Galactic Star Clusters in the $u'g'r'i'z'$ Photometric System

by

James Lewis Clem
B.Sc., University of Arkansas, 1998
M.Sc., University of Victoria, 2001

A Dissertation Submitted in Partial Fulfilment of the
Requirements for the Degree of

DOCTORATE OF PHILOSOPHY

in the Department of Physics and Astronomy

Supervisors: Dr. D A. VandenBerg & Dr. P. B. Stetson

Abstract

Although the Sloan Digital Sky Survey (SDSS) has compiled an unprecedented amount of photometric data on stellar populations in the Milky Way, it is not presently possible to *accurately* and *consistently* interpret these data due to the lack of precise fiducial stellar sequences and color–temperature relations for the new $u'g'r'i'z'$ photometric system. In order to address these deficiencies, this study describes an extensive observational project that has obtained high-quality and homogeneous photometry for a number of different Galactic star clusters spanning a wide range in metallicity ($-2.5 \lesssim$ [Fe/H] $\lesssim +0.3$), as observed in the $u'g'r'i'z'$ passbands with the MegaCam wide-field imager on the Canada-France-Hawaii Telescope. By employing these purest of stellar populations, fiducial sequences have been defined from color-magnitude diagrams (CMDs) that extend from the tip of the RGB down to approximately 4 magnitudes below the turnoff points: these have been accurately calibrated to the standard $u'g'r'i'z'$ system via a set of secondary photometric standards located within these same clusters. Consequently, they can serve as a valuable set of empirical fiducials for the interpretation of stellar populations data in the $u'g'r'i'z'$ system, as well as calibrators for the transformation of stellar isochrones to the $u'g'r'i'z'$ bandpasses. In fact, when a new grid of theoretical color–$T_{\rm eff}$ relations and bolometric corrections for the $u'g'r'i'z'$ system is computed from Kurucz model atmospheres and employed to translate isochrones to the observed planes, generally very good and consistent fits to the CMDs of the metal-poor ([Fe/H]<0.0) globular clusters M 92, M 13, and M 71 are found, once reasonable estimates of the cluster parameters are assumed (the only obvious discrepancy is a shift of $\sim 0.01 - 0.03$ mag between the predicted and observed giant branches when the models are fitted to the main sequences). Moreover, the same isochrone fits are entirely consistent with those inferred from cluster observations in other photometric systems – notably, the $BV(RI)_c$ and *uvby* systems.

At the metal-rich end ([Fe/H]$\gtrsim$0.0), however, these transformations fail to match the observed loci of cool, main-sequence stars ($T_{\rm eff} \lesssim 5000$K) in the open clusters M 67 and NGC 6791. An exploration into possible causes of these discrepancies is provided.

Table of Contents

List of Tables

List of Figures

Acknowledgements

On a personal level, I want to extend my deepest gratitude to my beautiful wife Melissa. She has shown much patience, sacrifice, understanding, and love to me throughout my education process here at UVic. I am so very blessed to have such a wonderful spouse and friend, and I look blissfully forward to spending many happy years together with her.

To those people who have made my research possible, I want to thank my supervisors, Don VandenBerg and Peter Stetson, for their insightful discussions, advice, motivation, and guidance during my study. Don - thanks so very much for your generous financial support over the 7 long years I have been under your supervision as a graduate student, as well as the many useful (and occasionally lighthearted) discussions we had over coffee. Peter - your knowledge of observational astronomy and photometric data reduction is very impressive, and this research could not have been possible without the fabulous suite of DAOPHOT algorithms that you have painstakingly written and maintained over the years. I anticipate many future collaborations and projects together. For everything, I thank you both immensely.

During the 7 years I have been in the department, I have seen many fellow grads come and go. I will never forget the fun discussions, the boat drink parties (thanks to Stephen G.), and laughs over beer on Friday afternoons. Thanks for the good times, everyone (and you know who you are).

I gratefully acknowledge use of the facilities at the HIA/DAO, as well as extend my appreciation for the generous allocation of time on the Plaskett telescope and the purchase of the $u'g'r'i'z'$ filter set for use in my research.

Finally, to my parents, thanks for your encouragement and support during this whole process. I love you both. Yes, Dad, I am finally finished with school.

Chapter 1

Introduction

1.1 The $u'g'r'i'z'$ Photometric System

In the Summer of 2005, the Sloan Digital Sky Survey (SDSS; York et al. 2000) officially ended its planned five years of sky scanning operations to obtain an unprecedented amount of imaging and spectroscopic data for approximately one-quarter of the sky. The SDSS operated on a dedicated 2.5 m telescope equipped with a large-format mosaic CCD to image the entire northern Galactic cap (i.e., $b > 30°$) in five photometric bands and two digital spectrographs to provide spectra for ~ 1 million stars, galaxies, and quasars scattered throughout the imaging area. Although designed to primarily investigate the large-scale structure of the universe, the imaging component of the SDSS has obtained high-quality multicolor photometry for about 10^8 stellar objects in the Milky Way, which represents the largest and most homogeneous database on Galactic stellar populations ever obtained. A notable feature of this database is that it was compiled in a new photometric system consisting of five unique basspands (u', g', r', i', and z') that were specifically designed for the SDSS to provide continuous coverage over the *entire* optical wavelength range.

This so-called $u'g'r'i'z'$ photometric system (Fukugita et al. 1996) is unique in

many respects when compared to other broadband filter sets, particularly the popular Johnson-Kron-Cousins $UBV(RI)_C$ system. As shown in Figure 1.1, the $u'g'r'i'z'$ filters cover a much broader range in wavelength, offer much less overlap of the spectral regions between filters, and have sharper cutoffs at the band edges. Furthermore, most of the bandpasses are significantly wider than those of the $UBV(RI)_C$ system which ensures a higher efficiency for the detection of faint objects. Arguably the most important feature of the $u'g'r'i'z'$ system, however, is the fact that its normalization is based on the spectrophotometric AB (absolute bolometric) magnitude system of Oke & Gunn (1983), which allows a magnitude to be directly related to physical units via the following definition:

$$AB_\nu = -2.5 \log \mathrm{f}_\nu - 48.60, \tag{1.1}$$

where f_ν is the flux of an object per unit frequency (ergs cm^{-2} s^{-1} Hz^{-1}). This convention is unlike the usual normalization definitions for other filter sets where the zero point is set by specifying some reference star (typically Vega) to have null colors. As a result, the $u'g'r'i'z'$ magnitudes measured by the SDSS can be conveniently converted to physical fluxes.

To ensure that any newly designed filter set can be widely used by the astronomical community, an extensive network of standard stars must first be established so that the observed photometry obtained on any telescope can be consistently calibrated back to the fundamental system. Such a network for the $u'g'r'i'z'$ system has been developed by Smith et al. (2002) using a 1 m telescope at the U.S. Naval Observatory (USNO) and consists of approximately 150 stars, most of which are situated near the celestial equator. Indeed, the calibration of the photometry resulting from the SDSS itself is based on this standard star system. Since the SDSS 2.5 m telescope is dedicated solely to scanning the sky throughout the entire night, along with the

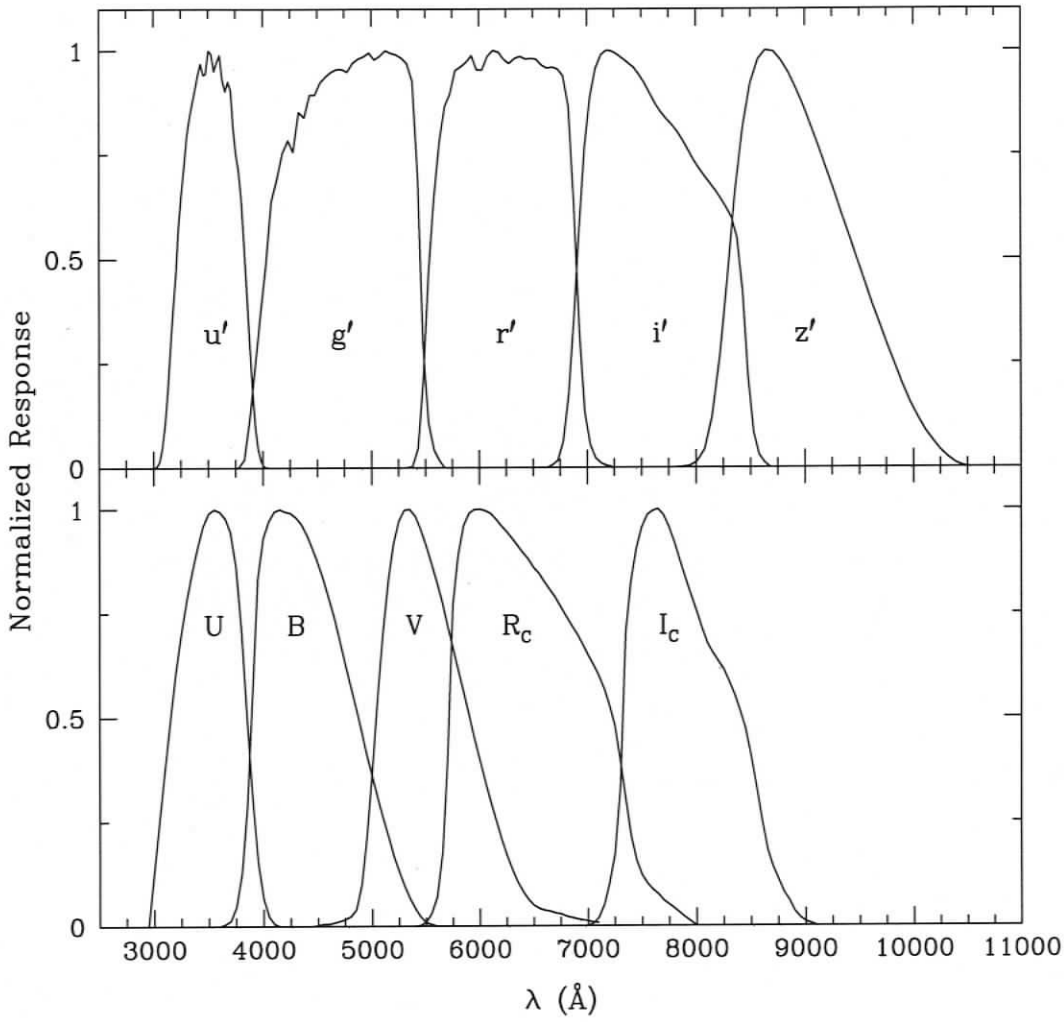

Figure 1.1: A comparison of the normalized filter response functions for the $u'g'r'i'z'$ and $UBV(RI)_C$ photometric systems. Note the broader coverage in wavelength space and sharper cutoffs for the $u'g'r'i'z'$ filters.

fact that all of the primary $u'g'r'i'z'$ standard stars are too bright to be imaged during the telescope's 54 second drift-scan exposure times, a rather unique setup allows the photometry collected from the survey telescope to be transformed to the standard system. A separate 0.5 m "photometric telescope" (PT) located next to the survey telescope is responsible for observing several different fields (denoted as secondary or transfer fields) that lie within the footprint of the SDSS sky coverage area along with observations of the $u'g'r'i'z'$ standards. Once calibrated to the standard system, the stars within these transfer fields will serve as fainter secondary standards for the calibration of the photometry from the survey telescope. Moreover, the PT also monitors the atmospheric extinction during nights when the survey telescope is imaging the sky.

Although this setup is ingenious in its design and efficiency, it is not without some problems. The most notable of these is the fact that the filters used on the PT and USNO telescope differ slightly from those on the 2.5 m survey telescope despite attempts to manufacture all three sets to be identical. This arises because the filters on the SDSS survey telescope are enclosed in the same vacuum environment as the CCD array, whereas the filters on the PT and USNO telescope are outside of the camera assembly and subject to the ambient air. As a result, the effective wavelengths of the g', r', and i' filters on the survey telescope are $\sim 1.5\%$ *shorter* than those of the PT and USNO filters. Thus, the photometric system as defined by the USNO telescope (and PT) is not directly applicable to the data from the survey telescope. Since one of the SDSS goals is to present AB magnitudes on the "natural system" of the survey telescope, a different nomenclature is adopted such that the calibrated magnitudes reported by the survey telescope are denoted as $ugriz$, while those on the USNO standard system are given the original $u'g'r'i'z'$ designation. It is anticipated, however, that these two essentially different (albeit slightly) photometric systems can be related to each other by simple linear relationships while still keeping their zero-points accurate on the AB system to within a few percent (Abazajian et al. 2003).

1.2 Thesis Goals

While the SDSS was the first to implement the $u'g'r'i'z'$ photometric system, analogous versions of these same filters are also currently in use with CCD imagers installed on the Gemini Telescopes, the Canada-France-Hawaii Telescope, and the Hubble Space Telescope so as to profit from the obvious synergy with the SDSS. Indeed, the very fact that the SDSS has already provided such a large database of photometry of stars and galaxies implies that the $u'g'r'i'z'$ system will likely be the filter set of choice for most future survey projects and a large fraction of future photometric observations. Despite this, much of our current observational and theoretical knowledge of resolved stellar populations is based largely on the conventional Johnson-Kron-Cousins $UBV(RI)_C$ photometric system, with a few other studies relying on niche systems like the Strömgren, DDO, Vilnius, and Geneva systems. Consequently, the empirical and theoretical tools that would tie the $u'g'r'i'z'$ system to the fundamental properties of observed stellar populations have yet to be defined. Specifically, neither well-calibrated fiducial stellar population sequences nor reliable color–$T_{\rm eff}$ relations are currently available for the $u'g'r'i'z'$ system, and yet, without them, it is impossible to fully exploit the capabilities of the SDSS data set as well as complementary studies employing these same filters.

In order to remedy these deficiencies, there is good reason to rely on $u'g'r'i'z'$ observations of star clusters within our own Galaxy. Clusters are the ideal stellar population templates because their constituents are effectively coeval, equi-distant, and nearly identical in terms of their heavy elemental abundances. As a result, their color-magnitude diagrams (CMDs) generally exhibit extremely tight and well-populated sequences of stars that span several orders of magnitude in brightness. Their wide distribution in metallicity is also suitable for characterizing how the photometric properties of stellar populations vary as a function of [Fe/H]. Consequently, cluster observations offer the perfect data sets to define fiducial stellar population

sequences that cover a broad range of stellar parameter space. These sequences serve as a set of empirical "isochrones" that not only facilitate the analysis of other stellar populations data, but also provide calibrators for stellar evolutionary models that are transformed to the observed CMDs via theoretically-derived color-$T_{\rm eff}$ relations (e.g., see Brown et al. 2005). Given the fact that the $u'g'r'i'z'$ system was introduced only a short time ago, however, the photometric database for star clusters remains too small to accomplish the tasks mentioned above. Unfortunately, the SDSS alone cannot provide a sufficient database since the imaging data do not extend deep enough to provide high-precision photometry for some of the fainter stars in the more distant metal-poor globular clusters, nor does the survey footprint reach down to the Galactic plane where the majority of metal-rich open clusters reside.

For these reasons, the present study has been designed to collect extensive observations at the Dominion Astrophysical Observatory (DAO) and at the Canada-France-Hawaii Telescope (CFHT) in order to thoroughly explore the nature of stellar populations in the $u'g'r'i'z'$ photometric system via observations of Galactic star clusters. The goal of this investigation is essentially threefold. First, to aid in the empirical analysis of stellar populations data, a set of fiducial sequences that span a broad range in both magnitude and metallicity is defined from high-quality and homogeneous photometric observations of the clusters listed in Table 1.1 as obtained on CFHT. Second, a network of fainter standard stars for the $u'g'r'i'z'$ system is established via repeat observations at the DAO to ensure that these fiducials are calibrated to the standard system with a high degree of accuracy. Finally, these fiducials are subsequently employed to test a new grid of theoretical color–$T_{\rm eff}$ relations and bolometric corrections for the $u'g'r'i'z'$ system that have been calculated from Kurucz synthetic spectra.

The chapters that follow describe both the derivation of the cluster fiducial sequences and the testing of the theoretical color–$T_{\rm eff}$ relations for the $u'g'r'i'z'$ system. In Chapter 2, the establishment of secondary photometric standard stars in the clus-

Table 1.1: Galactic star clusters observed in the CFHT survey.

Name	Type	α	δ	[Fe/H]	$E(B-V)^c$
M 67	open	08:51:18	+11:50:00	-0.15^b	0.040
M 3	globular	13:42:11	+28:22:32	-1.66^a	0.013
M 5	globular	15:18:34	+02:04:58	-1.40^a	0.038
M 13	globular	16:41:41	+36:27:37	-1.65^a	0.016
M 92	globular	17:17:07	+43:08:12	-2.24^a	0.023
NGC 6791	open	19:20:53	+37:46:30	$+0.11^b$	0.155
M 71	globular	19:53:46	+18:46:42	-0.58^a	0.265

[a] from Zinn & West (1984)

[b] from Friel et al. (2002)

[c] from Schlegel et al. (1998)

ters listed in Table 1.1 is described along with a detailed analysis of the quality of the resultant photometry when compared to the standard system. Chapter 3 then proceeds to employ these local cluster standards to calibrate an extensive set of cluster photometry obtained on the CFHT for the purposes of defining the highly accurate fiducial sequences. A new grid of theoretical color–$T_{\rm eff}$ relations and bolometric corrections for the $u'g'r'i'z'$ system that have derived from Kurucz synthetic spectra is described in Chapter 4, which also assesses their overall accuracy by comparing isochrones to the cluster fiducial sequences. Finally, a short summary and discussion of future work is provided in Chapter 5.

Chapter 2

The $u'g'r'i'z'$ Secondary Standards

The $u'g'r'i'z'$ standard star network established by Smith et al. (2002; hereafter S02) represents the primary system upon which the calibration of all the photometric data collected by the SDSS is based. Despite forming a firm and accurate observational foundation for the $u'g'r'i'z'$ photometric system, the S02 sample of standards imposes certain limitations for investigators observing on large telescopes due to the fact that they are scattered around the northern hemisphere and fairly bright ($9.0 \lesssim r' \lesssim 12.5$). Indeed, the 2.5 m SDSS survey telescope itself cannot rely on these stars as photometric calibrators since they would easily saturate the detector during the $\sim$ 60 second drift-scan exposure times, and it would greatly reduce the survey efficiency to interrupt sky-scanning operations to observe a different standard star every few minutes. While a rather ingenious setup has been devised to solve this problem by using fainter secondary standards scattered throughout the SDSS survey area (see Abazajian et al. 2003 for more specific details regarding this arrangement), the fact that primary standard sequences for some of the more popular filter sets, including the $u'g'r'i'z'$ system, are generally based on a sample of relatively bright, isolated stars represents the main problem facing investigators who wish to conduct accurate photometric calibration work on the variety of 4, 8, and 10 m class telescopes

that are online today.

To address the obvious need for fainter photometric sequences that are more suitable for use on large telescopes, Stetson (2000) has presented an extensive network of secondary standard stars for the Johnson-Kron-Cousins $BV(RI)_C$ system that are situated in a variety of "astrophysically interesting" targets, including a number Galactic star clusters. Clusters are ideal objects in which to establish these sequences since they contain a copious number of stars covering a wide range in both magnitude and color packed into a very small region of the sky. This fact allows a large number of useful standards to be imaged directly on a single CCD exposure using only moderate exposure times, thereby reducing the need for excessive slewing of the telescope. In theory, the same principles that Stetson (2000) employed can also be applied to the $u'g'r'i'z'$ system provided that observations of cluster program fields are obtained in conjunction with a sufficient number of the primary standard stars on successive photometric occasions in order to tie the cluster photometry as accurately as possible to the primary photometric system.

Given the aforementioned benefits of establishing secondary photometric sequences in star clusters, this chapter discusses efforts to derive a network of secondary standard stars for the $u'g'r'i'z'$ system which are situated in the star clusters listed in Table 1.1. The ultimate goal of this project is to relate the observed photometry for these cluster standards back to the primary system with an accuracy of 1% or better in each filter so they may be as reliable as the primary ones for photometric calibration purposes. While these secondary cluster standards will be used in the present study to calibrate the photometry for these clusters resulting from the CFHT (see Chapter 3), it is anticipated that they will also be useful for other researchers conducting $u'g'r'i'z'$ observations on large, high-demand telescopes due to their concentrations in small regions of sky and relative faintness. The following sections present the details of the secondary standard star development program. The instrumentation and a brief discussion of the observational strategy is presented in Section 2.1. A detailed

overview of the data reduction, including the important step of calibrating the observed cluster photometry to the standard $u'g'r'i'z'$ system, is provided in Section 2.2. Finally, a presentation and discussion of the final set of secondary cluster standards is given in Section 2.3, with a short summary in Section 2.4.

2.1 Observations

All observations were obtained at the Dominion Astrophysical Observatory (DAO) using the 1.8 m Plaskett telescope equipped with a thinned, back-illuminated SITe 1024×1024 CCD operating at a gain of $\sim 5.0\,e^-$/ADU with read noise of $\sim 11\,e^-$. The 24μm pixels of the detector each project to $\sim 0.546''$ on the sky at the modified f/5 Newtonian focus of the telescope to result in a full field of view of approximately 9.3′. This pixel scale is more than adequate to provide good sampling of point-source images when considering that atmospheric seeing conditions typically hover around $3-4''$ (FWHM) at the DAO.

Performance testing of the instrument setup was conducted on a variety of occasions during the observational program in order to investigate the linearity of the chip and the shutter timing performance. Based on these tests it was determined that (a) the chip maintained a linear response up to ∼32000 ADU – beyond this value the response was non-linear in a form that could not be determined or predicted reliably, and (b) shutter timing effects amounted to ~ 0.05 sec difference in measured exposure times across the chip from center to edge. In response to these findings, stars with peak values above 32000 counts in the science images were disregarded during the photometric reductions and exposure times of ≥ 5 sec were used to keep systematic deviations in the photometry derived from different portions of the detector to $\lesssim 1\%$. The combination of these two constraints also presented a problem when observing the brightest primary standard stars and necessitated the placement of a simple cardboard mask directly in front of the secondary mirror that served to effectively reduce

the aperture of the telescope down by a factor of four. This mask was in place on nights when data were collected in the g', r', and i' filters but removed for u' and z' observations due to reduced sensitivity of the CCD in these wavelength regimes.

The $u'g'r'i'z'$ filter set used for this project was manufactured by the Asahi Spectra Co. Ltd. in Japan and arrived at the DAO in 2003 July. Fortunately, the same manufacturers provided both the CCD detector (SITe) and the filter set (Asahi Spectra) used by S02 to establish on the primary $u'g'r'i'z'$ standards on the USNO 1.0 m telescope. Indeed, a graphical comparison of the spectral coverages of the two filter sets in Figure 2.1 reveals only subtle differences between them. Note that each transmission curve shown in the figure is computed by convolving the raw filter profile (as measured by the manufacturer) with the response curve for the SITe CCD, the reflectivity of two aluminium surfaces, and the altitude-scaled transmission of the terrestrial atmosphere.

This project was allocated a total of 135 nights of telescope time spanning a 15 month period beginning in 2003 July and ending in 2004 September. Observing runs were generally scheduled during dark or grey time of the lunar cycle, but a handful of runs coincided with bright time. During these bright periods, care was taken to avoid performing observations when the target fields were within 30 degrees of the moon in order to prevent background contamination in the science frames. Table 2.1 provides the details concerning the specific dates of each observing run along with the number of nights when observations were actually performed.

Since the goal of this project is to establish a network of secondary $u'g'r'i'z'$ standard stars from cluster stars whose calibrated magnitudes are reliable to the 1% level, it is important to mention the strategy employed while conducting the observations at the telescope that ultimately helped to ensure this goal was achieved. First, given the generous amount of telescope time allocated for this project, observations were generally limited to only one filter per night. This ultimately helped to improve the accuracy of the photometric transformations by allowing a large number of primary

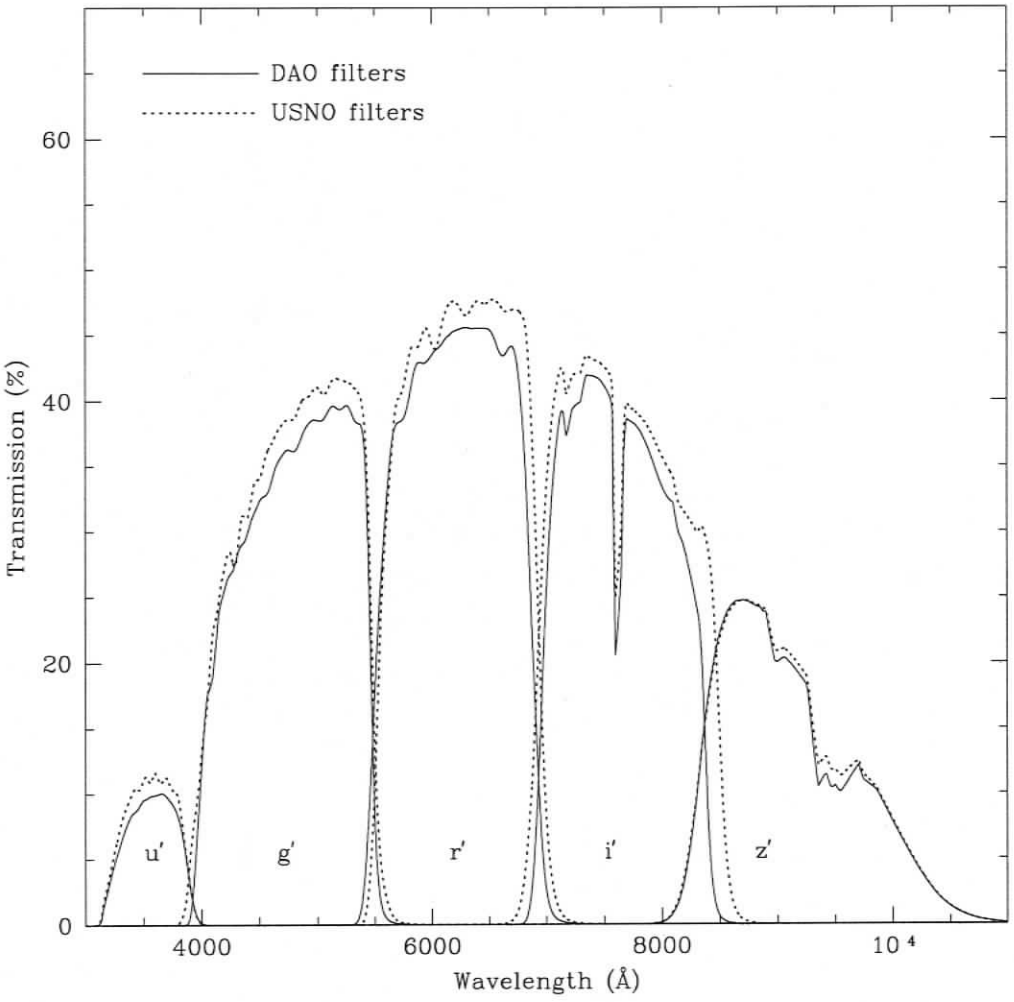

Figure 2.1: The spectral coverages of the DAO and USNO $u'g'r'i'z'$ filter sets. Each filter transmission curve is computed by convolving the raw filter profile with the response curve of the CCD detector, the reflectivity of two aluminium surfaces, and the altitude-scaled transmission of the terrestrial atmosphere.

Table 2.1: Log of Observing Runs at the DAO 1.8-m Telescope

Dates	# of Nights	# Usable	# of Observations
2003 Jul 22–27	6	6	373
Aug 15–21	7	5	360
Aug 28–Sep 3	7	3	132
Sep 23–Oct 1	7	5	501
Oct 24–Oct 30	7	0	0
Nov 7–11	5	0	0
Nov 17–27	11	0	0
Dec 11–15	5	0	0
2004 Jan 1–4	4	0	0
Jan 23–Feb 3	11	0	0
Feb 13–18	6	0	0
Mar 12–14	3	2	148
Mar 29–31	3	0	0
Apr 16–21	6	2	166
May 7–9	3	1	0
May 16–20	5	2	236
May 27–31	5	2	120
Jun 22–Jul 1	10	1	93
Jul 6–8	3	0	0
Jul 22–26	5	4	423
Jul 30–Aug 5	6	0	0
Aug 24–26	3	0	0
Sep 7–9	3	0	0
Sep 13–16	4	0	0
Total	**135**	**33**	**2619**

standards that cover a broad range in both airmass and color to be observed on any given photometric night. Furthermore, since good flat-fielding of the science data is essential for obtaining high-quality photometry, limiting observations to a single filter meant that a large number of high-signal sky flats could be taken during the evening and morning twilight periods. Second, the densest central regions of all the globular clusters in the program list were avoided due to obvious effects of crowding on the final photometry. Instead, a total of six different fields were situated according to the pattern shown in Figure 2.2 around each of globular clusters listed in Table 1.1. This layout was adopted due simply to the fact that it maximized the number of potential secondary standards in a single image while still avoiding the most crowded stars. In addition, as shown in the figure, each field overlapped its neighbour by at least 0.5′; this was advantageous since it offered the chance to check the photometric consistency between adjacent fields in the same cluster. For the two open clusters in the program list, on the other hand, crowding was much less severe and all exposures were centered on their cores to include as many cluster members as possible. Finally, exposure times were tailored to provide good photon statistics for a large number of stars each cluster field while still maintaining $\leq$32000 counts pixel^{-1} to avoid the nonlinear effects in the detector mentioned above. In this regard, a suitable level of precision ($\sim$1%) in the intrumental magnitudes could be achieved for stars lying approximately 3-4 magnitudes below the tip of a cluster's RGB while still keeping the exposures times relatively short (typically 100-600 seconds depending on filter). While this meant that the network of secondary standards resulting from this project would be based primarily on the brightest stars in any given cluster (i.e., brighter than a cluster's turnoff point), there still remain plenty of stars in each cluster covering a broad range in both magnitude and color to satisfy any investigator using them for photometric calibration work. Moreover, keeping the exposure times short increased the number of program fields observed in a single night.

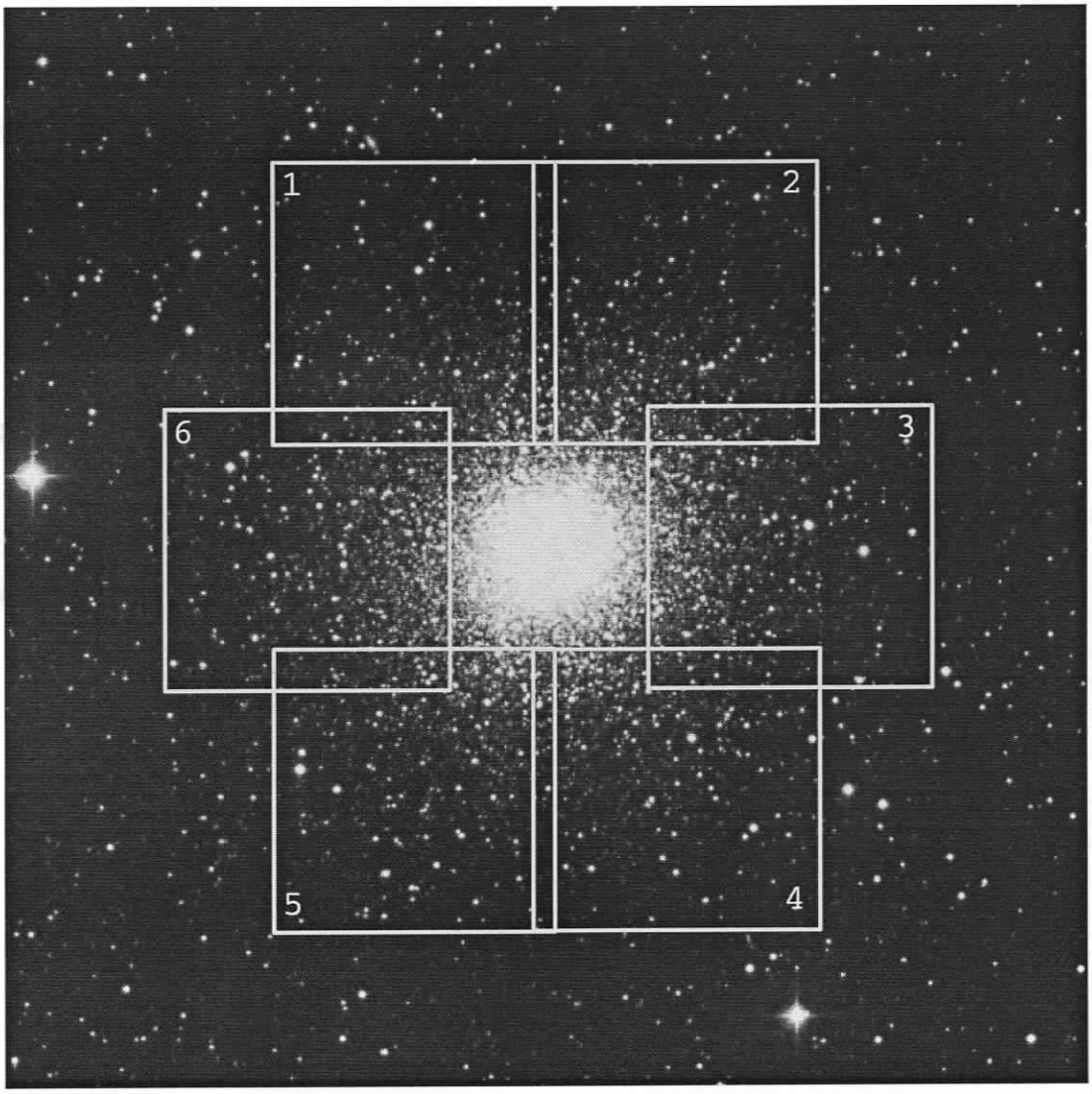

Figure 2.2: A DSS image for the globular cluster M 13 showing the locations of the 6 fields observed around each globular cluster in the program list.

2.2 Data Analysis

2.2.1 Pre-processing

All science images were pre-processed using routine techniques that employed an ample number of zero-second bias exposures and sky flats taken during the evening and morning twilight of each night. Generally, 10-15 individual flat-field exposures per filter were median-combined to produce a nightly master flat that was divided into each science frame to compensate for instrument-induced background structure (e.g., pixel sensitivity variations, illumination gradients, etc.). On a few occasions when sky conditions were not adequate for twilight flats, science frames were processed using either dome flats or a master flat for that filter from another night of the same observing run. However, if any science observations were collected on these same nights, they were all performed under non-photometric conditions. The effects of interference fringes were only noticeable in the science frames taken in the z' filter with a relative strength of $\sim \pm 3\%$ of the background level. Removal of these fringes was accomplished by median-combining all of the preprocessed z'-band science images to construct a master fringe frame which, in turn, was then normalized and subtracted from each individual science frame to result in a flat background. Table 2.1 provides the number of science observations recorded for each observing run resulting in a overall total of 2619 program images that were taken for this project.

2.2.2 The Instrumental Photometry

Relative instrumental magnitudes for all stars contained in the cluster program fields were obtained using standard point-spread function (PSF) modelling and fitting techniques with the DAOPHOT/ALLSTAR suite of algorithms (Stetson 1987; Stetson & Harris 1988). Due to the large number of cluster images collected for this project, a UNIX shell script was developed that executes DAOPHOT/ALLSTAR non-

interactively on each. In brief, this script serves to detect star-like objects, build a PSF model from a large number of bright, reasonably isolated stars, and subsequently subtract stars using this PSF model from each image. The script also iterates on each of these steps 2-3 times in an attempt to obtain a high quality PSF model and to detect any stars that were missed during the initial run through the image. The reliability of this automated reduction was assessed mainly via visual inspection of each individual star-subtracted image to check for obvious blemishes left behind by a badly constructed PSF model and/or an overabundance of missed stars. Generally, the script performed quite well and resulted in cleanly subtracted images for the vast majority of the cluster frames leaving only a handful of instances that required a manual execution of DAOPHOT/ALLSTAR.

For fields containing the primary $u'g'r'i'z'$ standards, on the other hand, standard aperture photometry was employed to derive the instrumental magnitudes since they were comparatively less crowded and occasionally contained too few stars of sufficient signal to construct a viable PSF model. A constant aperture radius of 30 pixels ($\sim$16″) was used to measure the magnitudes of all primary standards from every night. This was determined to be generous enough to contain the vast majority of light even during the worst seeing conditions while still preventing significant noise contributions from both the sky background and the CCD electronics. Regardless of the different techniques employed to obtain the photometry of the primary standards and cluster stars, the PSF-measured magnitudes for the latter are ultimately placed on a more absolute system using concentric-aperture growth curves derived with the DAOGROW software package (Stetson 1990). Since the magnitudes measured using PSF-fitting are referenced to an arbitrary zero-point that varies from frame to frame, it is generally necessary to apply a small aperture correction—a constant value for any given frame—to bring their magnitudes into better agreement with those determined from direct integration of a star's counts through a reasonably large aperture. As a result, the relative PSF photometry collected from different images

can be placed on a more homogeneous, aperture-based system that can be readily transferred to successive frames (provided the observations were performed during photometric conditions) and be more reliably calibrated to the standard system.

2.2.3 Astrometry

In order to compile a master star list for each star cluster, it is first necessary to match the natural CCD-based (x, y) coordinates for the stars detected in each cluster field to an external equatorial coordinate system. To perform this task the astrometric positions reported in the USNO-B1.0 guide star catalogue (Monet et al. 2003) are employed here to serve as the primary reference system, tabulated in terms of standard coordinates (ξ, η), to which all stars from each individual CCD image are subsequently cross-identified by positional coincidence. In general, all astrometric standards in a 1×1 degree region centered on the (α, δ) coordinates listed for each cluster in Table 1.1 are extracted from the USNO-B1.0 catalogue[1], and a preliminary set of positional transformations that solve for offset, scale, and rotation differences between the CCD-based coordinate system and the standard one is then established by relying on only a handful of the brightest stars from each list. Next, these initial transformation estimates are fed into the DAOMASTER task in an effort to improve their precision and accuracy by employing a set of third-order polynomials that further account for small higher-order effects due to optical distortions, filter-induced scale differences, and/or differential refraction in the CCD images[2]. These transformations, which are based on a larger sample of stars detected in each image, are iterated upon using robust fitting techniques with a matching tolerance gradually decreased from 5″ to 1″ (i.e., the matching radius used to decide if a star from each image refers to the same object). Once convergence is reached and the number of stars in the

[1]http://www.nofs.navy.mil/data/FchPix/

[2]Specifically, one polynomial predicting ξ as a function of x and y and another predicting η as a function of x and y for each CCD image

final list is stable, a master star list for each cluster is constructed using spherical geometry to relate the standard coordinate system (ξ, η) used for matching purposes to the equatorial coordinate system (α, δ).[3] In general, the average RMS of the residuals from the fitting between the USNO-B1.0 positions and the stellar positions in each CCD image ranged between $\sim 0.1''$ and $0.5''$ in both α and δ depending on the cluster. Since the scatter in the transformed stellar positions in pure CCD-image-to-CCD-image comparisons are typically much smaller than this, the scatter in the comparisons to the USNO-B1.0 catalogue is largely dominated by the precision of the latter, most likely due to the poorer sampling and signal-to-noise ratio in the original photographic data, the difficulty of determining the centroid of stellar blends and non-stellar astronomical objects, and accumulated proper-motion displacements over the period of time between the acquisition of the Sky Survey plates and the CCD data. Based on this information, one can reasonably expect that the astrometric positions reported for each cluster are internally precise to better than $0.1''$.

2.2.4 Photometric Calibrations

Transforming the observed instrumental photometry for the cluster stars to the primary $u'g'r'i'z'$ standard system represents the most crucial component of this project. When establishing a secondary standard star network such as this, it is important that the cluster photometry be firmly tied to the fundamental photometric system via observations of a number of primary standard stars. Moreover, it is imperative to perform repeat observations of the cluster program fields periodically over time in order to average out variations in the atmospheric extinction and/or the observational equipment. Assuming that the calibration equations employed to relate the instrumental photometry to the standard system can reliably compensate for

[3]It is important to note that these same techniques described here were also used to establish a master star list for each primary standard field in order to facilitate in the identification and matching of standard star observations from night-to-night and filter-to-filter during the photometric reductions.

both the combined effects of atmospheric extinction, bandpass mismatch, and any other systematic trends caused by the observing equipment or sky conditions, one can reasonably expect the uncertainties in repeat measurements of the same object to hover around the 2-3% level on any given photometric night. Indeed, this level of scatter is typical of most CCD-based photometry obtained during photometric conditions and is likely dominated by short-term fluctuations in the instantaneous extinction at the observing site, flat-fielding errors, and/or intrinsic differences in the spectral energy distributions among standard stars with similar observed color. If, however, an ample number of standards is used to derive the transformation constants, then the accuracy of the calibrated photometry is ultimately improved by a factor of order $\sqrt{N-m}$, where N is the number of standard-star measurements, and m is the number of free parameters in the adopted transformation equation. This section proceeds to show that when standard photometric calibration techniques are employed, together with observations of primary standard stars, the level of accuracy achieved meets the ultimate goal of 1% discussed above.

Photometric indices for the 158 primary $u'g'r'i'z'$ standard stars are taken from the work of S02. Moreover, an extended list of $\sim$ 1000 additional standard stars, kindly provided in advance of publication by J.A. Smith (private communication), were also included by virtue of the fact that they are situated in the same fields as the primary standards. This supplementary list of "extra" primary standards is a by-product of the initial definition of the standard star network at the USNO by S02, but, for a variety of reasons, were not included in their published list. Despite increasing the number of viable standard stars for this investigation, the majority of the stars ($\sim$ 70%) in both the primary and extended standard lists are still located near the celestial equator. Consequently, they do not get above $\sim$1.5 airmasses when situated on the meridian at the DAO. As a result, the strategy was to observe these equatorial standards two times per night – once when near the meridian, and again at a high airmass ($\sim$1.7-1.8). The remaining standard stars in the list are generally scattered

to higher declinations and observed approximately every 60-90 minutes throughout the night to supplement the airmass range.

Initially, the transformation of the observed instrumental magnitudes to the standard system is accomplished mathematically for each $u'g'r'i'z'$ filter through a set of equations taking the form

$$u'_{obs} = u'_{std} + Z_u + K_u(X-1) + b_u(u'-g')_{std} + c_u(X-1)(u'-g')_{std}, \quad (2.1)$$

$$g'_{obs} = g'_{std} + Z_g + K_g(X-1) + b_g(g'-r')_{std} + c_g(X-1)(g'-r')_{std}, \quad (2.2)$$

$$r'_{obs} = r'_{std} + Z_r + K_r(X-1) + b_r(r'-i')_{std} + c_r(X-1)(r'-i')_{std}, \quad (2.3)$$

$$i'_{obs} = i'_{std} + Z_i + K_i(X-1) + b_i(r'-i')_{std} + c_i(X-1)(r'-i')_{std}, \quad (2.4)$$

$$z'_{obs} = z'_{std} + Z_z + K_z(X-1) + b_z(r'-z')_{std} + c_z(X-1)(r'-z')_{std}, \quad (2.5)$$

where X denotes the airmass of the observation. It is important to note that these calibration equations are virtually identical to those employed by S02 in the definition of the $u'g'r'i'z'$ standard system (note the inclusion of a second-order color-extinction term to account for the fact that light from blue stars suffers more extinction than red stars as it passes through the terrestrial atmosphere). In addition, formalisms such as these are advantageous because they allow observations to be made in only a single filter for an entire night since the equations are functions of the *standard* rather than the *observed* color index. Moreover, each equation can be easily modified to accommodate data from non-photometric nights by removing the airmass term from the solution and deriving a unique photometric zero point to each CCD image on the basis of the standard stars it contains. Note, however, that observations collected on non-photometric nights only serve to improve the *precision* of the relative photometry for stars in a particular field but contribute nothing to the overall *accuracy* of the photometry on the standard system.

Once estimates for both the observed instrumental and standard magnitudes (and colors) for all the $u'g'r'i'z'$ standard stars observed on a particular night are fed into these equations, along with the airmass of each observation, the coefficients Z_i, K_i, b_i, and c_i are initially calculated using robust least-squares techniques as part of the CCDSTD algorithm (Stetson 2005). An important feature of the CCDSTD software is that it assigns a reduced weight to discrepant points while it iterates on the photometric solution, thereby minimizing the adverse effects of discordant measurements on the overall results. Moreover, it provides the user an opportunity to include additional low-order terms in the transformation equations to account for certain effects caused by the observing equipment and/or sky conditions at the observing site that may impart systematic deviations in the residuals. Such trends are commonly discovered once the residuals from the initial photometric reductions are examined as functions of the suspect variable. Indeed, it was noticed that when the computed residuals from any particular night were plotted against the x-coordinate location of the standard stars in the CCD images, they exhibited a slight, but noticeable, systematic trend. Not only was this trend present in the residuals from every night of observations, but it was also quite consistent within data sets performed in the same filter on separate nights. To demonstrate this, Figure 2.3 plots the residuals from the initial photometric solutions versus x-coordinate for standards observed in each filter over all photometric nights. The solid lines in each panel denote the weighted least squares fit to the data resulting in slopes for the individual filters of $x_{u'} = 0.027 \pm 0.010$, $x_{g'} = 0.048 \pm 0.006$, $x_{r'} = 0.066 \pm 0.007$, $x_{i'} = 0.077 \pm 0.006$, and $x_{z'} = 0.087 \pm 0.008$ mag per 1000 pixels. As a result of these findings, additional x-dependent terms are included in the transformation equations with their coefficients set to these derived values for a subsequent run through the photometric calibrations for all nights. The values for the derived transformation coefficients, number of observed standards, and the RMS dispersion in the residuals are given in Table 2.2 for each photometric night of the observational program.

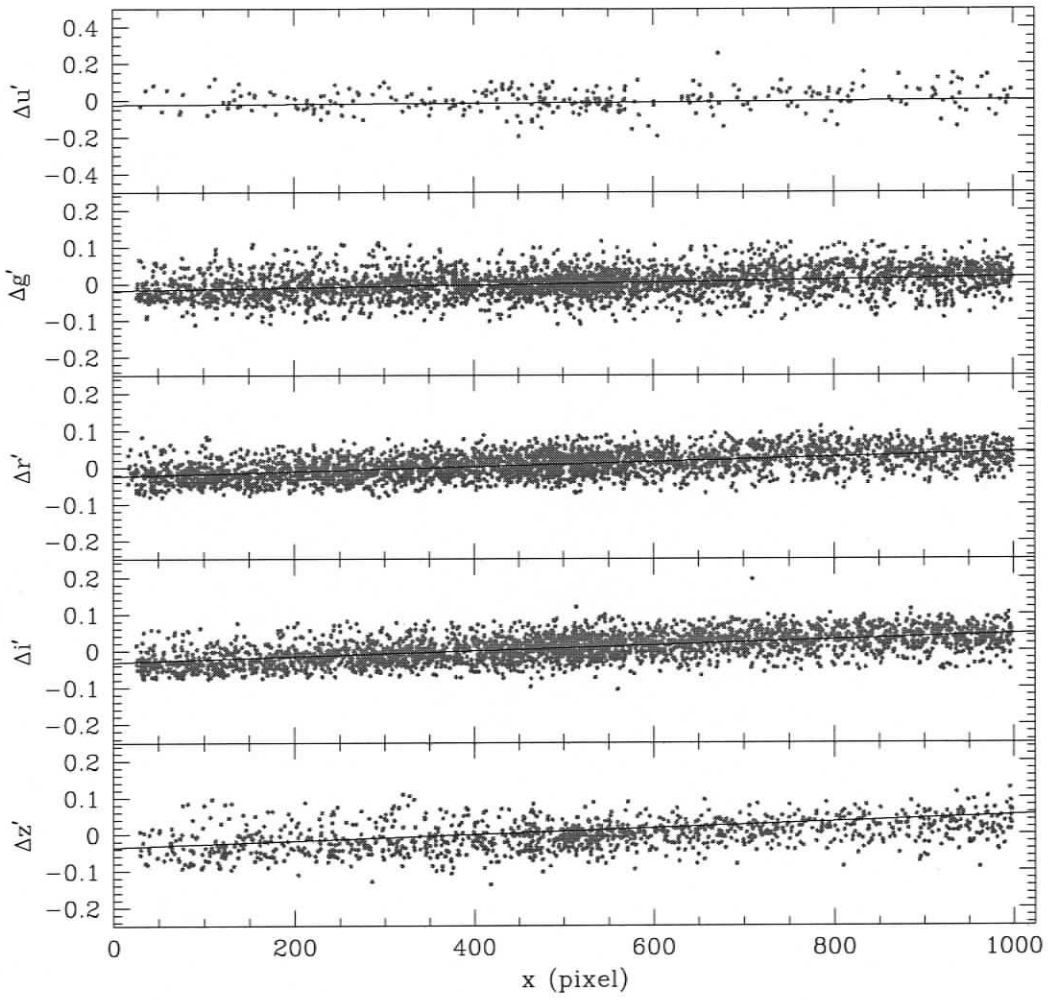

Figure 2.3: A plot of the $u'g'r'i'z'$ residuals from the photometric solutions versus x-coordinates of the standard stars in the CCD image. The solid lines denote weighted least squares fits to the data whose corresponding slopes are used to correct for these residual trends.

Table 2.2: Transformation Constants Derived for All Photometric Nights

UT Date	Filter	Z_i	b_i	c_i	K_i	N	RMS
2003-07-23	r'	3.8210 ± 0.0107	-0.0109 ± 0.0198	-0.0046 ± 0.0492	0.1766 ± 0.0199	524	0.0277
2003-07-24	u'	5.3988 ± 0.0148	-0.1475 ± 0.0106	$+0.0500 \pm 0.0254$	0.4910 ± 0.0398	123	0.0333
2003-07-25	r'	3.6663 ± 0.0091	$+0.0053 \pm 0.0208$	-0.0576 ± 0.0456	0.1673 ± 0.0177	287	0.0287
2003-07-27	i'	3.8641 ± 0.0078	-0.1094 ± 0.0338	$+0.0714 \pm 0.0656$	0.1341 ± 0.0143	548	0.0200
2003-07-28	g'	4.0212 ± 0.0063	-0.0710 ± 0.0084	-0.0196 ± 0.0149	0.2703 ± 0.0115	512	0.0142
2003-08-18	r'	3.7137 ± 0.0076	-0.0076 ± 0.0160	$+0.0028 \pm 0.0350$	0.1280 ± 0.0146	694	0.0231
2003-08-19	z'	4.8705 ± 0.0114	-0.0588 ± 0.0404	$+0.0556 \pm 0.0932$	0.0741 ± 0.0213	291	0.0200
2003-08-20	i'	3.9075 ± 0.0068	-0.0286 ± 0.0258	-0.0600 ± 0.0603	0.1280 ± 0.0129	616	0.0210
2003-08-21	g'	4.0582 ± 0.0037	-0.0671 ± 0.0058	-0.0351 ± 0.0117	0.2497 ± 0.0076	704	0.0143
2003-09-05	u'	5.4580 ± 0.0347	-0.1137 ± 0.0197	-0.0512 ± 0.0362	0.6549 ± 0.0663	145	0.0413
2003-09-06	z'	4.7837 ± 0.0094	-0.0223 ± 0.0147	$+0.0263 \pm 0.0270$	0.0715 ± 0.0162	677	0.0258
2003-09-24	r'	3.7934 ± 0.0054	-0.0038 ± 0.0123	-0.0045 ± 0.0229	0.1226 ± 0.0101	361	0.0174
2003-09-26	g'	4.1379 ± 0.0044	-0.0539 ± 0.0070	-0.0405 ± 0.0137	0.2255 ± 0.0088	949	0.0157
2003-09-29	z'	4.8167 ± 0.0076	-0.0198 ± 0.0113	$+0.0103 \pm 0.0273$	0.1306 ± 0.0153	307	0.0221
2003-09-30	i'	4.0293 ± 0.0078	-0.0279 ± 0.0095	$+0.0354 \pm 0.0223$	0.1872 ± 0.0171	518	0.0261
2004-04-22	g'	4.3972 ± 0.0196	-0.0866 ± 0.0206	-0.0031 ± 0.0349	0.3040 ± 0.0196	123	0.0250
	r'	4.0013 ± 0.0241	-0.0611 ± 0.0398	$+0.1513 \pm 0.0543$	0.1762 ± 0.0230	128	0.0314
	i'	4.0774 ± 0.0227	-0.0802 ± 0.0382	$+0.1445 \pm 0.0512$	0.1083 ± 0.0220	125	0.0296
2004-05-18	g'	4.5731 ± 0.0095	-0.0659 ± 0.0151	-0.0373 ± 0.0289	0.3692 ± 0.0176	237	0.0224
	i'	4.2994 ± 0.0054	-0.0223 ± 0.0281	-0.0010 ± 0.0549	0.1596 ± 0.0100	240	0.0164
2004-05-19	r'	4.2046 ± 0.0083	-0.0031 ± 0.0189	$+0.0417 \pm 0.0389$	0.2347 ± 0.0167	237	0.0280
	z'	5.1968 ± 0.0063	$+0.0181 \pm 0.0291$	$+0.0594 \pm 0.0613$	0.1327 ± 0.0126	231	0.0227
2004-06-09	i'	2.5246 ± 0.0044	$+0.0015 \pm 0.0190$	$+0.0732 \pm 0.0432$	0.1245 ± 0.0091	915	0.0203
2004-06-30	r'	2.3311 ± 0.0091	-0.0068 ± 0.0216	$+0.1159 \pm 0.0733$	0.1282 ± 0.0219	550	0.0313
2004-07-23	r'	2.2976 ± 0.0095	$+0.0021 \pm 0.0115$	-0.0149 ± 0.0287	0.1134 ± 0.0099	969	0.0207
2004-07-24	i'	2.5120 ± 0.0052	-0.0581 ± 0.0217	$+0.0302 \pm 0.0512$	0.0994 ± 0.0105	1119	0.0250
2004-07-27	g'	2.6350 ± 0.0135	-0.0758 ± 0.0203	-0.0036 ± 0.0425	0.2664 ± 0.0293	949	0.0563

In an effort to check the overall quality of the transformed magnitudes, the instrumental photometry for *all* of the observed primary standard stars observed on each photometric night are run backwards through the photometric equations to place them on a mean system so they may be readily compared to their $u'g'r'i'z'$ photometry. Such comparisons are shown in Figures 2.4 and 2.5 where the differences between the standard magnitudes and the present mean calibrated ones are plotted against both magnitude and color. Only those stars that have standard errors less than 0.03 mag and at least 3 observations on photometric occasions in each filter, along with no evidence of variability greater than 0.05 RMS (when all filters are considered together) in the present data set are plotted in each panel. All stars in the S02 data set already meet these criteria. Reassuringly, the horizontal lines corresponding to zero difference appear to pass through the densest concentration of points in Figure 2.4. Moreover, there seem to be no strong systematic trends as a function of $(g' - i')$ color in Figure 2.5 that would indicate the need for additional second-order color terms in the photometric solutions. Indeed, the photometry derived here exhibits superb consistency with that of S02: the mean differences are $\lesssim 0.001$ mag for the g', r', i', and z' filters and ≤ 0.002 mag for u'.

While graphical comparisons such as those presented above are useful in identifying systematic trends or deviations in the derived photometry, the ultimate accuracy to which the magnitudes have been placed on the standard system is better expressed quantitatively in terms of the nightly RMS dispersion in the residuals resulting from the calibrations. As discussed above, one can expect that absolute uncertainty in the zero points of the magnitude scale for any given photometric night to be no better than $\sigma_{RMS}/\sqrt{N-m}$ where N is the number of standards observed and m is the number of free parameters in the transformation equations. In other words, this represents the expected systematic uncertainty in the values of the calibrated magnitudes for *all* stars in *any* target field. Note that this differs from the random uncertainties associated with each star caused by profile errors, photon statistics, readout noise,

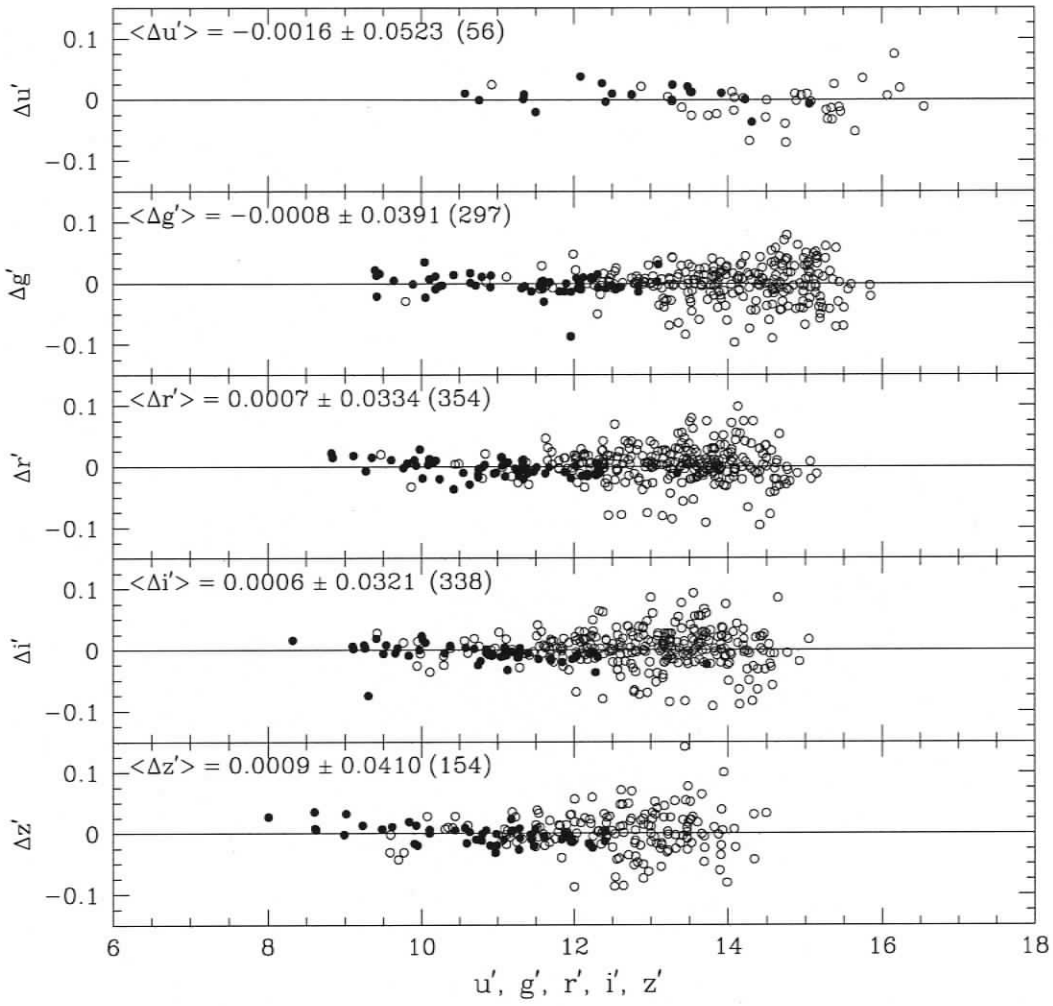

Figure 2.4: Comparison between the photometry for the $u'g'r'i'z'$ standards published by S02 and the mean calibrated magnitudes from the present analysis for the same stars. In each panel the Δmag represents the difference in the sense (present-S02) plotted against its respective magnitude on the standard system. Solid circles correspond to those standards included in the original S02 published list, while open circles are the "extra" standards provided by J. A. Smith (private communication). The mean difference, standard deviations, and number of stars used in computation of the means are indicated in each panel with the horizontal lines showing equality between the data sets.

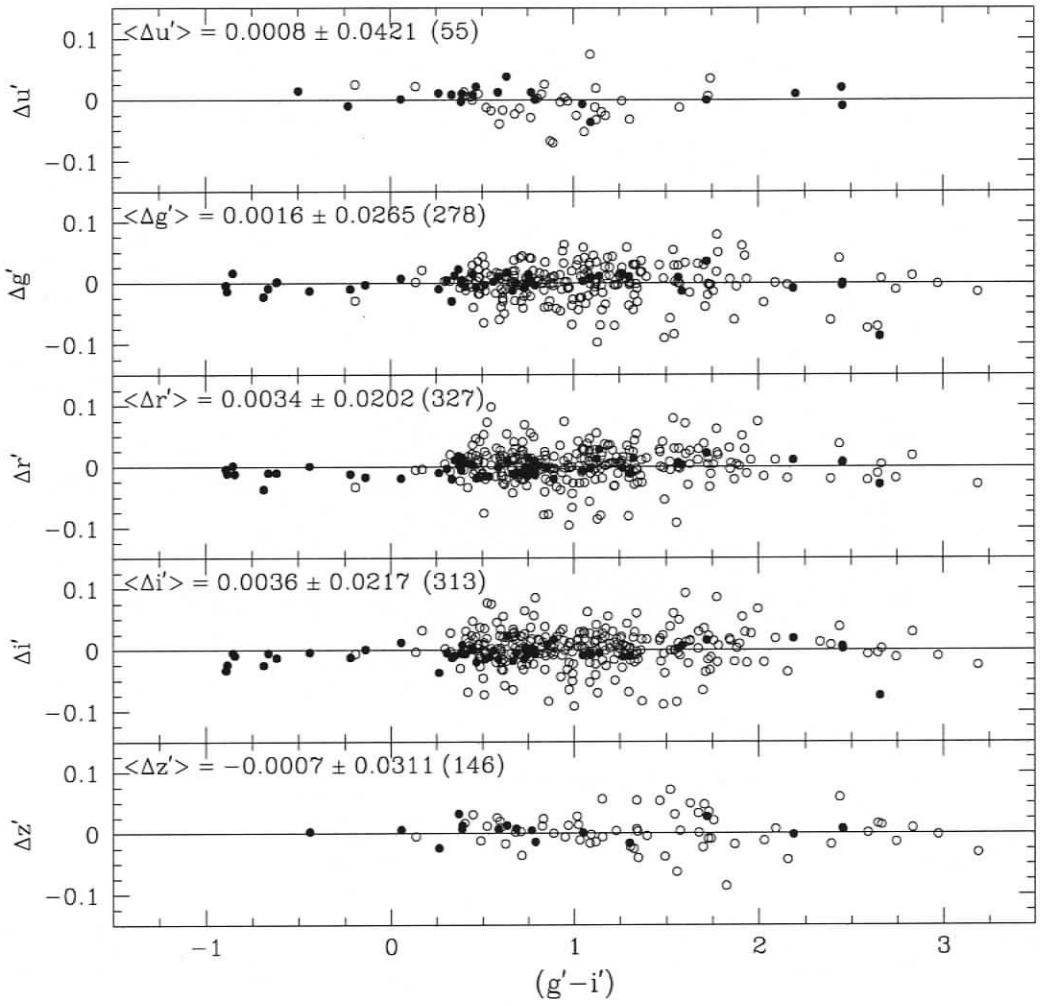

Figure 2.5: Same as Figure 2.4 except the magnitude residuals are now plotted as a function of *standard* $(g' - i')$ color.

variability, etc. since these are quoted on a star-by-star basis. For example, based on the information presented in Table 2.2, the RMS dispersion in the residuals for all filters ranges between 0.014 and 0.060 mag over all nights. This implies that the resulting systematic uncertainties in the photometric zero points can be no better than ~ 0.003 mag when considering the average number of primary standards observed on any given photometric night was ~ 450.

2.3 The Cluster Secondary Standards

Once the nightly coefficients have been determined using least-squares fitting, it is simply a matter of applying the transformation equations to the instrumental photometry for all cluster stars in all images in order to place their photometry nominally on the standard $u'g'r'i'z'$ system. Calibration of the entire set of cluster photometry began with the selection of a number of well-isolated stars with good precision in their instrumental magnitudes from the ALLSTAR photometry files so they may serve as a set of local standards for each cluster field. In actuality, this process relied solely on the collection of stars that were used to derive the model PSF for each cluster image since, by design, they should be relatively bright, non-saturated, and largely free of contamination by neighbors. The definition of these local standards allowed a redetermination of the zero-points of the magnitude scale from frame-to-frame via the comparison of their observed instrumental magnitudes with those placed on the mean system described above (i.e., the mean magnitude system based on all photometric nights). This helps to reduce the uncertainties due to extinction variations between successive frames and/or errors the aperture corrections, and it improves the overall precision of relative photometry averaged over many frames. Once new zero-points are derived in this fashion, the photometry for *all* cluster stars is finally referred to the standard system.

After the calibration of the cluster photometry to the standard system had been

performed, a final, definitive list of secondary standards for each cluster was constructed under the stipulation that a star should have been observed under photometric conditions at least 3 times *and* have a standard error of the mean magnitude less than 0.03 mag in at least two of the $u'g'r'i'z'$ filters. Also excluded from the list was any star that showed evidence of variability at the level 0.05 mag or greater when the standard deviations of the magnitude measurements from all filters were considered together. Any star excluded by these criteria cannot be considered suitable for use as a secondary photometric standard. Table 2.3 provides a listing of the total number of secondary standards that survived the aforementioned cuts in each cluster, along with the approximate field sizes that these standards cover on the sky around each target. Note that due to the fact that observations were generally conducted using one filter per night, there is not an equal number of standards observed in all five filters. This is especially true for the u' standards since the comparatively lengthy exposure times ($\sim$ 600 sec) needed to achieve a decent signal for even the brightest stars in this filter meant that observations were performed only in the northern-most fields of each globular cluster (i.e., Fields 1 and 2 in Figure 2.2). In addition, due to the persistent bad weather during early 2004 when M 5 was accessible to the telescope, only two observations in each of the g', r', and i' were obtained for this cluster during non-photometric conditions. As a result, no stars in M 5 could be defined as suitable secondary standards according to the criteria mentioned above and it was therefore excluded from future consideration for the remainder of this discussion.

To demonstrate the range in color-magnitude space covered by the secondary standards, Figures 2.6 and 2.7 plot the $(g' - r', r')$ diagrams for the four remaining globular clusters and the two open clusters in the sample, respectively. In each figure, black dots represent those stars that survived the criteria mentioned above to be considered a secondary standard, while the smaller, grey dots show the ones that did not. In Figure 2.6 the cluster red-giant and horizontal branch sequences are easily recognizable, except in the case of M 71. The combined effects of a low Galactic

Table 2.3: Number of secondary standard stars per filter in each cluster.

Name	Field Size	$N_{u'}$	$N_{g'}$	$N_{r'}$	$N_{i'}$	$N_{z'}$
M 67	$9.5' \times 9.5'$	0	276	276	276	0
M 3	$27.0' \times 27.0'$	0	662	670	670	650
M 5	$19.0' \times 27.0'$	0	0	0	0	0
M 13	$27.0' \times 27.0'$	768	2529	3382	3382	3382
M 92	$27.0' \times 27.0'$	334	1141	1489	1489	1489
NGC 6791	$12.3' \times 10.9'$	0	2073	2090	2090	2090
M 71	$27.0' \times 27.0'$	1472	7379	9579	9579	9579

latitude for M 71 and the field arrangement shown in Figure 2.2 result in a CMD that is dominated by field stars and largely devoid of cluster members. Regardless of this, the secondary standards in the M 71 field are defined primarily from field stars that exhibit the same approximate range in color as those for the remaining three globular clusters. Examination of the CMDs for the open clusters M 67 and NGC 6791 in Figure 2.7 also reveals that secondary standards form well-defined sequences that exhibit a color range that is only slightly less than that of the globulars, but still cover a comparable range in magnitude.

2.4 Summary

Based on the information and analysis presented above, it is concluded that the observed photometry for the secondary cluster standards has been placed on the standard $u'g'r'i'z'$ system with an accuracy of 0.01 mag or better in each of the five filters. Moreover, a large number of standards is present in each cluster that cover a broad range in color and extend down as faint as $r' \sim 20$ to facilitate the calibration of photometric data obtained on large telescopes. For example, the vast majority of these cluster stars ($\sim 90\%$) are appropriate for use on telescopes with apertures as large as 8 meters (i.e., $r' \gtrsim 15$) using exposure times of a few seconds, and their large

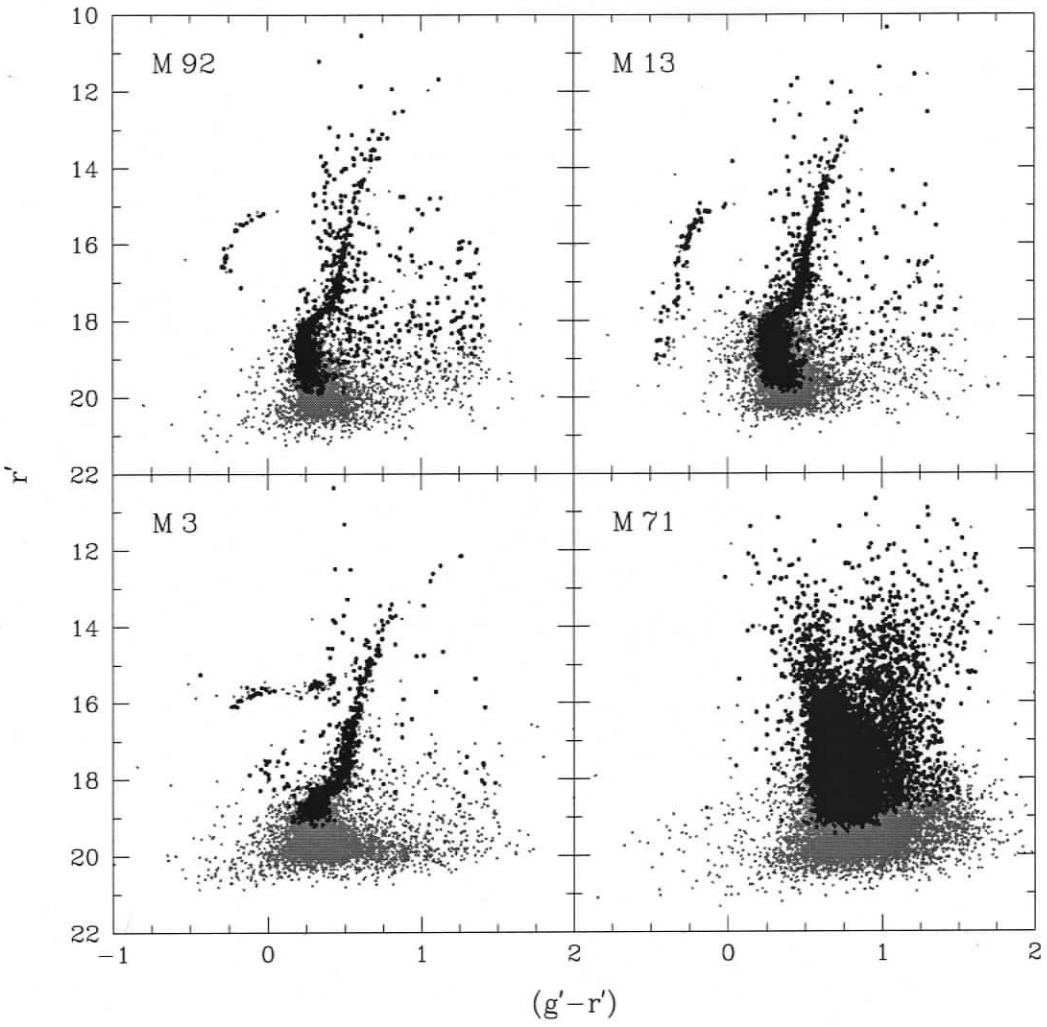

Figure 2.6: $(g' - r', r')$ CMDs for the 4 globular clusters in the present sample. The solid black dots represent the secondary standards established in the fields surrounding each cluster.

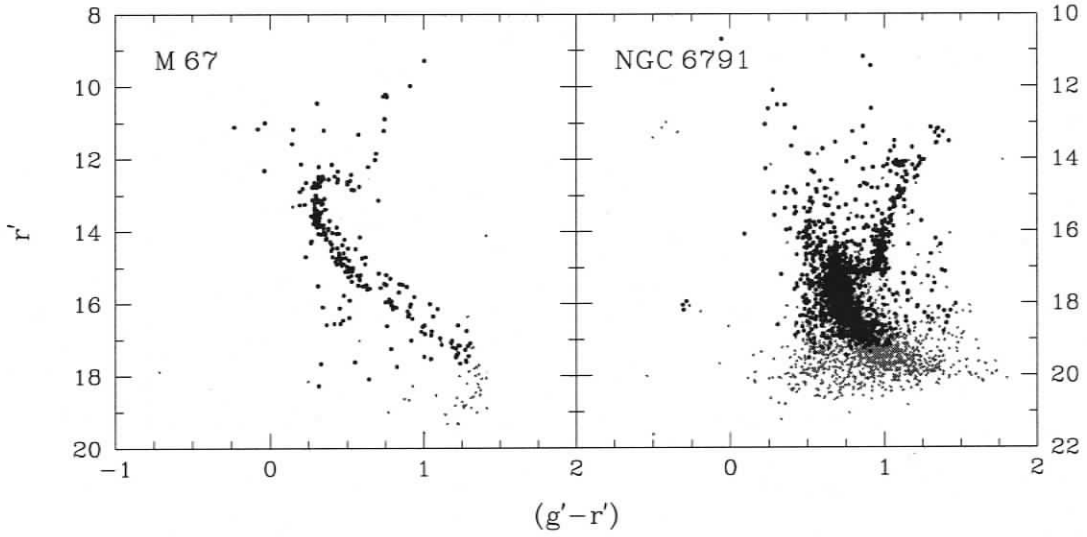

Figure 2.7: Same as Figure 2.7 except for the open clusters M 67 and NGC 6791.

concentrations on the sky reduce the need to take valuable time on these high-demand telescopes away from program observations in order to conduct calibration work. Indeed, these facts were the driving force behind the establishment of the secondary photometric sequences so that photometry of the same clusters obtained on the CFHT could be suitably calibrated to the $u'g'r'i'z'$ standard system as described in the next chapter. However, it is anticipated that these cluster standards will also prove to be quite valuable for any northern-hemisphere researcher who wishes to obtain highly accurate photometry from a moderately-sized telescope.

Chapter 3

Stellar Cluster Fiducial Sequences for the $u'g'r'i'z'$ System

Given that the SDSS will produce a large amount of high-quality multi-band photometry for Galactic stellar populations, it is essential that the $u'g'r'i'z'$ photometric system be tied to the physical properties of stars via the definition of fiducial stellar sequences. The most straightforward way to accomplish this is by observing a number of different open and globular clusters in the $u'g'r'i'z'$ filters so that fiducial sequences extending over a broad range in both magnitude and [Fe/H] can be derived from the loci of cluster stars in color-magnitude or color-color space. Star clusters are ideal for this purpose since (1) their constituents can be approximated to have the same distance, age, and metallicity, (2) they typically contain enough stars so that even short-lived evolutionary stages are well represented in a CMD, and (3) they span a wide range in metallicity from [Fe/H] ≈ -2.5 for the most metal-poor globular clusters to well above the solar value for some open clusters. Provided the cluster photometry is well calibrated to the standard system, the resulting fiducial sequences would not only serve as an invaluable set of empirical isochrones to aid in the interpretation and analysis of stellar populations data in the $u'g'r'i'z'$ system ob-

tained on any telescope, but also provide useful calibrators for the transformation of theoretical stellar models to the $u'g'r'i'z'$ bandpasses. While a detailed investigation of the latter is left until the next chapter, the current discussion presents the details behind the derivation of these fiducial sequences from a collection of high-quality, homogeneous star cluster photometry obtained on the 3.6 m Canada-France-Hawaii Telescope (CFHT) that has been calibrated to the $u'g'r'i'z'$ system using the network of secondary standard stars established in the previous chapter.

3.1 The CFHT Star Cluster Survey

To address the need for fiducial sequences in the $u'g'r'i'z'$ system, an observational program aimed at obtaining high-quality photometry for a number of Galactic star clusters was recently conducted on the 3.6 m CFHT in early 2004. One of the most notable features of these cluster observations is the fact that they were obtained using CFHT's wide-field mosaic imager known as "MegaCam". As shown in Figure 3.1, MegaCam contains 36 individual CCDs that combine to offer nearly a full 1x1 degree field of view with high angular resolution ($\sim 0.187''$/pixel at the f/4 prime focus). Moreover, MegaCam operates with a set of $g'r'i'z'$ filters whose effective wavelengths and bandwidths are very similar to those of the USNO/SDSS. For observations in the UV, however, a slightly different filter than u' is employed; this so-called u^* filter was designed to take advantage of the superb sensitivity of the MegaCam CCDs at short wavelengths along with the reduced atmospheric extinction in the UV at high altitudes. Figure 3.2 compares the spectral coverage of the MegaCam filter set to the USNO $u'g'r'i'z'$ bandpasses.

The star clusters listed Table 1.1 were selected for this survey since they are relatively nearby, well-populated, and cover a wide range in [Fe/H]. The observing strategy was designed not only to achieve a high level of photometric precision for cluster stars ranging over several magnitudes for the definition of the fiducial sequences,

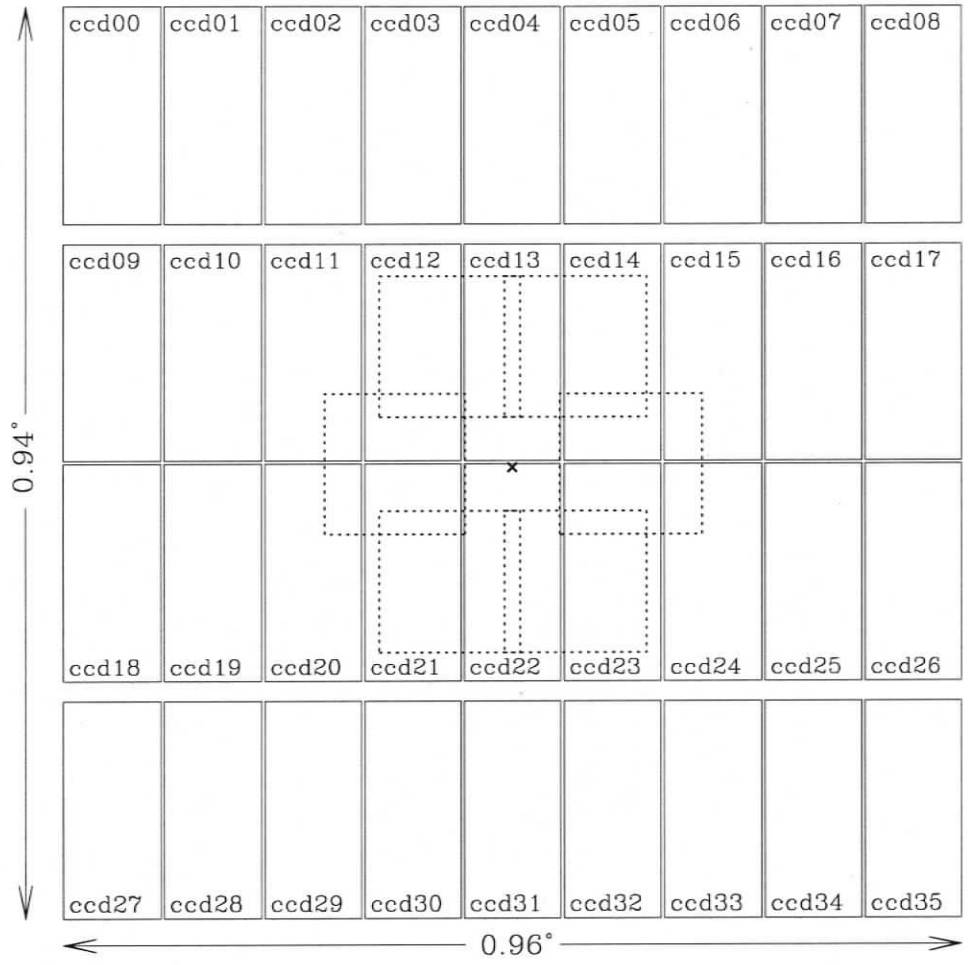

Figure 3.1: A schematic showing the layout of the 36 individual CCD chips in the MegaCam mosaic camera. Each chip measures 2048×4612 pixels and projects to ∼6.4×14.4′ at the CFHT f/4 prime focus resulting in a full field of ∼0.96×0.94 degrees for the entire mosaic. The cross near the center of the mosaic (located ∼ 14″ below the top of ccd22) corresponds to the location of the optical axis of the telescope in the focal plane. The boxes denoted by dotted lines indicate the approximate locations of the 6 DAO fields containing the secondary $u'g'r'i'z'$ standards derived in Chapter 2.

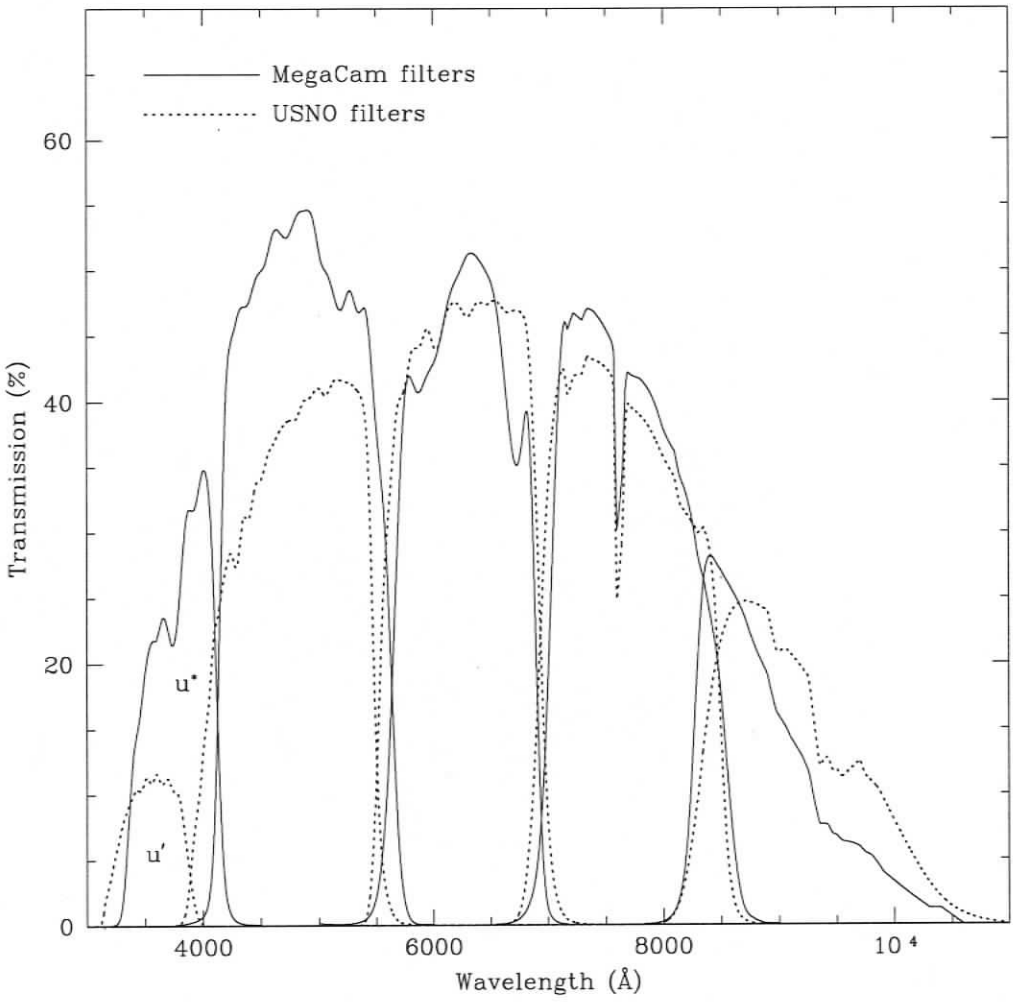

Figure 3.2: The spectral coverages of the CFHT/MegaCam $u^*g'r'i'z'$ and USNO $u'g'r'i'z'$ filter sets. Note that the effective wavelength of MegaCam's u^* filter is shifted redward by about 200Å compared to the u' filter.

but also to exploit the unique opportunity that MegaCam's sky coverage offers for detailed investigations into the large-scale properties of these clusters. Generally, a series of multiple short (5-30 s depending on filter) and long exposures (250-500 s) in each bandpass were obtained for each cluster in order to achieve high signal-to-noise ratios for stars lying on the bright and faint ends of the cluster sequences. The center of the MegaCam mosaic was positioned roughly on the cluster core for the first exposure in each series (denoted by the cross near the center of Figure 3.1) with successive exposures dithered by a few arcseconds in order to fill in the gaps between the CCDs and ensure a complete sampling of stars over the entire 1×1 degree field.

3.1.1 Observations and Data Reduction

Table 3.1 presents a list of the dates when data for the program clusters were collected on CFHT during the 2004A observing semester. The observing run identifications provided in the second column denote blocks of several consecutive nights when the same instrumental setup was in place on the telescope, and all raw science images collected during these blocks were preprocessed using the same run-averaged master bias and flat-field frames. It is important to note that, due to nature of the "queue-scheduled" mode of observing operations at CFHT, the cluster data were collected on nights when actual sky conditions at the telescope closely matched the tolerances specified in the initial project proposal (i.e., near photometric conditions during dark or grey time with moderately good seeing). As a result, the observations were generally conducted on non-consecutive nights, and a complete set of cluster observations in all five filters may not have been collected on the same night or even during the same observing run (e.g., the M 3 data were collected over 4 separate nights spanning 3 different observing runs).

A total of 287 individual MegaCam images in the $u^*g'r'i'z'$ filters was collected over the 12 separate nights listed in Table 3.1. All but one of these nights were

Table 3.1: Observing Log for the CFHT Star Cluster Survey

UT Date	Run ID	u^*	g'	r'	i'	z'	Clusters Observed	Photometric?
2004-05-13	04AM04	7	0	0	0	0	M 92	Y
2004-05-23	04AM05	20	0	0	0	10	M 92, M 3	Y
2004-06-10	04AM06	0	10	10	10	0	M 92	Y
2004-06-11		5	10	10	10	0	M 3	Y
2004-06-14		0	0	0	8	0	M 3	N
2004-06-19		0	10	10	10	0	NGC 6791	Y
2004-07-07	04AM07	8	6	0	0	0	NGC 6791, M 13	Y
2004-07-08		0	10	10	10	0	M 71	Y
2004-07-10		10	0	0	0	12	NGC 6791	Y
2004-07-13		10	0	0	0	10	M 71	Y
2004-07-16		10	10	10	10	10	M 13	Y
2004-07-17		3	8	0	0	0	M 3, M 5	Y
		73	**64**	**50**	**58**	**42**		

deemed photometric on the basis of the observing logs, observer's notes, and weather conditions at the Mauna Kea site with atmospheric seeing conditions ranging between 0.54″ and 1.45″ (FWHM; median of $\sim$ 0.93″) over all nights. While all the clusters listed in Table 1.1 were included in the survey, not all of them were actually observed. This is indicated in Table 3.2 where a listing of the number of short and long exposure images per filter that were obtained on a cluster-by-cluster basis is provided. Unfortunately, M 67 was not observed during this period, while only 8 g' frames were taken for M 5. As a result, these two clusters are excluded from consideration for the remainder of the analysis. In addition, the 8 i' images for M 3 obtained during non-photometric conditions were also excluded from the data reductions. This leaves 271 MegaCam images remaining to be processed in the analysis below.

It is important to note that all of the raw science images acquired for this investigation were preprocessed by CFHT's Elixir project (Magnier & Cuillandre 2004) prior to their distribution to the author. This involved the standard steps of over-

Table 3.2: The number of $u^*g'r'i'z'$ exposures obtained per cluster

Cluster	u^*	g'	r'	i'	z'
M 92	17	10	10	10	10
M 13	10	16	10	10	10
M 3	18	10	10	10	0
M 5	0	8	0	0	0
M 71	10	10	10	10	10
M 67	0	0	0	0	0
NGC 6791	18	10	10	10	12

scan correction, bias subtraction, flat-fielding (using run-averaged twilight sky flats), masking of bad pixels, and fringe removal from the i' and z' images. The Elixir project also provides a preliminary astrometric calibration and photometric analysis for each MegaCam image. The latter involves a normalization of the background level in each CCD to enforce a nearly identical instrumental zero-point for all chips and ensure that the final processed data show only small variations from a constant background over the entire mosaic.

As a result of the processing done by Elixir, the data analysis could proceed directly to the extraction of the instrumental PSF photometry from each MegaCam image. In this respect, no attempt was made prior to these reductions either to combine the 36 different CCD images into a single master exposure or to co-add the dithered exposures, but rather each CCD from every MegaCam image was processed separately as if they came from distinct cameras. This is advantageous since the act of assembling multiple CCDs into a large mosaiced image often requires the "resampling" of the individual images to account for subtle chip-to-chip differences in scale and rotation. This type of processing generally requires pixel interpolations and extrapolations that can distort the PSF in certain regions of the mosaic and may lead to spurious photometry for some objects during the PSF fitting.

Since the reduction of the CFHT images is conducted in a manner similar to

that described in Section 2.2.2, only a brief review is provided here. First, a UNIX shell script was employed to non-interactively run the PSF-building and star subtraction DAOPHOT/ALLSTAR routines on each individual CCD frame. In order to save computational time, only the center six CCDs from each MegaCam image (i.e., ccd13-ccd15 and ccd21-ccd23; see Figure 3.1) were reduced due to the fact that they contain the vast majority of cluster members and cover approximately the same region of sky as the secondary standard stars (see Figure 3.1). Therefore, the DAOPHOT/ALLSTAR reductions was performed on a total 1626 individual 2048×4612 CCD images; this required approximately 31 CPU days on a 1.8 GHz AMD PC. After star lists and associated instrumental PSF photometry for each frame had been derived, the correction of the relative profile-fitted photometry to a more absolute, aperture-based system was accomplished with concentric aperture growth curves derived using the DAOGROW package. Finally, the geometric transformations of the natural (x, y) coordinate system of the individual CCD images to an astrometrically meaningful system based on the USNOB-1.0 catalogue is accomplished via a set of third-order polynomials. In the end, magnitude and positional information was derived for some 16.9 million star images in the 1626 CCD images.

3.1.2 Calibrating the Cluster Photometry

As a result of the efforts described in Chapter 2, each star cluster in the CFHT survey contains a sizable number of local standard stars whose magnitudes have been referred to the $u'g'r'i'z'$ system with an accuracy of 1% or better in each filter. Therefore, calibrating the cluster photometry relies solely on comparing the observed instrumental magnitudes for these stars to their counterparts on the standard system in order to solve for the transformation coefficients using robust least-squares analysis. In the beginning stages of the calibration process, each CCD exposure from the mosaic was treated separately. That is, the transformation constants were allowed to

be determined freely and independently on the basis of the local standard stars contained in the image. Unfortunately, since the range in air mass spanned by the cluster observations on any given night was typically quite small ($\Delta(sec\, z) \lesssim 0.2$), it was soon discovered that the derived extinction coefficients often took on non-positive values and/or were wildly inconsistent between the different CCD images. Due to these findings, the canonical atmospheric extinction coefficients for Mauna Kea (as determined by the Elixir project) were employed for the calibrations rather than having them computed from the data. Namely, all chips are assigned $K_{u'} = 0.35$, $K_{g'} = 0.15$, $K_{r'} = 0.10$, $K_{i'} = 0.04$, and $K_{z'} = 0.03$ mag per air mass for all photometric nights.

With the extinction coefficients set to constant values for all chips, secondary runs through the calibrations were performed with one less unknown in the transformation equations. Upon completion, a weighted average of the linear color terms was then calculated and imposed as an additional known constant common to all chips for a final calibration run that left only the photometric zero points to be recomputed on a chip-by-chip basis. Given the fact that the spectral response of a telescope/detector system was largely determined by the combined effects of the transmission of the atmosphere, the reflectivity and transmissivity of the telescope components, and throughput of the filters, it can be expected that chip-to-chip differences in the computed color terms vary by only a few percent (provided that the CCDs are similar in design and the filter is spatially uniform). Indeed, the largest variations in the color coefficients between the different chips from any single photometric night amounted to $\sim 4\%$ observations in the u' filter.

Once the transformation constants from all nights were derived, the best estimates of the calibrated magnitudes for each secondary standard star observed over all 11 photometric nights were then determined. Figures 3.3 and 3.4 illustrate the extent to which the cluster data have been placed on the standard system by comparing the $u'g'r'i'z'$ photometry to the mean calibrated photometry for the secondary standards stars. The small, grey data points in each panel represent the difference between the

magnitude on the standard $u'g'r'i'z'$ system and the *mean* magnitude as a function of their respective magnitudes in Figure 3.3 and $(g' - i')$ color in Figure 3.4. To better aid in the detection of any systematic trends not immediately evident to the eye, each large dot represents the unweighted median difference for stars in intervals of 1.0 in magnitude or 0.5 mag in $(g' - i')$ color with their corresponding error bars providing a robust measure of the spread in the residuals within each bin (i.e., $(\pi/2)^{1/2}$ times the mean absolute deviation).

A few features in both figures bear detailed explanations. First, there is a noticeable excess of scatter in the data points towards negative values in each panel of Figure 3.3; this seems to indicate that a sizable fraction of the secondary standards with $r' \gtrsim 15$ have had their magnitudes on the standard system measured too bright compared to the values derived here. The most likely explanation for this effect is the fact that these standards are probably located closer to cluster cores and hence their photometry has been "contaminated" by light from nearby stars in the DAO images. This would serve to make the secondary standards appear brighter than they actually are. Given that atmospheric seeing conditions averaged around $3-4''$ at the DAO, it is reasonable to expect a higher probability of spurious photometry resulting from the effects of crowding in the DAO images compared to the CFHT observations (with average seeing values of $\sim 1.0''$). Reassuringly, however, the median magnitude differences tend to hover within 0.01 mag of zero difference over the entire ranges in g', r', i', and z' and the lines corresponding to zero difference tend to pass through the densest swarms of data points.

Secondly, the situation with the u' magnitude differences plotted as a function of color in the top panel of Figure 3.4 appears quite troublesome. In particular, there is considerable disagreement in the residuals towards bluer and redder colors which would seem to suggest that the use of a single linear color term in the transformation equations cannot sufficiently account for the bandpass mismatch between the u^* and u' filters. As mentioned above, CFHT's u^* filter was constructed to be substantially

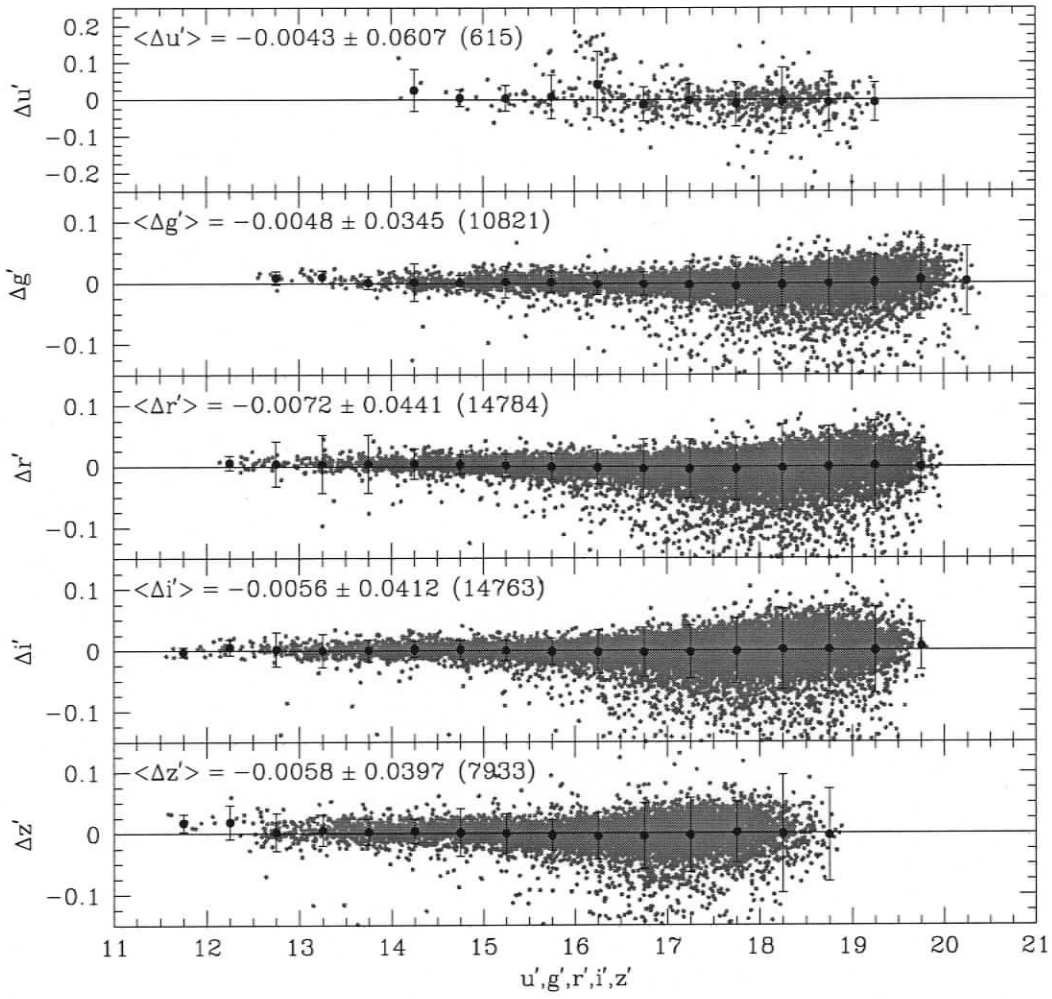

Figure 3.3: Plot of the photometric differences for stars observed over the 11 photometric nights on CFHT that also appear in the database of secondary $u'g'r'i'z'$ standards derived in Chapter 2. Each Δmag is plotted against its respective magnitude on the standard system. The small grey dots represent individual secondary standard stars in common between the two data sets while the large black circles designate the median difference in bins of 1.0 mag. The error bars associated with the median values correspond to a robust measure of the dispersion in the differences within each bin. The mean Δmag differences, associated standard deviations, and number of stars used to define the mean are denoted in each panel.

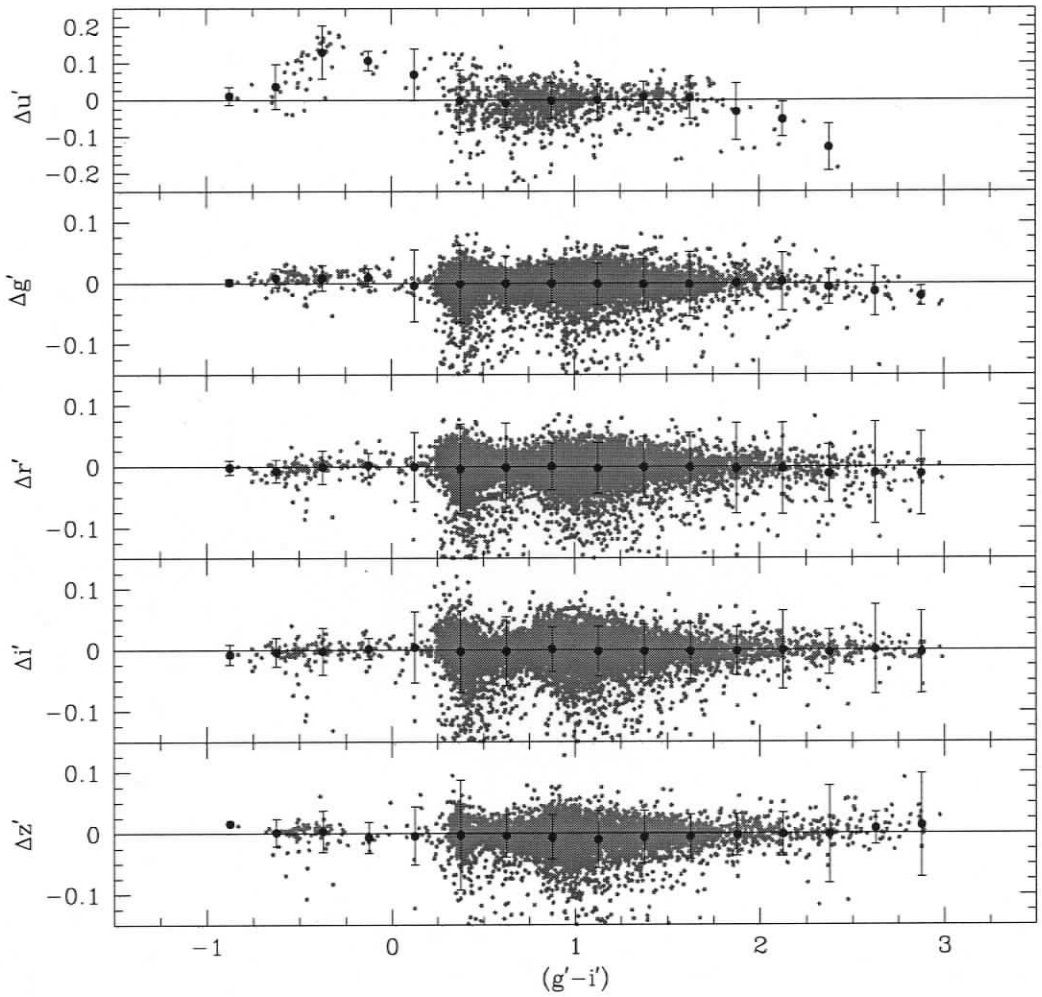

Figure 3.4: Same as Figure 3.3 except plotted against $(g' - i')$. This time each large black circle represents the median difference in bins of 0.5 mag in color. Note the strong deviations in $\Delta u'$ as a function of color in the top panel.

different than the u' filter in order to to take advantage of the good UV sensitivity of MegaCam and reduced atmospheric extinction at short wavelengths atop Mauna Kea. The effective wavelength of the u^* filter is about 220Å redder than that of u', and, as shown in Figure 3.2, this places the bulk of the u^* response *redward* of the Balmer discontinuity at 3700Å; this has profound implications for transforming the observed u^* magnitudes for B- and A-type stars (i.e., those with the largest Balmer jumps) to the standard system.

Given that the deviations seen in $\Delta u'$ at $(g' - i') \lesssim 0.0$ are so complex, together with the paucity of hotter u' secondary standards in this region of color space, it is unlikely that the inclusion of additional color terms in the photometric solutions would be sufficient to remove the discrepancies over the entire range in color. Reassuringly, however, the transformations seem to provide calibrated u' magnitudes for stars in the region $0.25 \gtrsim (g' - i') \gtrsim 2.0$ that are in quite good agreement with those on the standard system. Indeed, there appear to be no strong systematic trends in the individual data points and the median values deviate by no more than 0.02 mag from zero difference within this range. This fact bodes well for the derivation of the fiducial sequences in u' since the stars that define RGB, SGB, turnoff, and upper-MS loci for all clusters in the survey fall within this color range. It is important to stress, however, that the transformations between u^* and u' are invalid for blue horizontal branch stars or other hot stars, such as blue post-AGB stars, sdB stars, white dwarfs, or some blue stragglers.

3.2 The Cluster Photometry and Derivation of the Fiducial Sequences

The transformation terms computed during the calibration to the standard $u'g'r'i'z'$ system described in the previous section were subsequently applied to the instrumen-

tal magnitudes that were derived for all detected objects in every CCD image for each cluster field. Simultaneously, the zero points between the relative profile-fitting magnitude system and the standard one are redetermined by direct comparison to the local secondary standards within each cluster field on a frame-by-frame basis. This final step in the reduction process compensates for uncertainties caused by short term fluctuations in the extinction or errors in the aperture corrections. While this does nothing to improve the absolute calibration of the photometry to the standard system in the mean, it does improve the frame-to-frame repeatability of the measurements by ensuring that the photometry from each image is now referred to a common magnitude zero point defined by the local secondary standards. In addition, the transformation of the natural (x, y) coordinates of the stars in each image to an astrometrically meaningful system based on USNOB-1.0 catalogue facilitates the matching of stars from different chips and different exposures and results in a single master star list for the entire field surrounding each cluster. In the end, astrometric positions and $u'g'r'i'z'$ magnitudes are tabulated for almost 650,000 stars divided among 5 different star clusters.

3.2.1 Comparisons with the SDSS

The most recent SDSS data release (DR4; Adelman-McCarthy et al. 2005) includes digital imagery and five-band photometry for the globular clusters M 13 and M 3, and this provides an excellent opportunity to test the cluster photometry derived here. Before discussing the comparisons, it is important to reiterate that the cluster photometry presented here has been calibrated to the $u'g'r'i'z'$ system defined by the S02 sample of standard stars, while the SDSS photometry is on the "natural" *ugriz* system of the 2.5 m survey telescope. Therefore, it is necessary to convert the SDSS *ugriz* photometry to the $u'g'r'i'z'$ system by making use of the following empirically-determined relations (Rider et al. 2004):

$$u' = u, \tag{3.1}$$

$$g' = g - 0.060[(g - r) - 0.53], \tag{3.2}$$

$$r' = r - 0.035[(r - i) - 0.21], \tag{3.3}$$

$$i' = i - 0.041[(r - i) - 0.21], \tag{3.4}$$

$$z' = z + 0.030[(i - z) - 0.09]. \tag{3.5}$$

Figures 3.5-3.8 present the differences between the SDSS and CFHT photometry for M 13 and M 3 stars in common between the CFHT and SDSS data sets plotted as a function of magnitude and $(g' - i')$ color. Note that the comparisons for M 3 are limited to only the g', r', and i' photometry since no u' or z' data from CFHT are available for this cluster. With the exception of the $\Delta u'$ magnitudes for M 13, the $g'r'i'z'$ photometry derived here is quite consistent with that of the SDSS and there appear to be no strong systematic trends in the differences for both clusters in either magnitude or color. Indeed, the deviation in $\Delta u'$ towards more positive values at $(g' - i') \lesssim 0.0$ mirrors that shown in Figure 3.4.

3.2.2 Thinning the Sample

Given that approximately 16.9 million individual magnitude and position measurements have been derived for some 650,000 distinct objects in 1626 CCD images, it is inevitable that a sizable number of these detections will be non-stellar objects (e.g., background galaxies, cosmic rays, satellite or meteor trails, etc.) or image blemishes (e.g., defective pixels, diffraction spikes, etc.). Moreover, when dealing with crowded cluster fields such as these, the photometry for a significant fraction of the legitimate stars will undoubtedly be contaminated by light from neighbouring objects even under the most ideal seeing conditions. As a result, when the cluster photometry is plotted on color-magnitude or color-color diagrams for the purpose of analysis, these

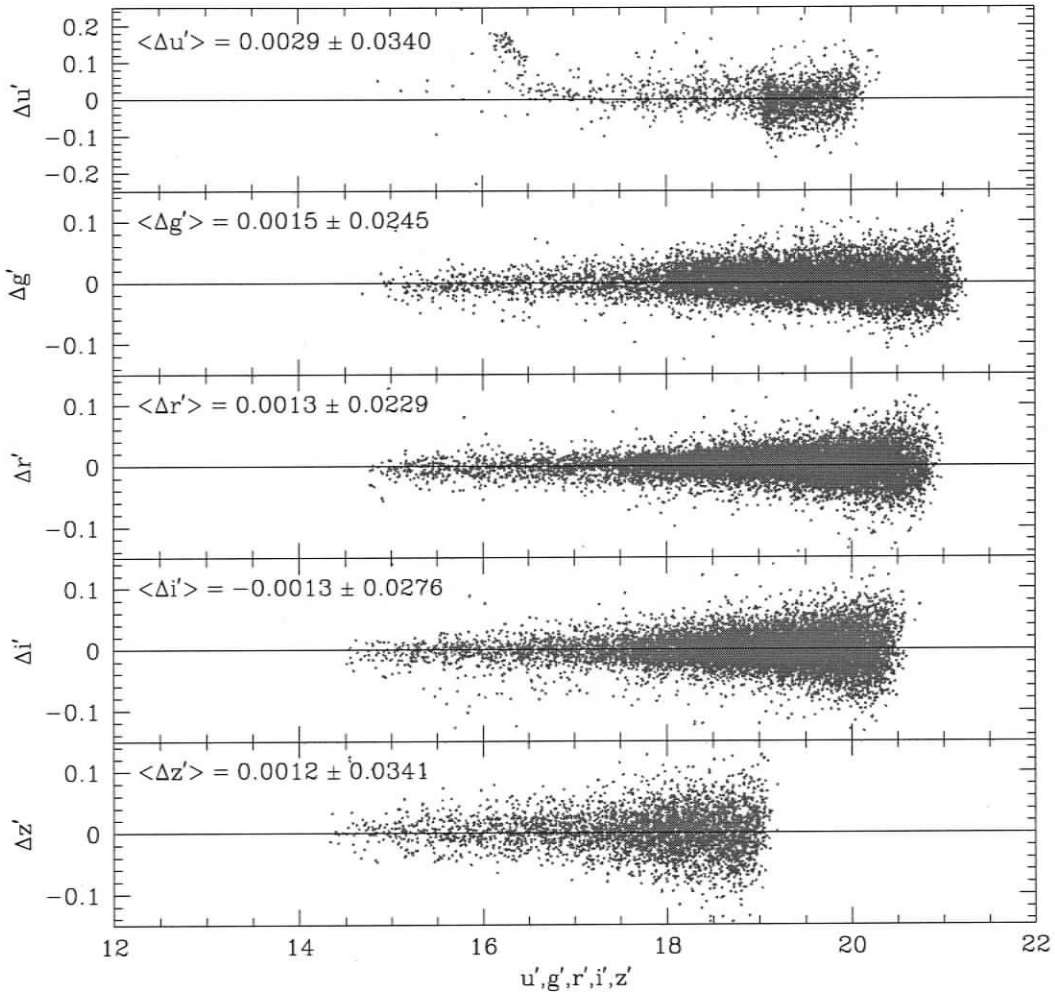

Figure 3.5: Plots of the photometric difference between the calibrated CFHT and SDSS photometric data sets (in the sense SDSS-CFHT) versus the indicated magnitudes for stars in field surrounding M 13.

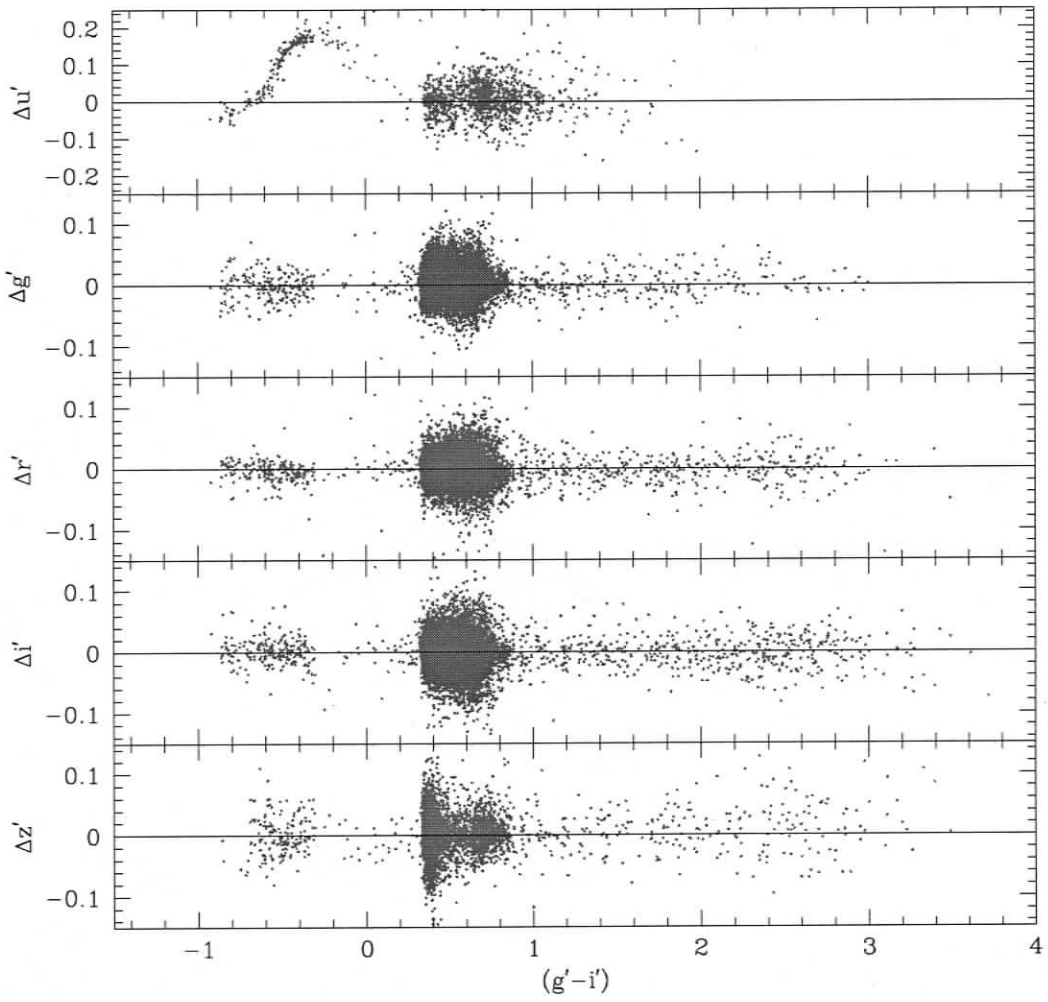

Figure 3.6: Plots of the photometric difference between the calibrated CFHT and SDSS photometric data sets (in the sense SDSS-CFHT) versus the $(g' - i')$ color for stars in field surrounding M 13

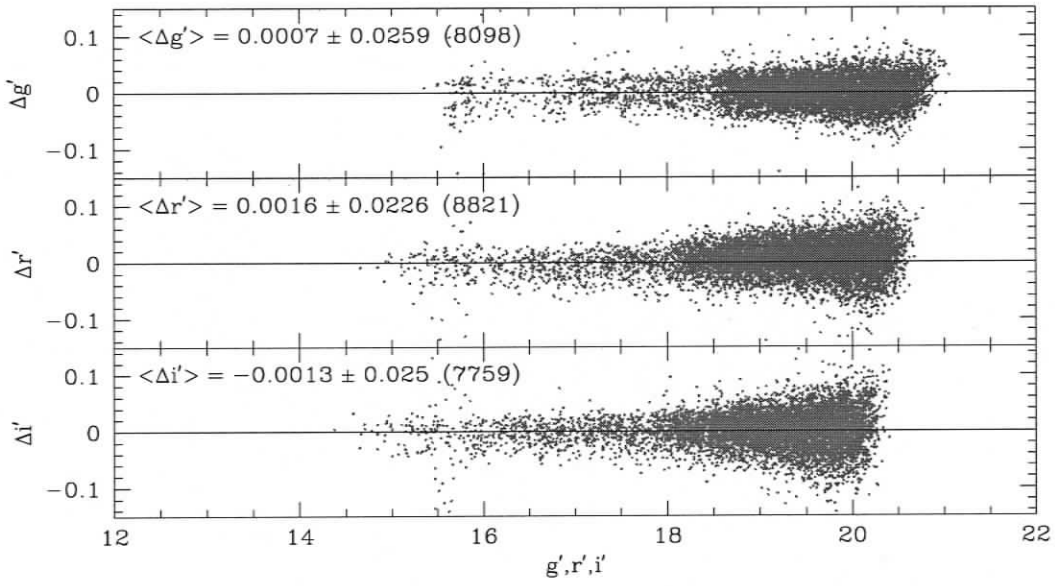

Figure 3.7: Same as Figure 3.5 but for stars in M 3. Note that only calibrated $g'i'z'$ CFHT photometry is available for this cluster.

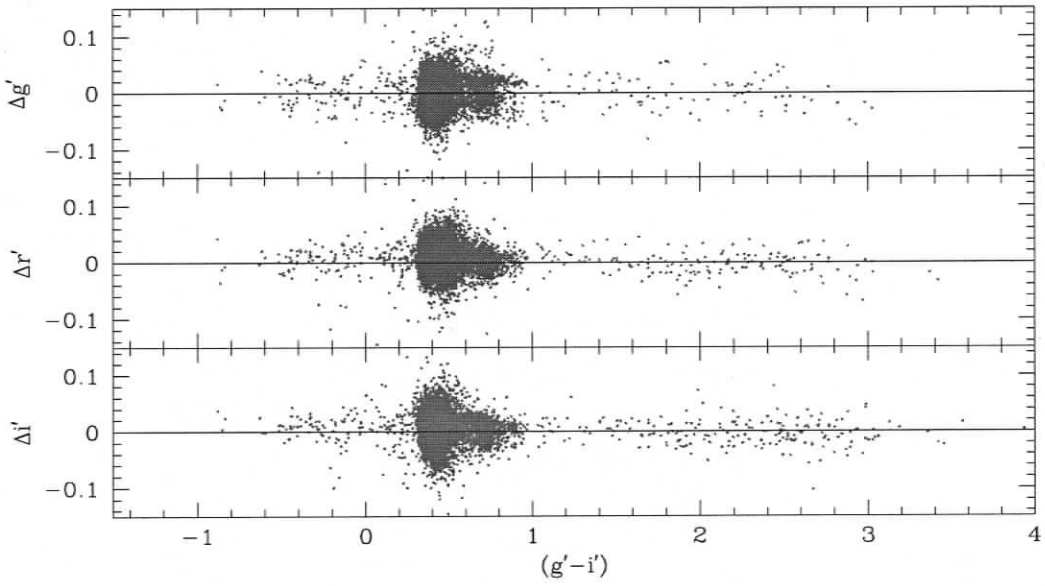

Figure 3.8: Same as Figure 3.6 but for stars in M 3.

spurious objects and crowded stars may contribute increased scatter or broadening of the primary cluster sequences, and it is better to exclude them from consideration when deriving the fiducials. While it is obviously not feasible to censor problematic measurements by hand, the various programs that have been used to extract the PSF instrumental photometry from the CCD images output certain image-quality and data-reliability indices that can be used to reject spurious detections or non-stellar objects from consideration. In addition to these indices, the discussion below describes the mechanics of the so-called "separation index" (Stetson 2003) that is quite effective in culling severely crowded stars from the cluster data sets.

In brief, the definition of the separation index is based on the fact that the typical seeing profile for each star in a particular image is well approximated by the Moffat function (Moffat 1969):

$$S(r) \propto \frac{F}{[1 + (r/r_o)^2]^\beta}, \tag{3.6}$$

where r is the distance from the star's centroid, r_o is some characteristic radius that can be related to FWHM of the stellar brightness profile, F is just the stellar flux determined from $F \propto 10^{-0.4m}$; where m is the apparent magnitude, $S(r)$ is the surface brightness of the stellar profile at radius r, and β is a parameter that governs the shape of the stellar profile. Based on this definition, if one assumes a reasonable value for β (typically 1.5–2.5 for stellar profiles in digital images) and FWHM for the seeing value, it is a simple matter to compute the surface brightness produced by a particular star with both an apparent magnitude m and a centroid position at any point in the field. Based on this definition, the *sep* index for any given star can be mathematically expressed as:

$$sep = \frac{S(0)}{\Sigma S_i(r)}. \tag{3.7}$$

Here $S(0)$ is the surface brightness at the centroid of the star in question and $S_i(r)$ is the surface brightness contribution from the i^{th} neighbouring star situated at a distance r away.

The computation of the *sep* index for the 5 different cluster data sets assumes the typical values of FWHM = 1.0″ and $\beta = 2$ and uses the apparent r' magnitude to define the fluxes for the individual stars. In order to save computational time, the determination of *sep* for any particular star in the field considers contributions only from those stars lying within 10 times the assumed FWHM. The top panel of Figure 3.9 shows the plot of the derived *sep* index versus apparent r' magnitude for stars in M 13. As evidenced by the higher concentration of points at increasing magnitudes, fainter stars are more susceptible to contamination by light from neighbouring stars in the field than bright ones. Since the M 13 turnoff corresponds to $r' \sim 18.6$, the scattering of points to brighter magnitudes and higher *sep* values primarily correspond to stars lying on the RGB and HB of this cluster. Based on examinations of the cluster CMDs using different *sep* cuts, it was determined that stars with $sep > 3.5$ produced the most well-defined cluster sequences. Therefore, the remainder of this discussion only considers those stars with *sep* values above 3.5.

During the process of deriving PSF magnitudes the DAOPHOT/ALLSTAR software computes two image-quality indices known as χ and *sharp* for every detected object in a CCD image. In the final reduction of all the data for a particular cluster, the individual χ and *sharp* measurements for each star are then averaged and reported in the data tables. Briefly, χ is simply a measure of the agreement between the object's observed brightness profile and the derived PSF model (i.e., the quality of the fit between the model PSF and the object). As shown in the middle panel of Figure 3.9, the χ values for the vast majority objects with $sep > 3.5$ in M 13 tend to cluster around $\chi \approx 1$ over the entire magnitude range which would indicate that

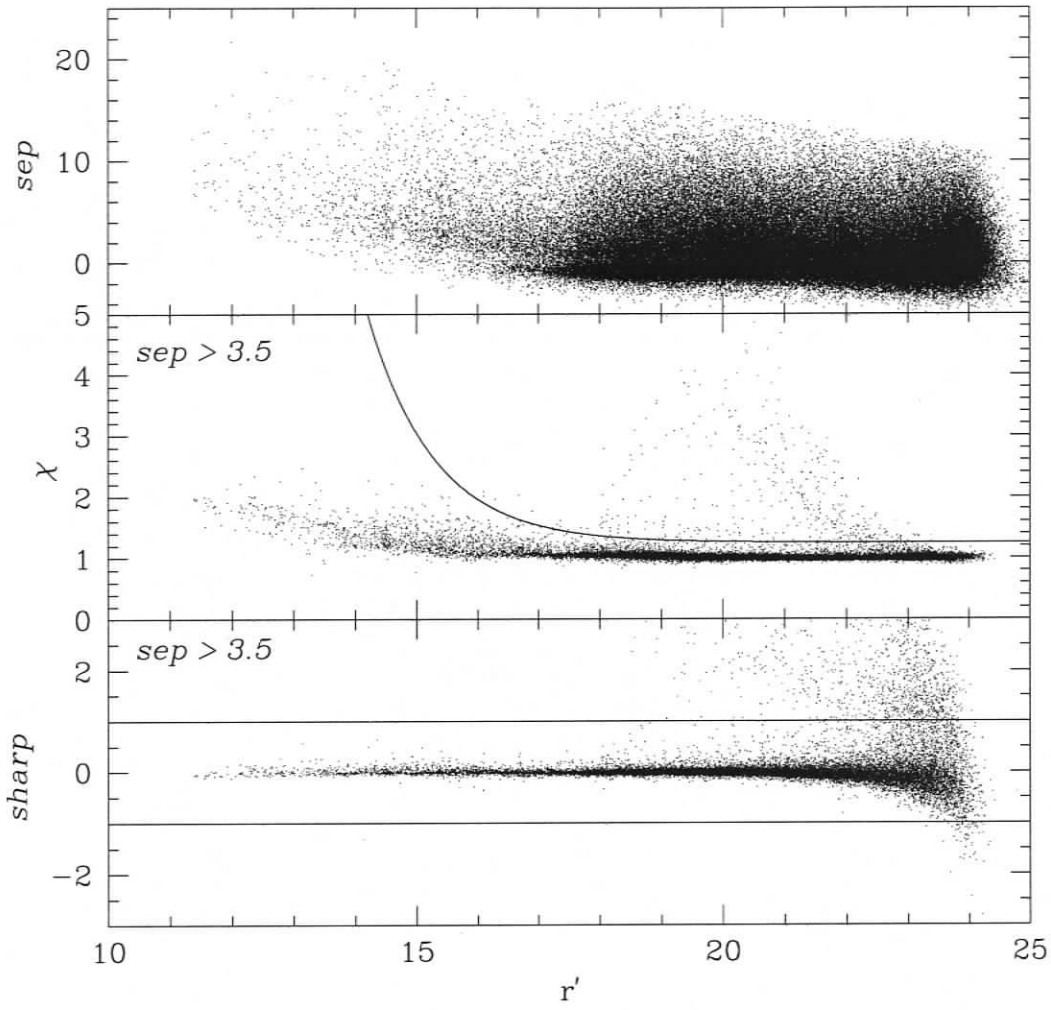

Figure 3.9: Plots of the image-isolation and image-quality indices *sep*, χ and *sharp* versus apparent r' magnitude for stars in the globular cluster M 13. Only those stars with $sep > 3.5$ are plotted in the bottom two panels. Stars lying below the solid curve in the middle panel together with those having $-1 < sharp < 1$ in the bottom panel are retained in the sample for the derivation of the cluster fiducial sequences.

they are legitimate stars. Those at larger χ values, on the other hand, are most likely either non-stellar objects or stars whose brightness profiles are corrupted by image defects or diffraction spikes. Stars lying above the solid curve shown in the same panel are excluded on the basis of the χ values. Finally, a plot of the *sharp* index versus apparent r' magnitude in the bottom panel of Figure 3.9 shows that real stars have a propensity to hover in a narrow range centered on zero. This is due to the fact that the *sharp* index measures the degree to which an object's intrinsic angular radius differs from that of the model PSF. Therefore, detections with large *sharp* values have large characteristic radii compared to the PSF model and are most likely resolved galaxies, while those with small *sharp* have comparatively small radii and probably correspond to an image blemish or cosmic ray. As a result, one can safely assume that objects with $|sharp| < 1$ have a high degree of probability of being real stars.

To demonstrate the effectiveness of the χ, *sharp*, and *sep* indices in culling crowded stars and spurious objects from the photometry lists and producing extremely well-defined cluster sequences, Figure 3.10 shows two CMDs for M 13 with those stars that survived the cuts plotted in the left-hand panel and those that did not in the right. Note the well-defined and very tight cluster sequences extending from the RGB to the lower main sequence in the left-hand panel. In contrast, stars that were excluded in the right-hand panel result in a quite diffuse and noisy main sequence, turnoff, and lower-RGB regions due largely to the effects of crowding. It important to mention that while the stars plotted in the left panel do not represent a *complete* sample of all the cluster members, they do provide a suitable *representative* sample for the derivation of the fiducial sequences.

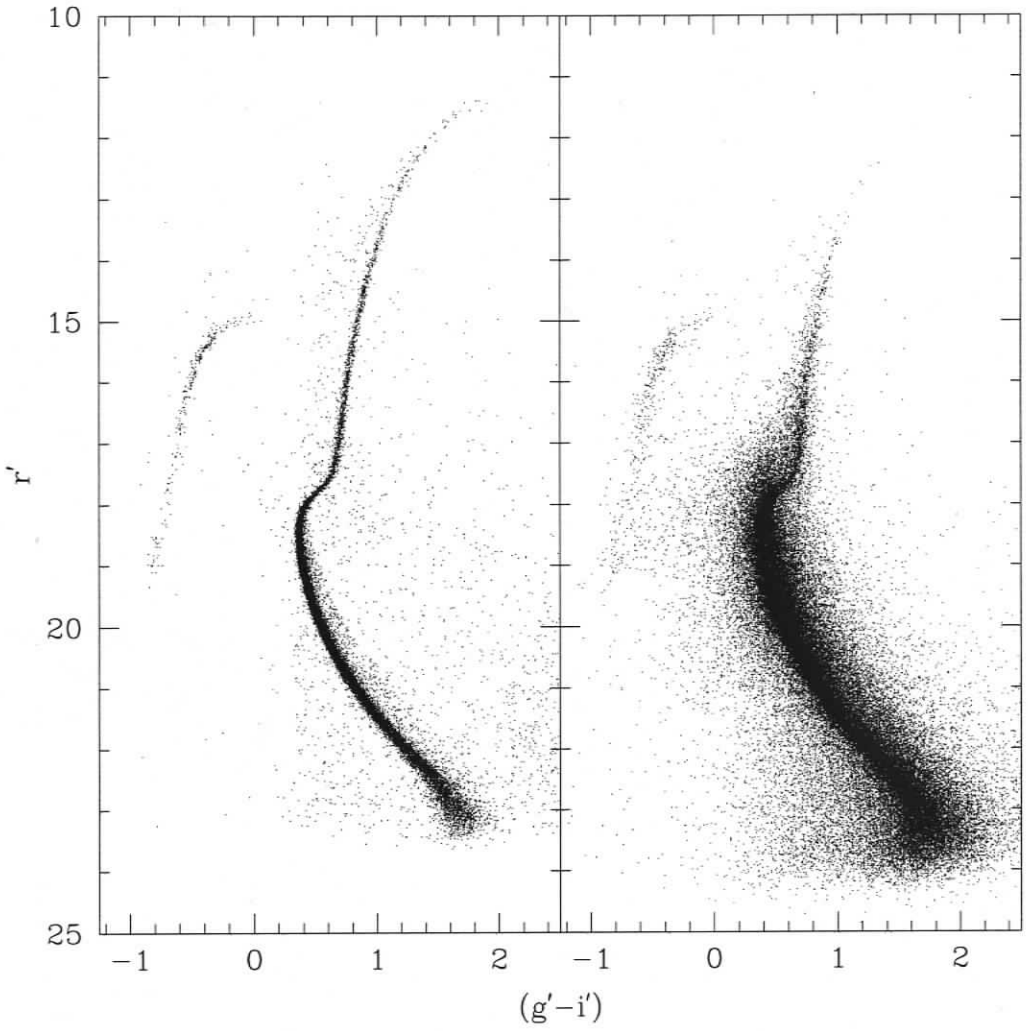

Figure 3.10: Two $(g' - i', r')$ CMDs for stars in the field surrounding the globular cluster M 13. The left-hand panel plots those stars judged to have the highest quality $u'g'r'i'z'$ photometry on the basis of their *sep*, χ, and *sharp* values as described in the text. The right-hand panel presents stars that are excluded from the deviation of the fiducial sequences due to their poorer photometry. Note the diffuse nature of the primary cluster sequences in this panel.

3.2.3 Defining the Fiducials

With objects from each of the cluster data files rejected or accepted according to the cuts in χ, *sharp*, and *sep* mentioned above, the definition of the fiducial sequences from the cluster photometry proceeds by defining the ridge lines of the stellar locus in color-magnitude space. Due to the various possible combinations of different colors and magnitudes that are available to plot for a cluster's CMD, the r' magnitude is adopted as the primary ordinate against which the median colors are defined since the cluster loci are rarely double valued in r', and the level of completeness at faint magnitudes is the best for r'. Therefore, each ridge line is created by determining the median color of stars that lie within different r' magnitude bins. The size of these bins is arbitrarily adjusted along the cluster locus to include a sufficient number of stars to define a median color. For example, larger magnitude bins are defined in parts of the CMD where the photometric scatter is larger at the faint end and where the number of stars is scarce at the bright end. Smaller bins are employed for areas of the cluster loci with large curvature and numerous stars (e.g., between the turnoff and base of the RGB). Outlying stars are iteratively clipped during the determination of the median color to ensure that the ridge line is not significantly skewed. While this technique seemed to work quite well, there were some regions of the CMD where the number of stars is just too small, the scatter in the sequences is too large, or the cluster locus is double valued (i.e., the subgiant branch of NGC 6791) for an accurate median color to be defined; in these cases the location of the points defining the ridge lines are determined by eye estimation.

Figures 3.11 through 3.15 present the various CMDs of each cluster in the sample along with their associated ridge lines spanning the MS, SGB, and RGB (tabulated in Tables 3.3-3.7). It is important to note that the photometry for each cluster has been censored according to the same χ, *sharp*, and *sep* cuts mentioned above before plotting. In addition, only those stars that lie within a radius of $\sim 2.5'$ and $\sim 5.0'$ of

the centers of M 71 and NGC 6791, respectively, have been plotted to help reduce field star contamination in their CMDs. Indeed, the imposed cuts appear to have been quite successful in yielding extremely well-defined and tight loci of stars extending from the clusters' upper-RGB down to approximately 4 magnitudes below the turnoff points.

3.3 Summary

Using high-quality, homogeneous observations of Galactic clusters spanning a wide range in metallicity, fiducial sequences in the $u'g'r'i'z'$ photometric system have been derived that range from the upper-RGB down to the lower main sequence. The fiducial sequences can serve as a valuable tools for the interpretation of other stellar population investigations involving the $u'g'r'i'z'$ bandpasses by virtue of the fact that they represent a set of empirical isochrones for both metal-poor and metal-rich stars having a wide range of physical parameters. Moreover, they provide an excellent data set to test the accuracy of color-temperature relations that have been derived from model atmospheres and synthetic spectra. The following chapter presents the details behind the deviation of these transformations along with the quality of the fits of evolutionary model isochrones to the data.

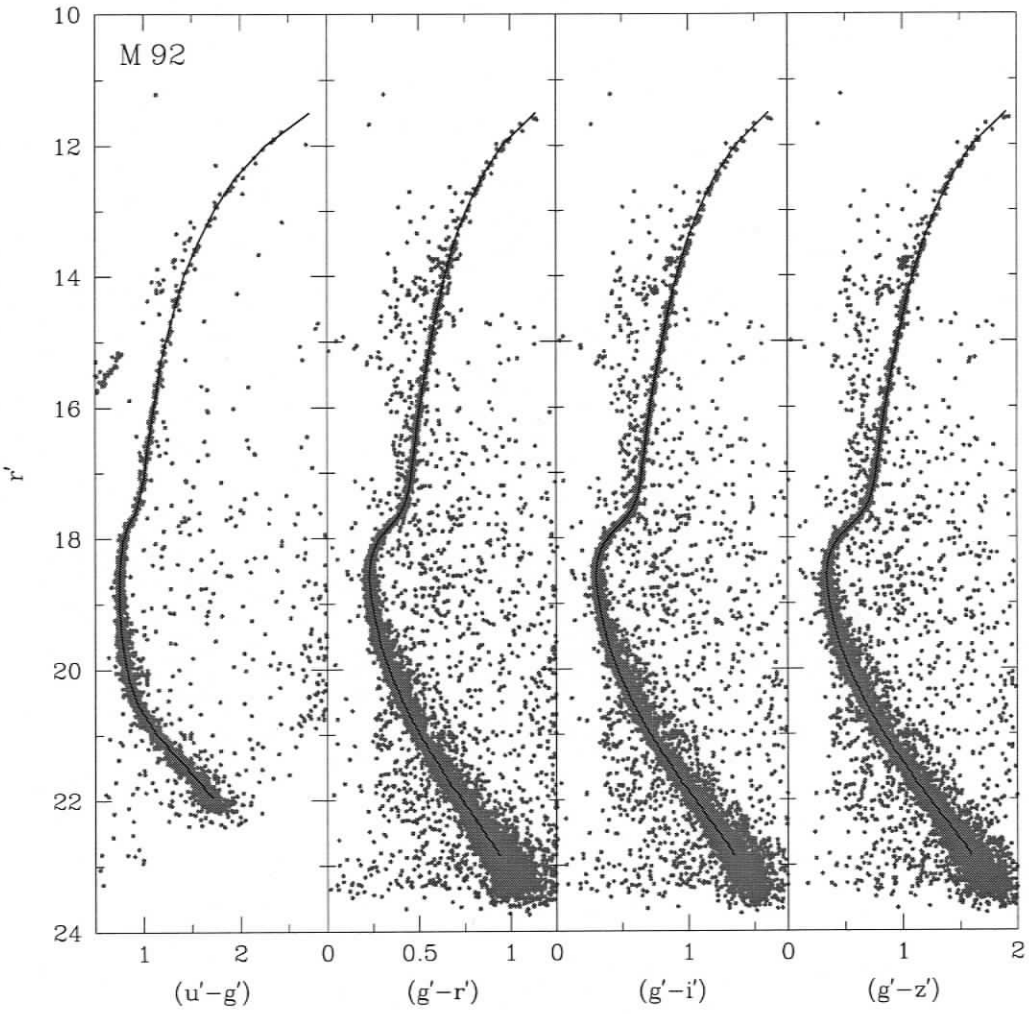

Figure 3.11: The various $u'g'r'i'z'$ CMDs and associated derived fiducial sequences for the globular cluster M 92. Note that each panel includes only those stars judged to have the highest quality photometry based on their values of χ, *sharp*, and *sep*.

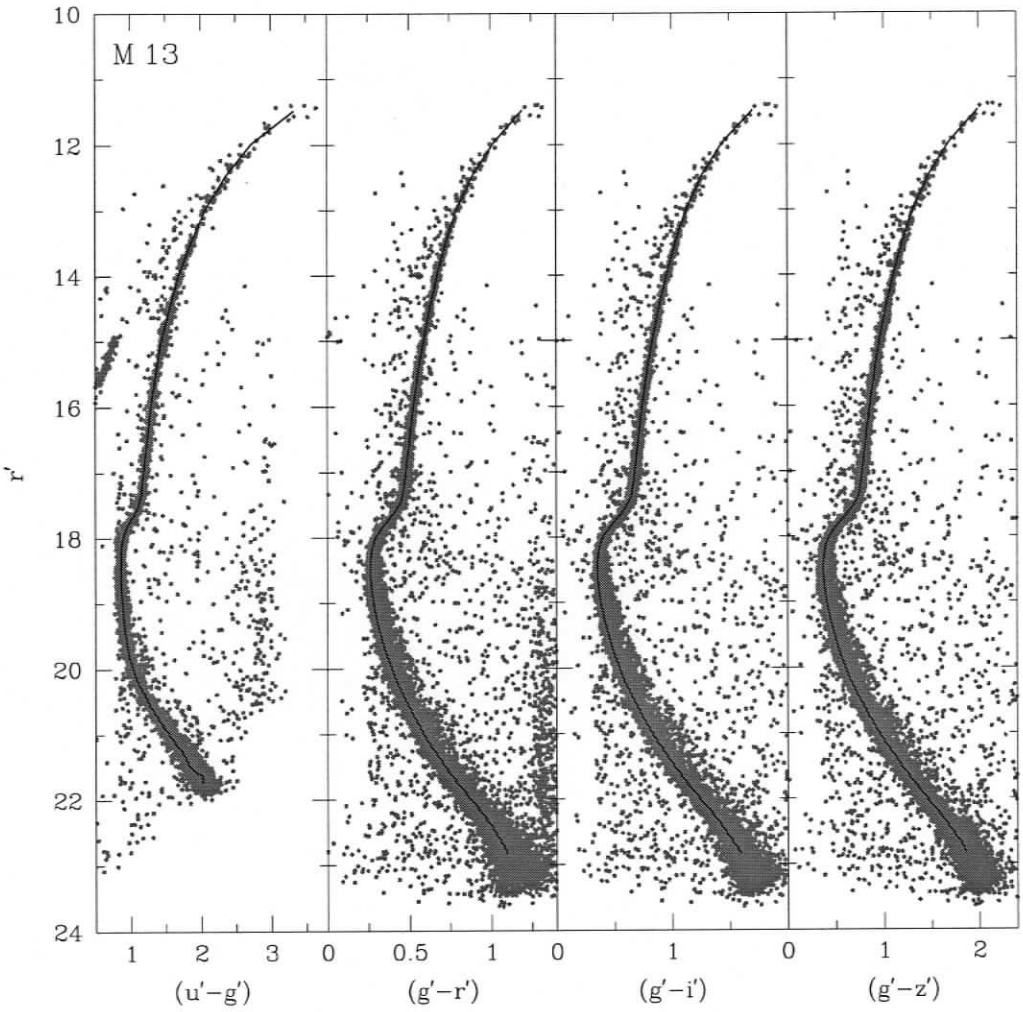

Figure 3.12: The same as Figure 3.11, but for M 13.

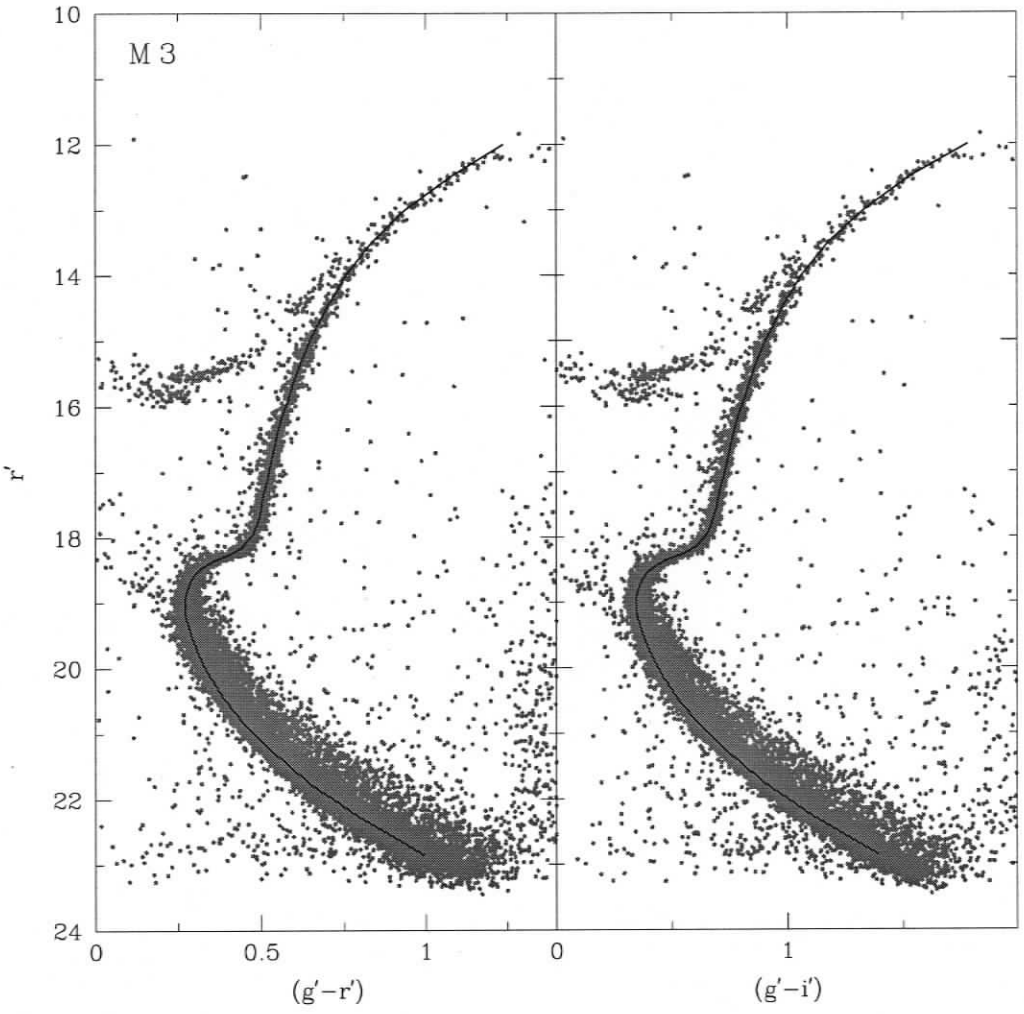

Figure 3.13: The same as Figure 3.11, but for M 3. Note that only $g'r'i'$ photometry is available for this cluster.

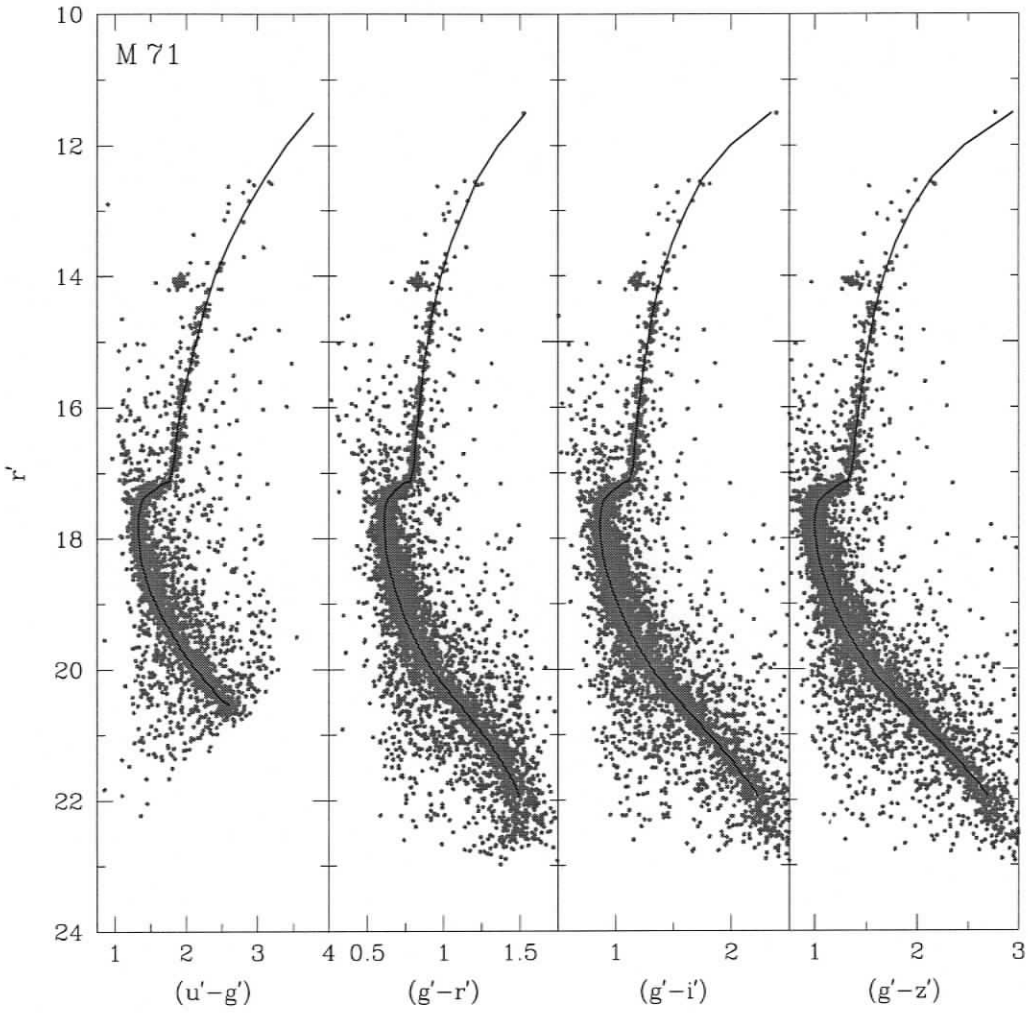

Figure 3.14: The same as Figure 3.11, but for M 71. Note that each panel plots only those stars that lie within a radius of $\sim 2.5'$ from the cluster center in order to reduce field star contamination in the CMDs.

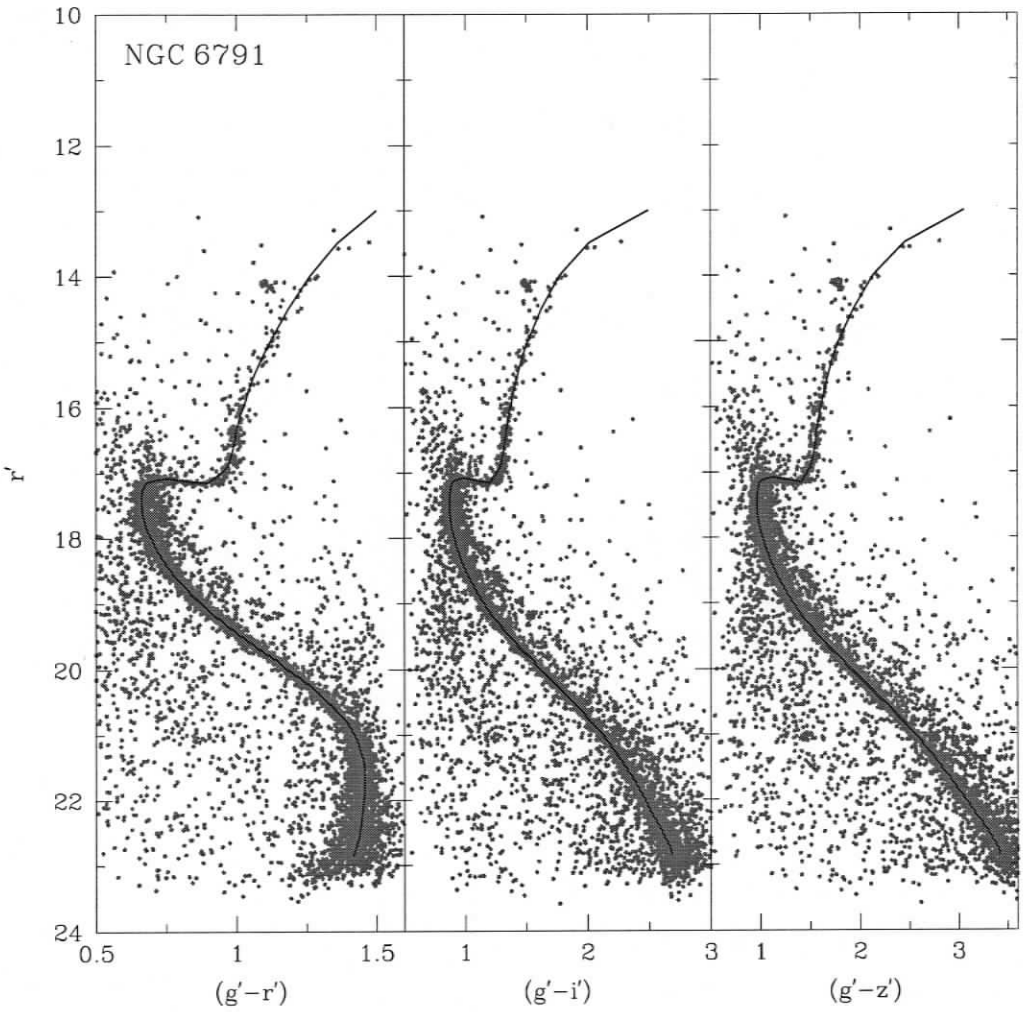

Figure 3.15: The same as Figure 3.11, but for NGC 6791. u' photometry is not available for this cluster. Note that each panel plots only those stars that lie within a radius of $\sim 5'$ from the cluster center in order to reduce field star contamination in the CMDs.

Table 3.3: Ridge line for globular cluster M 92

u'	g'	r'	i'	z'
15.360	12.640	11.500	11.032	10.732
15.293	13.343	12.500	12.143	11.918
15.750	14.190	13.500	13.204	13.016
16.421	15.101	14.500	14.248	14.086
16.893	15.683	15.125	14.892	14.743
17.300	16.150	15.625	15.407	15.267
17.713	16.623	16.125	15.918	15.787
18.141	17.101	16.625	16.428	16.305
18.579	17.579	17.125	16.938	16.824
18.676	17.696	17.250	17.065	16.956
18.827	17.877	17.450	17.273	17.170
18.940	18.040	17.650	17.494	17.403
19.011	18.181	17.850	17.722	17.647
19.113	18.326	18.050	17.951	17.898
19.265	18.495	18.250	18.169	18.128
19.439	18.683	18.450	18.376	18.340
19.630	18.880	18.650	18.576	18.540
19.838	19.088	18.850	18.773	18.737
20.049	19.299	19.050	18.968	18.929
20.273	19.512	19.250	19.161	19.118
20.501	19.729	19.450	19.354	19.304
20.736	19.946	19.650	19.544	19.488
20.978	20.168	19.850	19.732	19.668
21.231	20.394	20.050	19.920	19.848
21.495	20.623	20.250	20.105	20.024
21.773	20.853	20.450	20.290	20.200
22.082	21.089	20.650	20.472	20.372
22.406	21.326	20.850	20.655	20.543
22.741	21.565	21.050	20.837	20.714
23.095	21.807	21.250	21.017	20.882
23.481	22.057	21.450	21.196	21.047
23.843	22.300	21.650	21.376	21.215
24.198	22.547	21.850	21.553	21.380
24.797	22.797	22.050	21.731	21.545
25.047	23.047	22.250	21.912	21.713
25.297	23.297	22.450	22.086	21.868
25.545	23.545	22.650	22.264	22.028
25.789	23.789	22.850	22.447	22.195

Table 3.4: Ridge line for globular cluster M 13

u'	g'	r'	i'	z'
16.003	12.674	11.480	10.978	10.681
15.722	13.368	12.480	12.111	11.894
16.076	14.206	13.480	13.177	13.006
16.672	15.110	14.480	14.223	14.082
17.105	15.686	15.105	14.868	14.739
17.498	16.153	15.605	15.380	15.258
17.907	16.625	16.105	15.891	15.777
18.332	17.102	16.605	16.401	16.295
18.756	17.580	17.105	16.911	16.810
18.859	17.697	17.230	17.040	16.942
19.013	17.882	17.430	17.249	17.156
19.096	18.037	17.630	17.471	17.402
19.114	18.168	17.830	17.699	17.652
19.203	18.319	18.030	17.928	17.897
19.367	18.498	18.230	18.137	18.114
19.558	18.693	18.430	18.342	18.321
19.756	18.893	18.630	18.540	18.519
19.974	19.102	18.830	18.736	18.712
20.197	19.313	19.030	18.930	18.903
20.431	19.529	19.230	19.122	19.090
20.671	19.749	19.430	19.313	19.275
20.924	19.972	19.630	19.503	19.459
21.184	20.197	19.830	19.691	19.638
21.472	20.426	20.030	19.879	19.817
21.776	20.658	20.230	20.064	19.992
22.119	20.896	20.430	20.248	20.164
22.461	21.138	20.630	20.428	20.328
22.817	21.380	20.830	20.609	20.495
23.186	21.623	21.030	20.788	20.659
23.589	21.876	21.230	20.966	20.820
23.949	22.132	21.430	21.141	20.978
24.409	22.389	21.630	21.317	21.137
24.670	22.650	21.830	21.493	21.293
24.935	22.915	22.030	21.663	21.447
25.200	23.180	22.230	21.834	21.603
25.458	23.438	22.430	22.004	21.754
25.707	23.687	22.630	22.176	21.905
25.948	23.928	22.830	22.339	22.076

Table 3.5: Ridge line for globular cluster M 3

g'	r'	i'
13.238	12.000	11.454
13.938	13.000	12.604
14.757	14.000	13.695
15.648	15.000	14.742
15.991	15.375	15.130
16.458	15.875	15.644
16.926	16.375	16.157
17.404	16.875	16.667
17.667	17.150	16.950
17.857	17.350	17.153
18.051	17.550	17.358
18.241	17.750	17.566
18.426	17.950	17.773
18.591	18.150	17.990
18.709	18.350	18.230
18.852	18.550	18.460
19.031	18.750	18.670
19.220	18.950	18.876
19.421	19.150	19.074
19.632	19.350	19.270
19.843	19.550	19.462
20.058	19.750	19.654
20.277	19.950	19.844
20.498	20.150	20.035
20.724	20.350	20.223
20.952	20.550	20.410
21.184	20.750	20.596
21.419	20.950	20.779
21.661	21.150	20.960
21.904	21.350	21.142
22.148	21.550	21.322
22.396	21.750	21.501
22.655	21.950	21.678
22.913	22.150	21.853
23.176	22.350	22.028
23.444	22.550	22.201
23.711	22.750	22.370

Table 3.6: Ridge line for globular cluster M 71

u'	g'	r'	i'	z'
16.820	13.040	11.500	10.692	10.092
16.826	13.726	12.500	11.970	11.580
17.150	14.550	13.500	13.058	12.760
17.692	15.432	14.500	14.102	13.841
18.122	16.012	15.125	14.744	14.499
18.485	16.485	15.625	15.257	15.020
18.871	16.961	16.125	15.766	15.539
19.288	17.438	16.625	16.272	16.055
19.672	17.907	17.125	16.789	16.580
19.489	17.939	17.250	16.944	16.765
19.446	18.076	17.450	17.184	17.041
19.596	18.262	17.650	17.393	17.260
19.794	18.462	17.850	17.595	17.462
20.011	18.668	18.050	17.793	17.656
20.239	18.879	18.250	17.990	17.849
20.491	19.096	18.450	18.180	18.035
20.767	19.319	18.650	18.368	18.216
21.056	19.543	18.850	18.556	18.396
21.381	19.774	19.050	18.742	18.573
21.693	20.003	19.250	18.925	18.745
22.042	20.242	19.450	19.109	18.918
22.397	20.487	19.650	19.293	19.088
22.774	20.735	19.850	19.471	19.248
23.168	20.988	20.050	19.651	19.413
23.584	21.254	20.250	19.825	19.565
24.011	21.521	20.450	19.998	19.717
23.793	21.793	20.650	20.165	19.858
24.064	22.064	20.850	20.332	20.002
24.329	22.329	21.050	20.496	20.140
24.585	22.585	21.250	20.656	20.277
24.842	22.842	21.450	20.814	20.407
25.093	23.093	21.650	20.978	20.547
25.333	23.333	21.850	21.135	20.684
25.555	23.555	22.050	21.300	20.821
25.758	23.758	22.250	21.450	21.450
25.955	23.955	22.450	21.610	21.610
26.154	24.154	22.650	21.770	21.770
26.348	24.348	22.850	21.930	21.930

Table 3.7: Ridge line for open cluster NGC 6791

g'	r'	i'	z'
14.500	13.000	12.005	11.442
15.261	14.000	13.488	13.125
16.120	15.000	14.607	14.333
16.564	15.500	15.133	14.881
16.909	15.875	15.523	15.283
17.373	16.375	16.038	15.810
17.847	16.875	16.552	16.333
17.907	16.950	16.632	16.415
17.960	17.125	16.849	16.661
17.832	17.075	16.842	16.699
17.819	17.125	16.906	16.801
17.916	17.250	17.039	16.942
18.112	17.450	17.243	17.148
18.318	17.650	17.444	17.346
18.531	17.850	17.641	17.536
18.753	18.050	17.835	17.722
18.979	18.250	18.026	17.903
19.209	18.450	18.216	18.081
19.447	18.650	18.404	18.258
19.689	18.850	18.587	18.427
19.940	19.050	18.765	18.587
20.195	19.250	18.943	18.749
20.455	19.450	19.114	18.900
20.720	19.650	19.283	19.047
20.991	19.850	19.445	19.182
21.251	20.050	19.606	19.317
21.513	20.250	19.763	19.448
21.762	20.450	19.912	19.567
22.012	20.650	20.055	19.677
22.251	20.850	20.198	19.790
22.478	21.050	20.337	19.898
22.692	21.250	20.478	20.009
22.905	21.450	20.612	20.109
23.107	21.650	20.743	20.208
23.307	21.850	20.885	20.314
23.503	22.050	21.025	20.414
23.698	22.250	21.168	20.521
23.891	22.450	21.298	20.612
24.081	22.650	21.435	20.721
24.266	22.850	21.582	20.848

Chapter 4

The $u'g'r'i'z'$ Color-Temperature Relations

The analysis of photometric data for stellar populations resulting from any investigations that employ filters resembling those of the $u'g'r'i'z'$ system, such as the SDSS, requires that color-temperature relations be defined for the $u'g'r'i'z'$ bandpasses so that stellar evolutionary models can be translated to the observed color-magnitude or color-color diagrams. To provide a reliable interpretation of the data, or to test the models themselves against the observations, it is imperative that the relations employed be as accurate as possible. Arguably the most accurate color–$T_{\rm eff}$ relations come from empirical analyses where a sample of stars with well-determined physical parameters are plotted against their observed photometry to form functional relationships that predict a $T_{\rm eff}$ value corresponding to an input value of color. Indeed, numerous such relations have been derived in the past for both the $UBV(RI)_c$ and Strömgren *uvby* photometric systems (see, for example, the works of Sekiguchi & Fukugita 2000, Alonso et al. 1996; 1999, and Ramirez & Melendez 2005), among others. While these relations are generally beneficial for stars with near-solar metallicities, their extension to cooler temperatures and/or more metal-poor stars is usually

complicated by the fact that few stars in these regimes have accurately-determined $T_{\rm eff}$'s. Thus, in order to have a set of color–$T_{\rm eff}$ relations for any photometric system that are applicable to the entire HR diagram, including both Population I and II stars, it is generally better to rely upon grids of theoretically-derived colors computed from model stellar atmospheres and synthetic spectra.

Recently, VandenBerg & Clem (2004; hereafter Paper I) and Clem et al. (2004; Paper II) have shown that color-$T_{\rm eff}$ relations computed from synthetic stellar spectra for the $BV(RI)_c$ and Strömgren *uvby* systems provide inaccurate or inconsistent interpretations of the observed data for star clusters and field stars on various color-magnitude and color-color planes involving $BV(RI)_c$ or *uvby* indices, mainly at cooler temperatures ($T_{\rm eff} \lesssim 5000K$) and at higher metallicities (i.e., [Fe/H]$\gtrsim$ 0.0). They compensate for these discrepancies by applying small, empirically-based corrections to the synthetic colors to bring them into better agreement with the data. Indeed, when the color–$T_{\rm eff}$ relations are corrected in this way, they provide improved fits to the observed CMDs of both globular and open clusters, satisfy empirically determined color–$T_{\rm eff}$ relations, and match the observed photometry for stars with well-determined physical parameters. Importantly, the fits obtained between CMDs for the same clusters are remarkably consistent regardless of which color index is employed (i.e., $B-V$, $V-I$, $b-y$, etc.).

This chapter describes the computation of theoretical color–$T_{\rm eff}$ relations and bolometric corrections for the $u'g'r'i'z'$ system from Kurucz synthetic spectra. To test their accuracy, these transformations are subsequently used to translate stellar isochrones to the observed CMDs for direct comparison to the star cluster fiducial sequences that were derived in Chapter 3. The goal is to (i) identify the regions of color-magnitude and/or color-color space where the color–$T_{\rm eff}$ relations fail to provide adequate matches to the observed photometry, and (ii) assess whether the interpretation of the $u'g'r'i'z'$ results is the same as those derived from $BV(RI)_c$ and *uvby* data for the same clusters when the color–$T_{\rm eff}$ relations reported in Papers I and II

are employed.

4.1 Derivation of the Synthetic $u'g'r'i'z'$ Colors

The theoretical $u'g'r'i'z'$ colors reported here are derived using low-resolution synthetic stellar spectra computed from the one-dimensional, plane-parallel, LTE-based model stellar atmospheres of Kurucz that neglect convective overshooting (Castelli, Gratton, & Kurucz 1997). These atmosphere and spectral models assume a mixing length of $\ell/H_p = 1.25$, a micro-turbulent velocity of 2 km/s, and a standard solar abundance scale (Anders & Grevesse 1989), along with enhancements in the α-elements by [α/Fe]=+0.4 for [Fe/H]$\leq$ 0.5. Kurucz models have been used widely in the past (see, e.g., Girardi et al. 2002; 2004) to compute synthetic colors due to their broad coverage of stellar parameter space and accessibility online.[1] Moreover, the Kurucz colors for other broadband filter sets such as $UBV(RI)_C$ appear to provide a reasonably accurate representation of the observed photometry for most stars over a broad range of color (see, for example, Bessell et al. 1988).

Recall that the normalization of the $u'g'r'i'z'$ magnitudes is based on the AB system of Oke & Gunn (1983) given by:

$$AB_\nu = -2.5 \log \mathrm{f}_\nu - 48.60, \tag{4.1}$$

where f_ν is the flux of an object per unit frequency. This is essentially a monochromatic system since, by definition, an individual AB magnitude is defined for a specific frequency ν. However, measuring a magnitude through such a broad bandpass is complicated by the fact that the mean wavelength of a filter is dependent on the spectral energy distribution of the object being observed. Thus, a *broadband* AB magnitude

[1] http://kurucz.harvard.edu

is defined by as

$$m_{AB} = -2.5 \log \frac{\int f_\nu S_\nu \, d(\log \nu)}{\int S_\nu \, d(\log \nu)} - 48.60, \tag{4.2}$$

where f_ν is the flux per unit frequency of the input synthetic spectra and S_ν represents the response function for a specific filter. It is important to note that, in this type of definition, the transmission of the terrestrial atmosphere and the sensitivity of the telescope/detector combination are implicitly included in the S_ν term. Since modern CCD detectors are essentially photon counting devices, the synthetic models are converted from an energy spectrum per unit frequency (ergs cm^{-2} s^{-1} Hz^{-1}) to a photon spectrum per unit wavelength (photons cm^{-2} s^{-1} Å^{-1}) to be multiplied by the throughput of each bandpass, and integrated over wavelength to produce the expected count rate on the detector (e^- s^{-1}). The synthetic broadband AB magnitudes are then derived from Kurucz spectra using the formalism below:

$$m_{AB} = -2.5 \log \left[\frac{\int (\lambda/hc) f_\lambda S_\lambda \, d\lambda}{f_\lambda^0 S_\lambda \, d\lambda} \right], \tag{4.3}$$

where f_λ and S_λ are now expressed as a function of wavelength rather than frequency, and f_λ^0 corresponds to the reference spectrum used to define the zero point of the AB magnitude system. The color computations employ the response functions for the USNO filters as reported on the $u'g'r'i'z'$ standard star webpage[2]. These filter functions take into account both the sensitivities of the USNO telescope/CCD combination and the altitude-scaled transmission of the Earth's atmosphere. In order to place the synthetic photometry nominally on the standard system defined by S02, the theoretical magnitudes are normalized to the observed magnitudes of three F-type subdwarf stars (BD+17 4708, BD+26 2606, and BD+21 0607) relative to their syn-

[2]http://home.fnal.gov/ dtucker/ugriz/Filters/response.html

thetic counterparts as calculated using their accurate spectrophotometry reported by Fukugita et al. (1996). This ensures that there is still a formal relationship between the *broadband* $u'g'r'i'z'$ magnitudes of the standard stars and meaningful flux units.

Since the Kurucz spectra used here cover a wide range in stellar parameters, the resulting synthetic $u'g'r'i'z'$ colors are applicable to most of the HR diagram. To be specific, they are computed for cool dwarfs and giants having $5.0 \leq \log g \leq 0.0$ and $3500 \leq T_{\rm eff} \leq 6000\,K$ as well as warm dwarfs with $5.0 \leq \log g \leq 2.0$ and $6000 \leq T_{\rm eff} \leq 40000\,K$ for metallicity values of [Fe/H] = -5.0, -4.0, -3.0, -2.5, -2.0, -1.5, -1.0, -0.5, 0.0, and $+0.5$. Simple linear extrapolation is used to extend the color grids down to $T_{\rm eff} = 3000\,{\rm K}$ and to $\log g = -0.5$.

Before proceeding directly to a comparison of the synthetic colors to observational data for star clusters, it is useful to test whether the filter transmission functions adopted for the color calculations are accurate representations of the actual $u'g'r'i'z'$ bandpasses used at the USNO by S02 to establish the standard star sequences. The most obvious way to do this is to input the actual observed, flux-calibrated spectra for stars that have known standard magnitudes into Equation 4.3 to see whether the resulting *computed* $u'g'r'i'z'$ color indices provide a good match to their observed counterparts. In much the same way that observed photometry from a non-standard filter set must be transformed to the standard system via first- and second-order color terms, this synthesized photometry may show certain systematic deviations when compared to the actual observed indices that are caused by improperly determined filter functions. While the SDSS has released a large database of stars having both *ugriz* photometry and flux-calibrated spectra, it is important to remind the reader that this photometry is on the natural photometric system of the 2.5 m telescope and not on the $u'g'r'i'z'$ system defined by S02. Therefore, any such comparisons between the computed and observed photometry for these stars must be performed using the response functions for the filters on the SDSS survey telescope and not the ones used in the development of the standard star program. Indeed, Abazajian et al. (2004)

have found that there appears to be no strong systematics when these comparisons are performed. While such a database is currently unavailable for stars with observed $u'g'r'i'z'$ magnitudes, we can compare the locus of the S02 standards in color-color space to that computed from stars in the Gunn & Stryker (1983; hereafter GS83) spectrophotometric atlas. In order to account for possible degeneracies that may arise when plotting these loci in terms of one $u'g'r'i'z'$ color index versus another, Figure 4.1 employs the $B-V$ index as the abscissa for all the comparisons. The $B-V$ colors for the GS83 stars have been taken from the Lausannne Photometric Database accessed online.[3] $B-V$ indices for for the USNO standard stars, on the other hand, are primarily from the works of Landolt (1973; 1983; 1992). Fortunately, there does not appear to be any strong systematic deviations between the computed and observed $u'g'r'i'z'$ colors in any panel of the figure which would would indicate that the filter functions have been grossly mismeasured. This does not preclude the fact that some slight differences may still exist at the imperceptible level, and, until observed $u'g'r'i'z'$ photometry for GS83 stars and/or flux-calibrated spectra for the S02 standards become available, one cannot be completely certain that the synthetic colors derived in the present study are placed *exactly* on the standard system.

4.2 The Theoretical $u'g'r'i'z'$ Color-$T_{\rm eff}$ Relations

The computations described above yield an extensive grid of theoretical color–$T_{\rm eff}$ relations and bolometric corrections for the $u'g'r'i'z'$ system that cover a broad range in both effective temperature ($T_{\rm eff}$) and surface gravity ($\log g$), as well as metal abundance ([Fe/H]). As mentioned above, these transformations are necessary to translate stellar evolutionary models to observed color-magnitude or color-color diagrams. Therefore, the most obvious way to check the accuracy of the newly calculated $u'g'r'i'z'$ colors is to assess how well they reproduce the observed photometry of real

[3] http://obswww.unige.ch/gcpd/gcpd.html

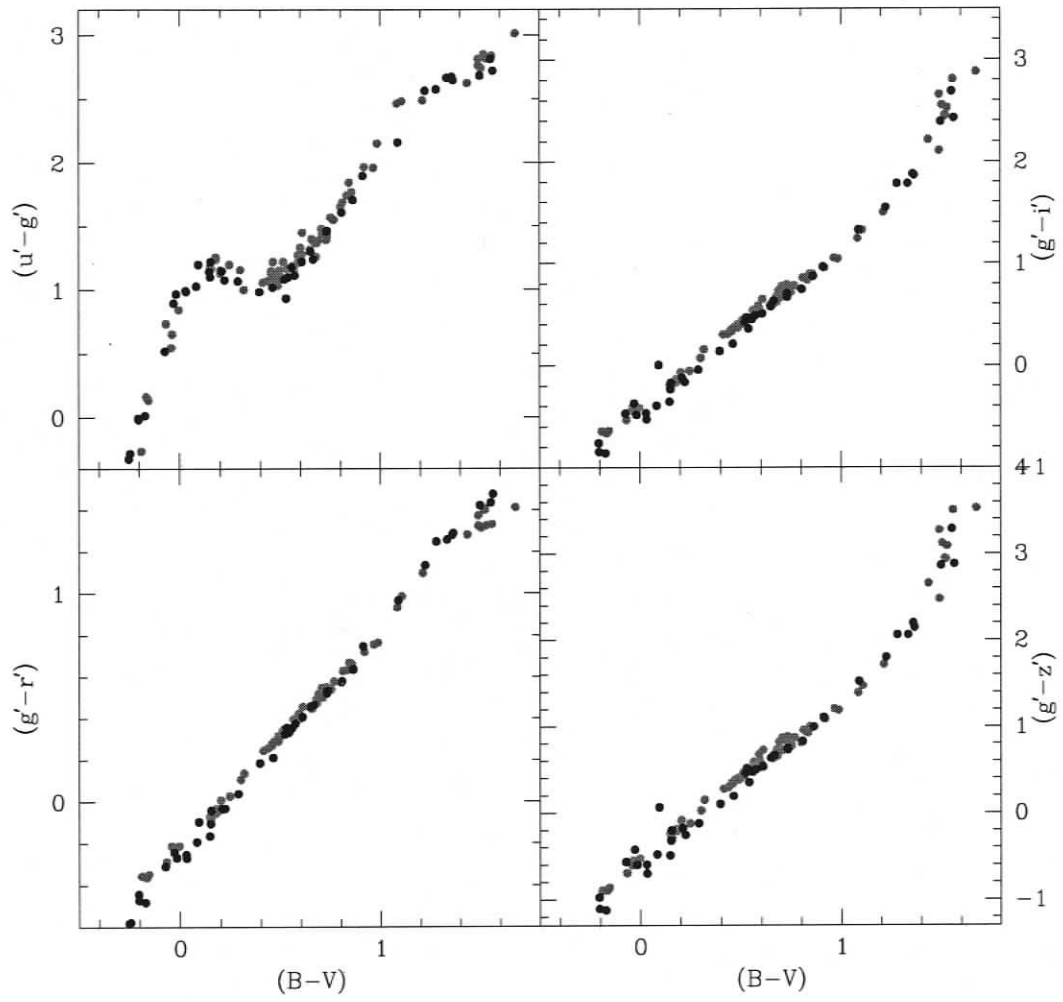

Figure 4.1: Color-color plots comparing the loci of $u'g'r'i'z'$ standard stars from S02 (grey circles) to the computed photometry for the stars in the GS83 spectrophotometric atlas (black circles). Note that $B - V$ colors are used for the abscissae.

stars. In this sense, the star cluster fiducials derived in the previous chapter offer the best constraints since they have been defined from a sample of clusters that span a broad range in [Fe/H] and extend over a wide range in both color and magnitude. Provided the temperature scales of the stellar models are correct, the cluster fiducials are accurately calibrated to the standard system, and the cluster parameters are known *a priori* with reasonable accuracy, then any differences between the transformed isochrone and the observed data would indicate problems associated with the synthetic spectra used in the color computations.

Before testing the color–$T_{\rm eff}$ relations against the star cluster observations, it is instructive to first consider how the individual $u'g'r'i'z'$ color indices correlate to changes in the fundamental stellar parameters of $T_{\rm eff}$, log g, and [Fe/H]. In an effort to demonstrate this quantitatively, Table 4.1 lists the derivatives of each color index with respect to the indicated stellar parameters. These values have been computed at two specific locations on an intermediate-metallicity globular cluster's CMD – near the turnoff and on the RGB at the level of the HB. Upon inspection, it is clear that the shorter wavelength indices provide the best chance to discern differences in surface gravity and metallicity at both locations. For instance, the $(u' - g')$ index for giant stars changes by $\sim$ 0.19 mag and $\sim$0.10 mag for every 0.5 dex change in both log g and [Fe/H], respectively. Similarly, the indices involving the u' filter also offer good sensitivity to $T_{\rm eff}$ for globular cluster giants, but an index like $(g' - r')$ is perhaps better for discerning changes in $T_{\rm eff}$ for main sequence and turnoff stars. On the other hand, longer wavelength indices like $(r' - i')$ or $(i' - z')$ are virtually insensitive to changes in log g and [Fe/H] and show only a minor dependence on $T_{\rm eff}$.

Of course, achieving the level of precision in the data necessary to photometrically separate and/or classify stars according to their individual parameters is dependent on the amount of telescope time allocated to the observing project. Observations through u' and z', for instance, normally require the lengthy exposure times due primarily to the decreased quantum efficiency of CCDs and lack of stellar flux in

Table 4.1: Sensitivity of colors to stellar parameters

Turnoff	$[\delta(color)/\delta(T_{\rm eff})]^a$	$[\delta(color)/\delta(\log g)]^b$	$[\delta(color)/\delta([{\rm Fe/H}])]^b$
$(u'-g')$	−0.019	−0.025	−0.026
$(u'-r')$	−0.042	−0.036	−0.029
$(u'-i')$	−0.053	−0.039	−0.032
$(u'-z')$	−0.060	−0.040	−0.034
$(g'-r')$	−0.023	−0.011	−0.003
$(g'-i')$	−0.034	−0.014	−0.006
$(g'-z')$	−0.041	−0.015	−0.008
$(r'-i')$	−0.011	−0.003	−0.003
$(r'-z')$	−0.018	−0.004	−0.005
$(i'-z')$	−0.007	−0.001	−0.002
RGB			
$(u'-g')$	−0.097	−0.192	−0.096
$(u'-r')$	−0.150	−0.222	−0.127
$(u'-i')$	−0.191	−0.233	−0.130
$(u'-z')$	−0.217	−0.236	−0.131
$(g'-r')$	−0.053	−0.030	−0.031
$(g'-i')$	−0.094	−0.041	−0.034
$(g'-z')$	−0.120	−0.044	−0.035
$(r'-i')$	−0.041	−0.011	−0.003
$(r'-z')$	−0.067	−0.014	−0.004
$(i'-z')$	−0.026	−0.003	−0.001

[a] per 100 K

[b] per 0.5 dex

these wavelength regimes. Therefore, an observer must consider which $u'g'r'i'z'$ color index provides the best all-around sensitivity to the stellar parameter of interest while still optimizing the observing time. For the sake of example, consider an observer wanting a color index that provides the best sensitivity to $T_{\rm eff}$ for stars lying near the turnoff of M 13. He or she can make use of the values listed in Table 4.1 to estimate the expected standard error in $T_{\rm eff}$ that may result from a certain photometric error in the observed color index. By employing the MegaCam exposure time calculator (DIET) operated through the CFHT website, and assuming the observer has typical sky conditions at the Mauna Kea site (i.e., photometric conditions with 0.8″ seeing and dark skys), then an answer to the question can be easily achieved by computing the ratio of $\sigma^2(T_{\rm eff})$ resulting from a given index to the value of $\sigma^2(T_{\rm eff})$ computed for the best possible color index at this location in the CMD. These values are: $(u'-g')$, 26.3; $(u'-r')$, 11.9; $(u'-i')$, 9.4; $(u'-z')$, 8.3; $(g'-r')$, 1.4; $(g'-i')$, 1.0; $(g'-z')$, 1.6; $(r'-i')$, 2.6; $(r'-z')$, 2.8; $(i'-z')$, 7.5. These can be interpreted simply as the ratios of the total observing time required to achieve a comparable value of $\sigma(T_{\rm eff})$ for a typical turnoff star in a given pair of filters. Clearly, $(g'-i')$ offers the best sensitivity to changes in $T_{\rm eff}$ per unit time. Interestingly, despite the good sensitivity of $(u'-z')$ to $T_{\rm eff}$, the observer would have to integrate up to 8-9 times longer on the target cluster to achieve a comparable level of precision in $T_{\rm eff}$ for a turnoff star as that obtained from $(g'-i')$. Similarly, exercises such as this can be performed for different types of stars to assist an observer in deciding which set of filters is optimal for the derivation of the other stellar parameters.

4.2.1 Testing the Relations at [Fe/H]<0.0

The testing of the color-$T_{\rm eff}$ relations begins with Population II stars via a comparison of the transformed isochrones to the $u'g'r'i'z'$ data and fiducial sequences derived for the globular clusters M 92, M 13, and M 71. Since good knowledge of

cluster distance, metallicity, and reddening is vital for fitting stellar isochrones to the data, it is important to first mention the various sources of information and methods employed for the determination of these parameters. Initially, the analysis of the globular cluster data favors the [Fe/H] values on the metallicity scale of Zinn & West (1984; hereafter ZW84) and the reddenings derived from the Schlegel, Finkbeiner, & Davis (1998) dust maps.[4] The preference of the ZW84 metallicity scale over that derived by Carretta & Gratton (1997) using high-resolution spectroscopy is based on the fact that the latter predict [Fe/H] values that are ~ 0.3 dex higher at intermediate metallicities ($-2.0 \lesssim$ [Fe/H] $\lesssim -1.0$) than the former, and VandenBerg (2005) has shown that the metallicity estimates inferred from model isochrone fits to the clusters M 3 and M 5 are in better agreement with those of ZW84. Estimates of the cluster distance moduli are primarily based on fitting theoretical zero-age horizontal branch (ZAHB) to the lower envelope of stars defining clusters horizontal branch (HB). According to the recent works of De Santis & Cassisi (1999) and Cacciari, Corwin, & Carney (2005), the luminosity of RR Lyrae stars in globular clusters, as derived from analyses of their pulsational properties, are close to those predicted by the ZAHB models employed here. Once the distance and reddening have been constrained for a particular cluster, the age determination is based on the isochrone fits in the vicinity of the cluster turnoff (TO) point and sub-giant branch (SGB) region. Generally, small horizontal shifts in color are also required in order to achieve a good match to the observed main sequence (MS), thereby compensating for inaccurate photometric zero-points, incorrect reddening, or shortcomings in the color-$T_{\rm eff}$ relations.

Figures 4.2-4.4 present a variety of $u'g'r'i'z'$ CMDs for the clusters considered here overplotted with the appropriate isochrones. Focusing on the CMDs for M 92 in Figure 4.2 as an example, each panel plots the indicated dereddened color versus its absolute r' magnitude for direct comparison to the isochrones and ZAHB models

[4]The resulting $E(B-V)$ values from these maps are then transformed to their equivalents in the $u'g'r'i'z'$ system using the relations of Rider et al. (2004): $A_{u'} = 5.155/E(B-V)$, $A_{g'} = 3.793/E(B-V)$, $A_{r'} = 2.751/E(B-V)$, $A_{i'} = 2.086/E(B-V)$, and $A_{z'} = 1.479/E(B-V)$

denoted by solid lines. The derived absolute distance modulus and adopted [Fe/H] values (to within 0.1 dex on the ZW84 scale) are listed in the left-hand panel along with the age that provides the best match of the isochrone to the cluster's TO point. Note that the isochrones employed for the fitting come from Bergbusch & VandenBerg (2001) and assume $[\alpha/Fe] = +0.3$. These isochrones do not include the effects of He diffusion, which would decrease the derived ages at a given TO luminosity by $\sim 10-15\%$ (see VandenBerg et al. 2002) while not otherwise changing the quality of the fit. In addition, each panel provides the sizes of both the reddening corrections applied to the data $[E(color)]$ and the horizontal color shifts that have been applied to the isochrone $[\delta(color)]$ in order to improve the fits to the cluster main sequences. The individual cluster stars are indicated by light-grey dots with their corresponding fiducial sequences spanning the MS, SGB, and RGB locus overplotted as dotted lines.

Clearly, the adopted isochrones provide superb and consistent matches to the derived fiducial sequences for all four globular clusters in the vicinity of the TO and upper-MS (i.e. $4 \lesssim M_{r'} \lesssim 7$). Furthermore, with the exception of the $[(u'-g'), M_{r'}]$ diagrams for M 92 and M 13 where the transformation of the observed u^* photometry from CFHT to the standard u' is suspect (see Section 3.1.2), the stars defining the HB locus are also fit quite well by the ZAHB models. These results are perhaps not that surprising since both Paper I and Paper II found that theoretical color-$T_{\rm eff}$ relations for the $BV(RI)_c$ and *uvby* systems computed from synthetic spectra provide comparably good matches to the same parts of the observed $B-V$, $V-I$, and $b-y$ CMDs for some of these same clusters.

A clear discrepancy begins to appear, however, for the brighter and cooler cluster members with the isochrone lying consistently redward of the RGB loci regardless of which color index is employed. If this is a result of problems with the synthetic spectra, then it is quite surprising that the predicted indices for dwarf MS stars lying at the same color do not exhibit a similar tendency to the red. Moreover, the comparisons shown in Figure 4.1 reveal that the filter response functions employed for

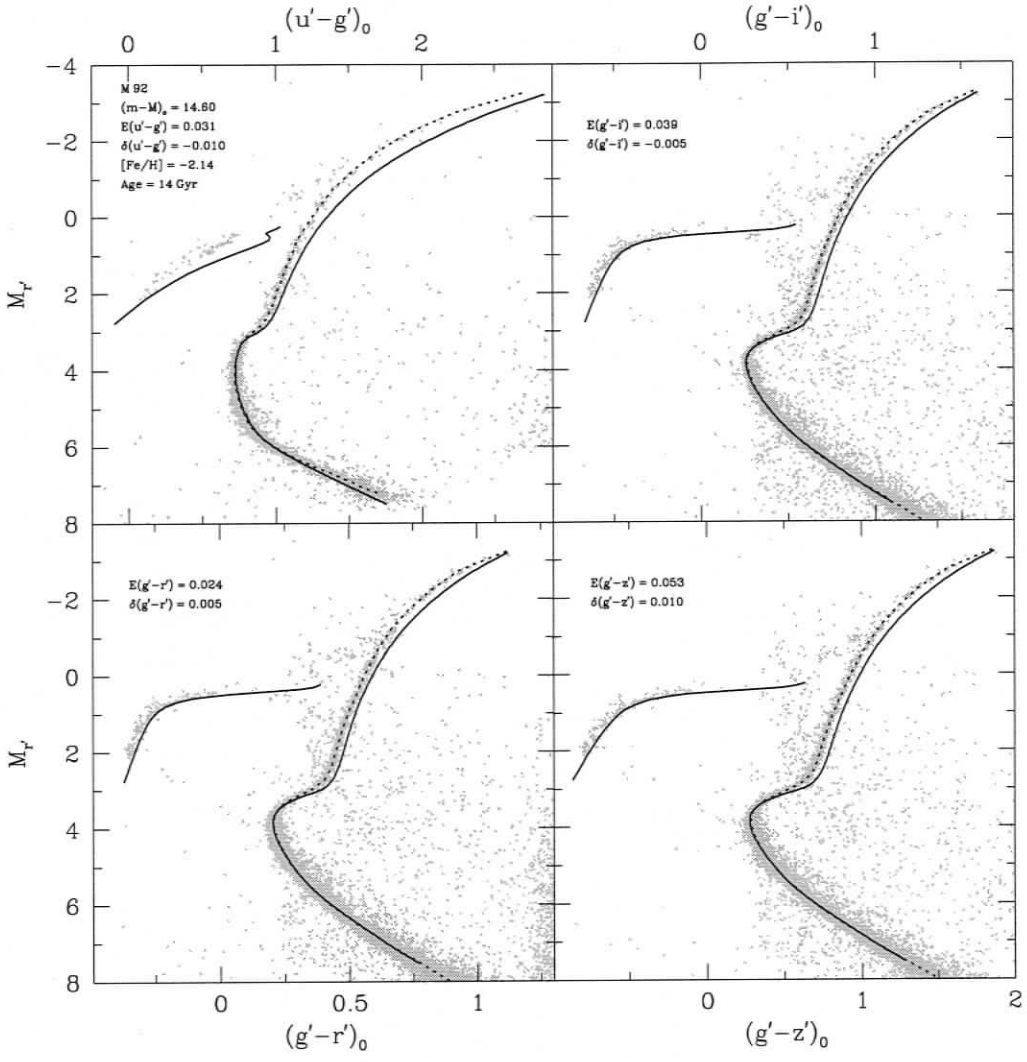

Figure 4.2: Fits of isochrones and ZAHB models (solid lines) corresponding to the indicated metallicity and age to the various $u'g'r'i'z'$ CMDs for M 92. Small grey dots denote individual cluster stars with dotted lines providing the fiducial sequences derived for the RGB, SGB, and MS loci.

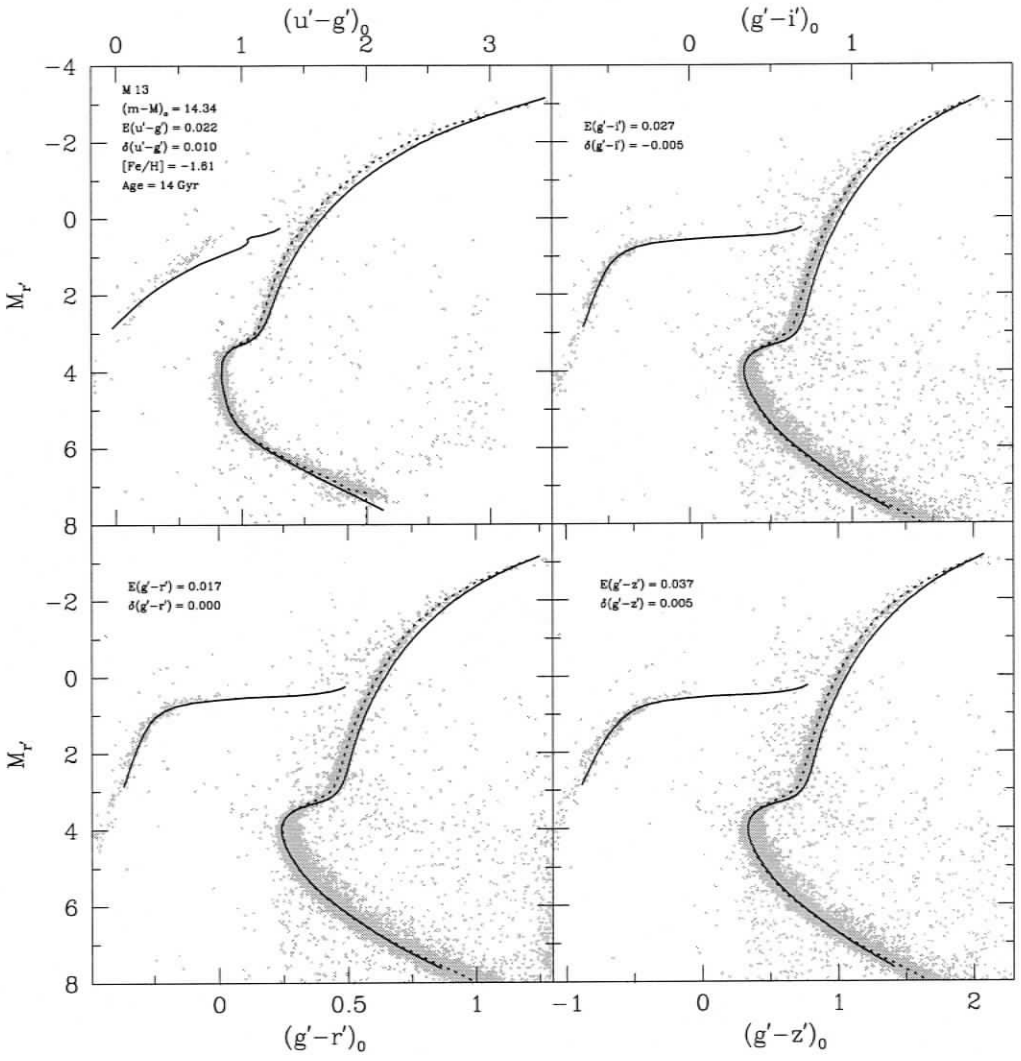

Figure 4.3: Same as Figure 4.3, but for M 13

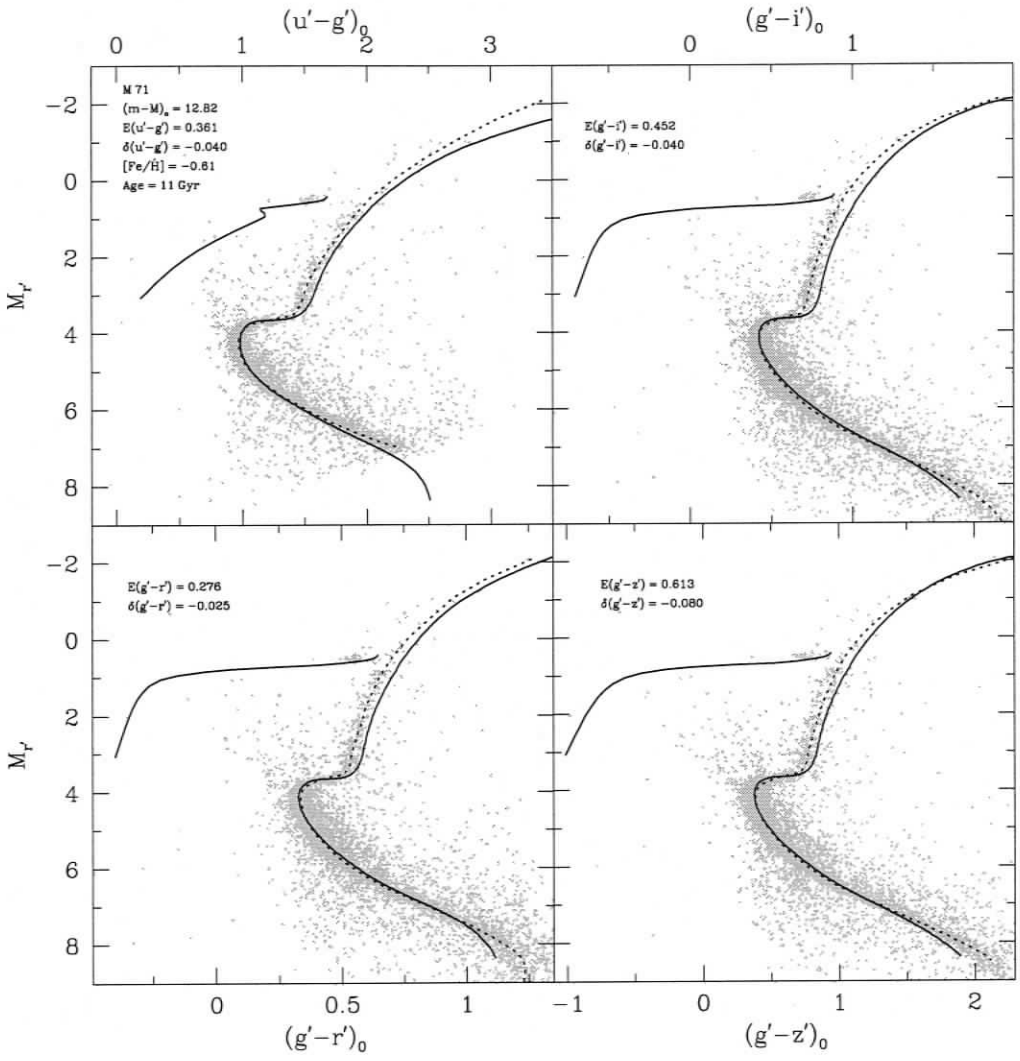

Figure 4.4: Same as Figure 4.2, but for M 71

the synthetic color computations can reliably match the $u'g'r'i'z'$ filters used to define the standard system (at least for Population I dwarf and giant stars); this would tend to rule out problems with the adopted filter functions as the cause. The fact that these redward offsets in the RGBs of the isochrones are similar between the different colors and different clusters strengthens the support for the accuracy of the theoretical color–$T_{\rm eff}$ relations for metal-poor stars in that they are providing consistent matches of the isochrones to the data regardless of which color index is employed. However, the synthetic spectra employed for the color computations may have been derived using the wrong values for the convective mixing length and/or micro-turbulent velocity, and perhaps even an incorrect abundance scale, but without grids of model Kurucz spectra computed using different values of these parameters for comparative purposes, it is difficult to explain the cause of these discrepancies on the basis of the theoretical colors themselves.

Alternatively, the model temperature scales of the isochrones themselves may be in error. To account for the offsets in the cool giants stars seen in Figures 4.2-4.4, the temperatures along the RGB would have to increase by $\sim 50 - 200$ K, depending on metallicity, to provide an acceptable match the the entire RGB locus. However, VandenBerg et al. (2000) have shown that the predicted giant branches for these clusters on the (M_{bol}, log $T_{\rm eff}$)-plane agree with those derived by Frogel, Persson, & Cohen (1981) from $V-K$ photometry when similar distance moduli and [Fe/H] values are assumed. Although their derived $T_{\rm eff}$ estimates are uncertain by at least $\pm$100K, the fact that the RGB loci of isochrones agree to well within these uncertainties provides considerable support for the temperature scale along the isochrones' RGBs.

In an effort to provide some additional insight into the problems associated with the RGB, the top panels in Figures 4.5-4.7 provide CMDs highlighting the upper-MS, TO, and lower-RGB regions for M 92, M 13, and M 71 using the colors observed in three different photometric systems (i.e., the $u'g'r'i'z'$, $BV(RI)_c$, and *uvby* systems) plotted against absolute V-band magnitudes. For each cluster the empirically-

constrained color–$T_{\rm eff}$ relations and bolometric corrections to the V-band reported in Paper I and Paper II have been used to transform the same isochrones (solid lines) used in the previous comparisons to the $[B-V,\ M_V]$ and $[v-y,\ M_V]$ CMDs. The BV cluster data come from Stetson (private communication) while the *uvby* photometry is from Grundahl (1998, 2000, 2002). Note that each CMD is plotted against the absolute V-band magnitude derived using the distance moduli indicated in Figures 4.2-4.4 in order to reveal any problems that might be associated with the colors themselves and not the computed bolometric corrections in r'. Clearly, the same discrepancy that is present in the $u'g'r'i'z'$ CMDs is also seen when the isochrones are translated to the other colors in different photometric systems.

This is not the entire story, however. The bottom panels in Figures 4.5-4.7 show the fits obtained if the assumed metallicities for these clusters are decreased by $\lesssim 0.2$ dex. Recall that the metallicity scale adopted for the comparisons above is that of ZW84, but their [Fe/H] estimates have an uncertainty of at least 0.1-0.2 dex. Therefore, assuming slightly lower metallicities for these clusters is quite reasonable. In fact, Kraft & Ivans (2003) have recently derived a new globular cluster metallicity scale based on analysis of Fe II lines, and their quoted [Fe/H] values for M 92 and M 71 are consistent with the slightly more metal-poor values adopted here ([Fe/H]=-2.38 and -0.81, respectively). Indeed, employing more metal-poor isochrones results in improved fits to the RGBs, although this is due to the fact that a slightly older age is required to provide a good fit to the cluster TO points. Moreover, the fits to the SGBs seem to be also improved by using an older age isochrone. While some slight offsets are still noticeable in the regions of the SGB and lower-RGB, these can largely be removed by adopting slightly smaller distance moduli or perhaps even lower metallicities. Based on these findings, there seems to be no strong evidence that contradicts the reliability of the $u'g'r'i'z'$ color-$T_{\rm eff}$ relations for metal-poor stars, or even the color–$T_{\rm eff}$ relations presented in Papers I and II for that matter. To be sure, one can doubt the accuracy of the adopted distances, reddenings, and metallicities, but it

cannot be denied that the choices for these parameters are within the uncertainties of current estimates. Given the evidence shown above that consistent fits are achieved regardless of which data set and color–$T_{\rm eff}$ relations are employed, however, would seem to indicate that theoretical colors and bolometric corrections that are computed from synthetic spectra for metal-poor stars are reasonably accurate.

4.2.2 Testing the Relations at [Fe/H]$\gtrsim 0.0$

Tests of the color–$T_{\rm eff}$ relations for more metal-rich stars are presented in Figures 4.8 and 4.9, which show the fits of the VandenBerg, Bergbusch, & Dowler (2005) isochrones to the $u'g'r'i'z'$ photometry for the open clusters M 67 and NGC 6791. Note that the comparisons presented here are limited to only $g'r'i'$ photometry for M 67 and $g'r'i'z'$ photometry of NGC 6791. In both figures the indicated distance moduli, metallicities, reddenings, and ages are *exactly* the same as the values favored in Papers I and II from their analysis of these two clusters in the $BV(RI)_C$ and *uvby* systems (see Paper I and Paper II for a justification of these values). These parameters have been adopted here to ensure complete consistency in the interpretations of the $u'g'r'i'z'$ CMDs given in Figures 4.8 and 4.9.

The adopted isochrones clearly provide acceptable matches to both clusters in the vicinity of the RGB, SGB, TO, and upper-MS, which would indicate the computed colors for stars in these regimes are reasonably accurate. This agreement soon begins to break down towards cooler $T_{\rm eff}$'s, however. Specifically, the isochrones predict colors for lower-MS stars that are systematically blueward of the observed data. Similar discrepancies in the $BV(RI)$ and *uvby* colors computed from Kurucz synthetic spectra for cool dwarfs have been noted before in Papers I and II. To reassure the reader that these discrepancies are not due to problems with the calibrated photometry, Figure 4.10 presents various color-color diagrams for the S02 $u'g'r'i'z'$ standard star with $B-V$ index plotted as the abscissa. The sample of standards is limited to those

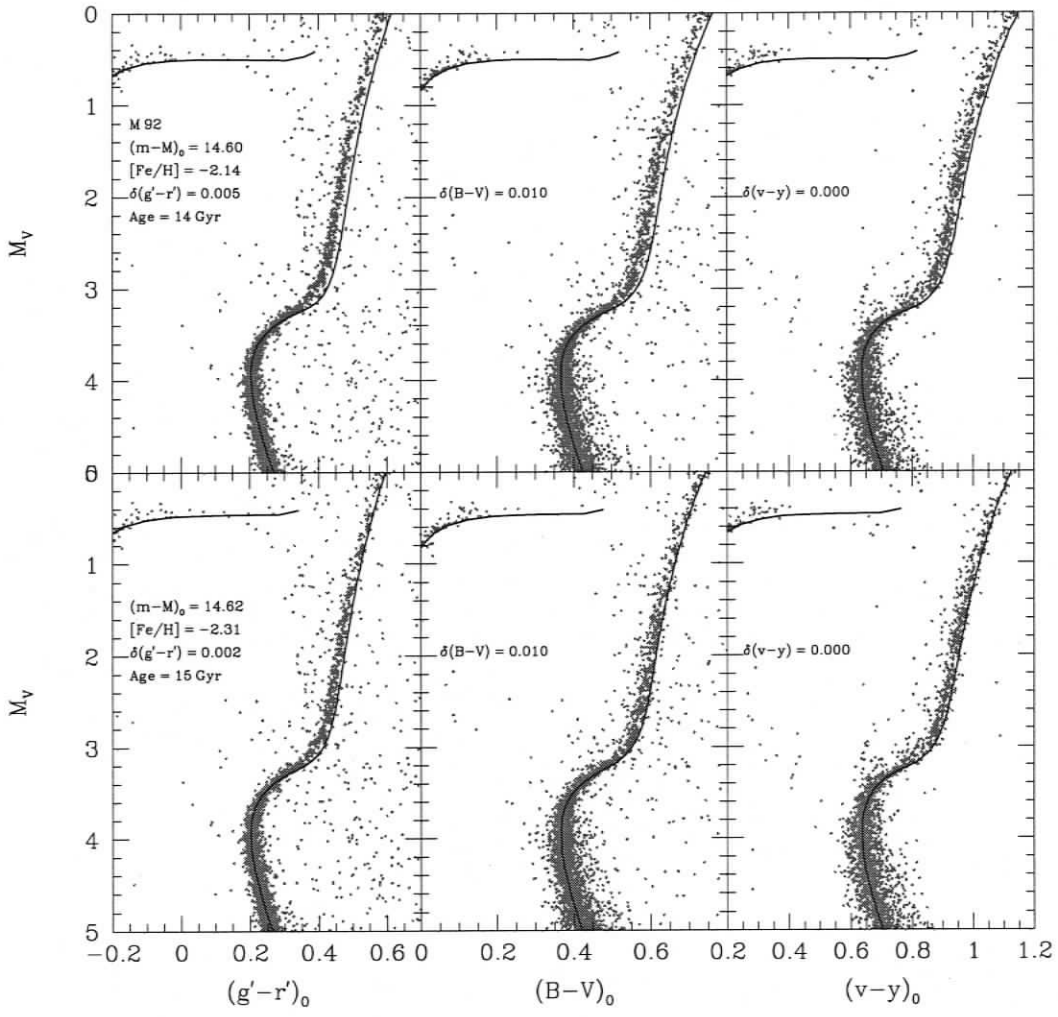

Figure 4.5: Isochrone and ZAHB fits to various CMDs involving $u'g'r'i'z'$, $BV(RI)_c$, and *uvby* indices versus M_V for M 92. The photometry has been corrected for reddening using the values of Schlegel et al. (1998). The transformation of the stellar models to $B-V$ and $v-y$ CMDs are accomplished using the color–$T_{\rm eff}$ relations reported in Paper I and Paper II, respectively. The top row of panels employ the same isochrone and ZAHB that were used in the initial fits to the M 92 $u'g'r'i'z'$ CMDs shown in Figure 4.2 while the CMDs in the bottom row show the results obtained if the adopted metallicity is decreased by $\sim 0.1-0.2$ dex and assumed age is increased by 1 Gyr.

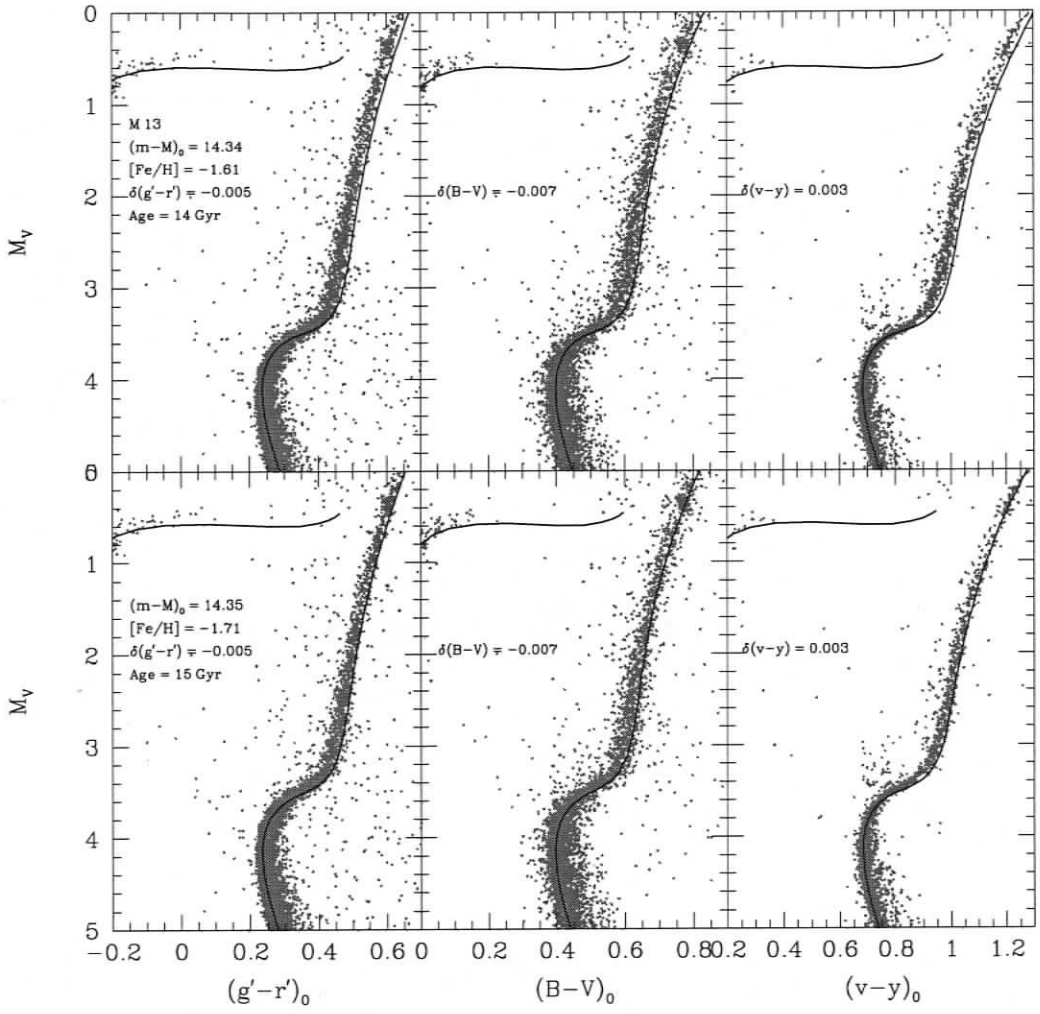

Figure 4.6: Same as Figure 4.5, but for M 13.

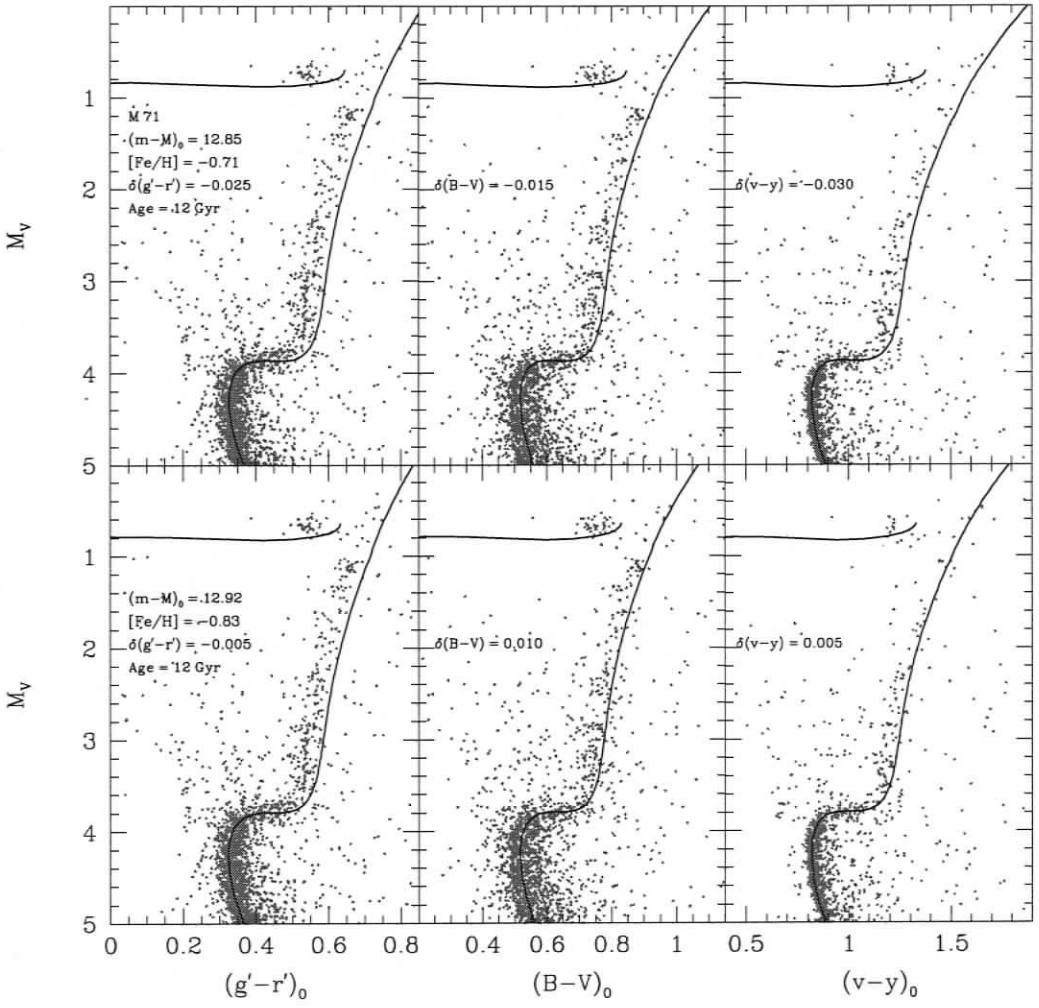

Figure 4.7: Same as Figure 4.5, but for M 71.

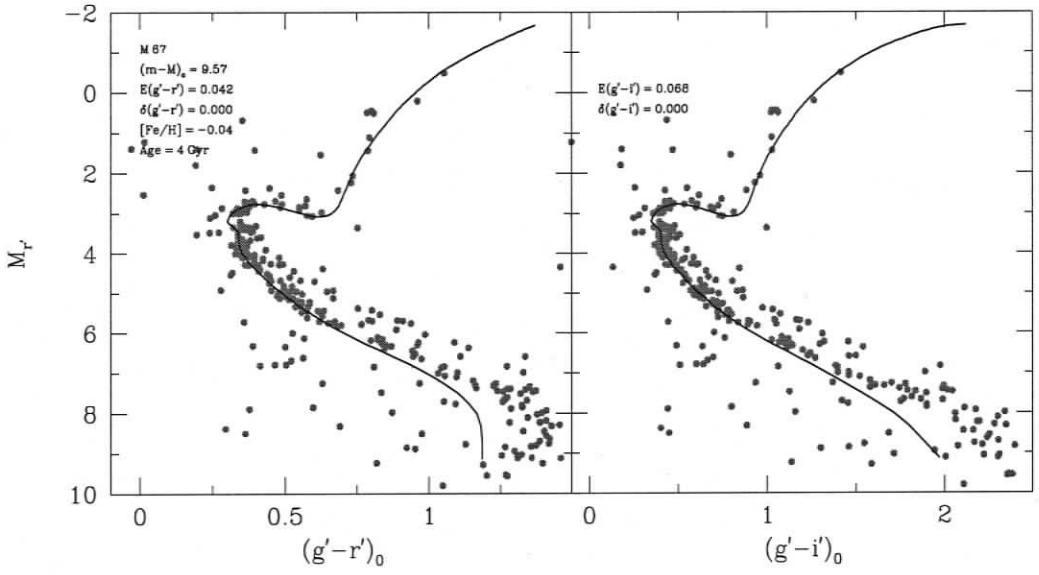

Figure 4.8: Same as Figure 4.2, but for the open cluster M 67

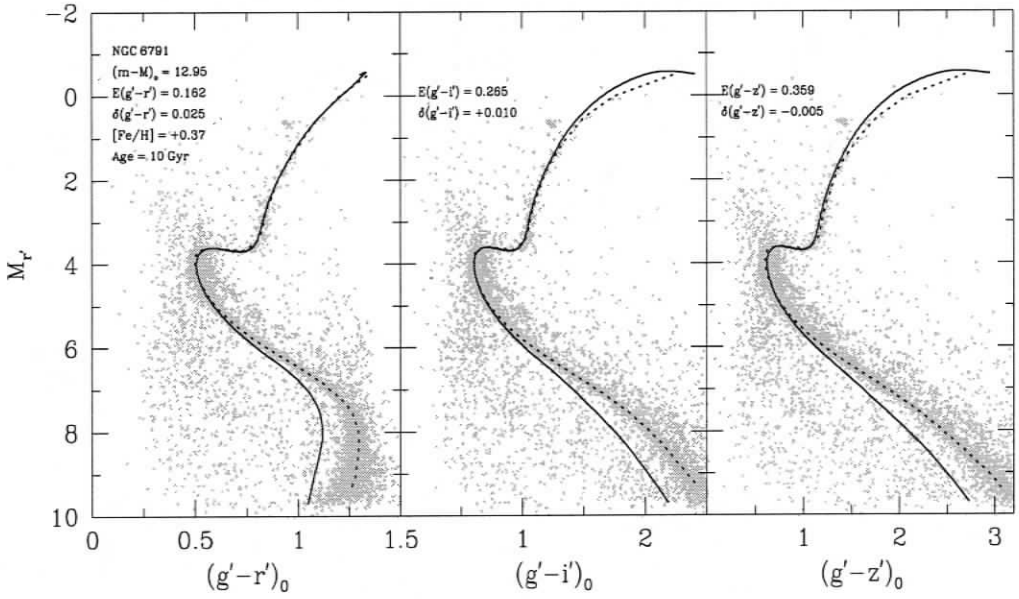

Figure 4.9: Same as Figure 4.2, but for the open cluster NGC 6791

stars that could be identified as Population I dwarfs based either on their published spectral types or positions in the color-color diagrams. As mentioned earlier, the $B-V$ photometry for these stars comes primarily from the works of Landolt and the indicated ZAMS model (solid line) has been transformed to the $B-V$ colors using the $BV(RI)_c$ transformations derived in Paper I for comparison. Clearly, the agreement here is quite good for stars with $(B-V) \lesssim 1.0$ (corresponding to $T_{\rm eff} \gtrsim 5000\,{\rm K}$) in all panels, but the ZAMS begins to mirror the same blueward deviations seen in the $g'-i'$ and $g'-z'$ colors for cooler stars in the CMDs shown above. Note that due to the lack of u' observations for the two open clusters considered here, the sample of S02 standards provides the only means to test the reliability of the $u'-g'$ colors at [Fe/H] ~ 0.0. In this respect, the correspondence noted in the top left-hand panel of Figure 4.10 between the ZAMS model and observed data for the dwarf standard stars lends considerable support for the derived $u'-g'$ colors, even beyond $B-V \sim 1.0$ where the other colors begin to show discrepancies.

Again, the question arises of whether or not the model temperature scales of the isochrones themselves could be contributing to the mismatch at the faint end. In this regard, both Paper I and Paper II have shown that when the colors for the $BV(RI)_c$ and *uvby* systems are constrained to match observational data for Population I stars, the resulting *predicted* color–$T_{\rm eff}$ relations for solar-metallicity dwarfs match those determined empirically by a number of different studies. In addition, similar consistency between theory and observations is found when comparing the predicted RGB locus from the 4 Gyr, [Fe/H]$\approx$0.0 isochrone to the ($T_{\rm eff}$, M_{bol}) predictions for giant stars in M 67 as derived from $V-K$ photometry (see Fig. 27 in Paper I). Therefore, confidence in the isochrones is quite high and it would seem that the theoretical color–$T_{\rm eff}$ relations and/or r' bolometric corrections are the cause of the problem.

Since the color transformations computed from Kurucz spectra do not appear to match the observed data for real stars towards cooler $T_{\rm eff}$'s, it is instructive to perform a comparison between his synthetic spectra and the observed spectrophotometry from

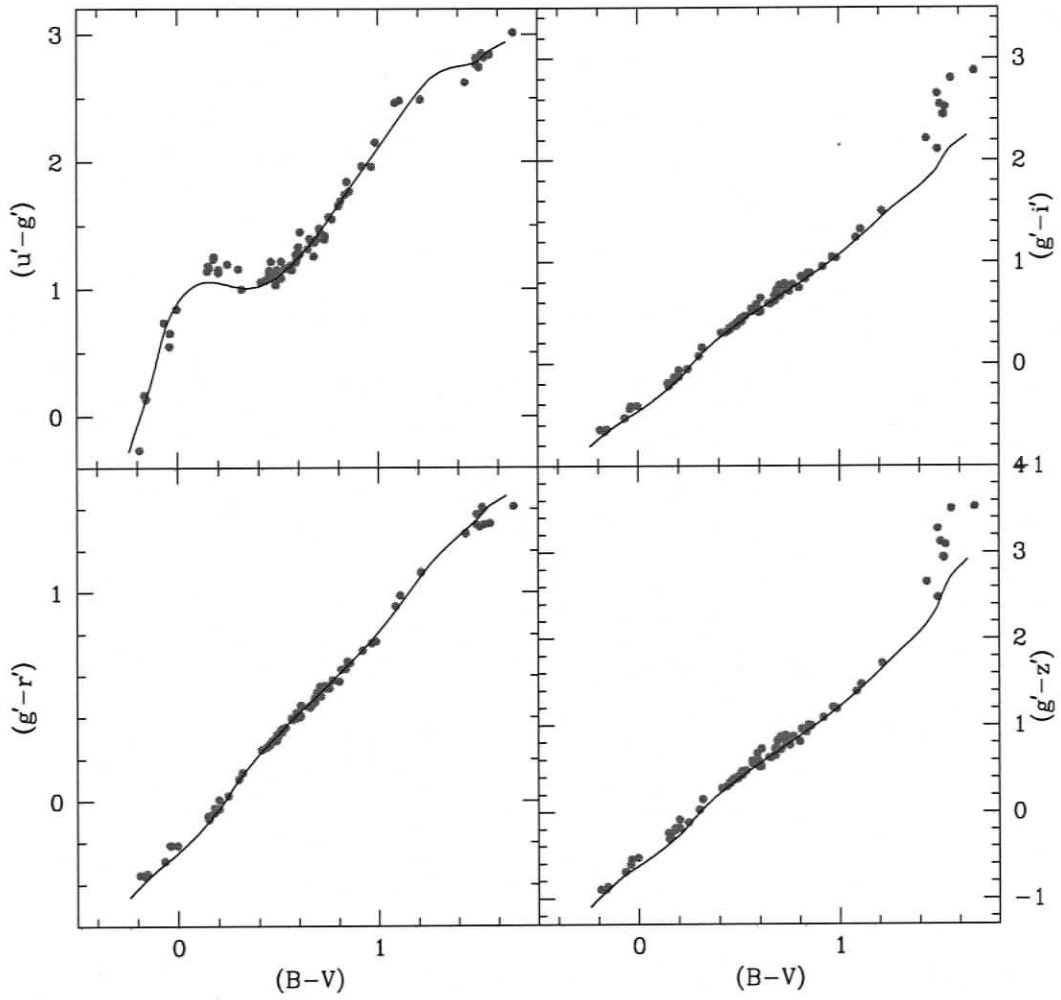

Figure 4.10: Fits of a ZAMS model having [Fe/H] = 0.0 to the $u'g'r'i'z'$ photometry for the S02 sample of standard stars. Note the same blueward deviations of the model isochrone from the $g' - i'$, and $g' - z'$ data for $B - V \gtrsim 1.0$ that were present in the CMDs for M 67 and NGC 6791 are also obvious here.

the GS83 atlas for a representative sample of early-, mid-, and late-type dwarf stars. Such a comparison is shown in Figure 4.11 where the observed flux distributions for stars approximating A0, G2, and M0 dwarfs (solid lines) are overplotted with Kurucz synthetic spectra computed for the indicated stellar parameters (dotted lines) that provide the best fits to the observed spectra. Note that both spectra are plotted on an arbitrary scale to facilitate these comparisons. While the synthetic and observed spectra for the A0 and G2 dwarfs plotted in the top two panels are fit reasonably well by the Kurucz models over the entire wavelength range, the deviations for the cooler M0 dwarf are quite substantial, especially towards longer wavelengths. The strong absorption bands seen between 6000Å and 9000Å correspond to the TiO molecule. It would appear that Kurucz predicts much stronger TiO absorption than is actually observed. To be sure that the GS83 template spectrum for an M0 dwarf employed here for comparisons is not metal poor (no [Fe/H] information is available for stars in the GS83 atlas), plots similar to those in Figure 4.11 have been constructed for other cool GS dwarf stars ranging from K5 to M2 to reveal that the stronger TiO absorption bands are a ubiquitous feature of the Kurucz spectra for stars with solar metallicities.

To demonstrate the quality of isochrone fits to the $BV(RI)_c$ and *uvby* data for M 67 and NGC 6791 that were obtained in Paper I and II, Figures 4.12 and 4.13 provide their $B-V$ and $v-y$ CMDs together with the fits on the $g'-r'$ plane. The BV photometry for M 67 comes from Montgomery et al (1993) while that of NGC 6791 is from Stetson et al. (2003). The *uvby* data for both open clusters have been kindly provided by F. Grundahl (private communication). Again, the CMDs involving colors from different photometric systems are all plotted against M_V to prevent any misinterpretation of the cluster CMDs based on incorrectly calculated $BC_{r'}$ values. Given the fact that the interpretation of the data on the $B-V$ and $v-y$ CMDs is precisely the same for both clusters lends considerable support to the color-$T_{\rm eff}$ relations that have been presented for the $BV(RI)_c$ and *uvby* systems, even if different methods

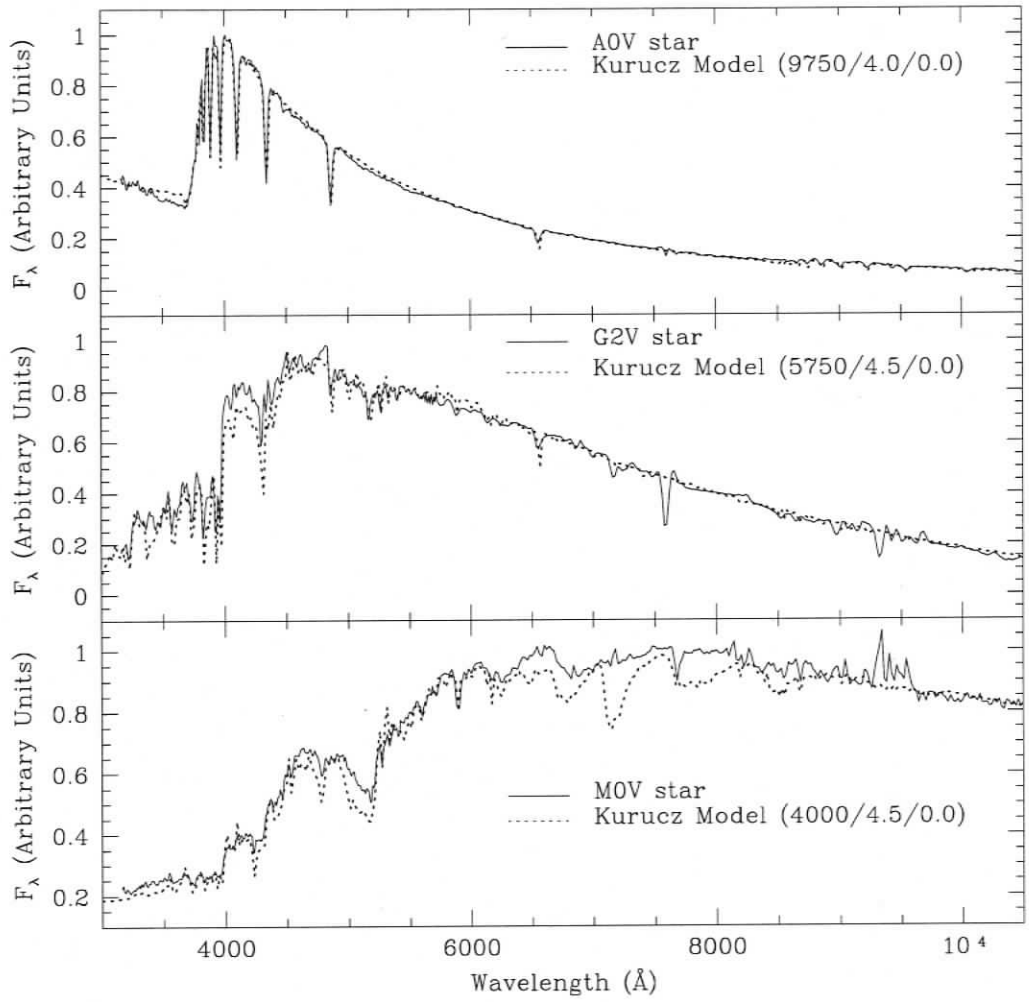

Figure 4.11: Comparisons of the observed spectra from the GS83 spectrophotometric atlas (solid lines) to Kurucz synthetic spectra computed for the indicated ($T_{\rm eff}$, log g, [Fe/H]) values (dotted lines) for dwarf stars having spectral types A0, G2, and M0. Note the significant mismatch in the bottom panel for the late-type dwarf in the wavelength regimes where absorption due to TiO is overpredicted by the Kurucz models.

were used to empirically correct the colors. Briefly, corrections to the $BV(RI)_c$ colors in Paper I at solar metallicities were largely accomplished by systematically shifting the colors for cool stars redwards until they matched the observed MS locus of M 67 in the $B - V$ and $V - I$ CMDs. When the colors are corrected in this way, the resulting $(B - V)$–$T_{\rm eff}$ relation is shown to be in good agreement with that derived empirically by Sekiguchi & Fukugita (2000) from a careful analysis of solar-metallicity dwarf stars. Moreover, they also provide exceptional fits to the $B - V$ CMDs for the Hyades and Pleiades. Corrections to the *uvby* transformations in Paper II, on the other hand, were based entirely on a sample of field stars that have well-determined $T_{\rm eff}$ values derived using the infrared flux method (IRFM) and in no way relied on star cluster CMDs to perform these corrections at [Fe/H] = 0.0. Likewise, the resultant transformations provided a consistent match of the isochrones to the CMDs of M 67 and the Hyades, as well as matched empirically-derived color-$T_{\rm eff}$ relations for solar metallicity dwarfs. Indeed, Figure 4.14 shows that when the field dwarf and giant stars having accurate IRFM temperatures, as well as spectroscopically determined log g and [Fe/H] values, are inserted in the color tables for the $BV(RI)_c$ and *uvby* systems, the computed $B - V$ and $v - y$ indices are in good agreement with their observed counterparts. This evidence, along with the comparison between observed and computed spectra shown in Figure 4.11, thus justifies the need to apply empirical corrections to the synthetic $u'g'r'i'z'$ colors to bring them into better agreement with the observed data.

4.2.3 Testing the r' Bolometric Corrections

In some of the comparisons presented so far, the transformation from computed bolometric magnitudes for the stellar evolutionary models to absolute r' magnitudes has obviously required the use of the bolometric corrections predicted by the synthetic spectra. Given the discrepancies seen above in the $u'g'r'i'z'$ color–$T_{\rm eff}$ relations for

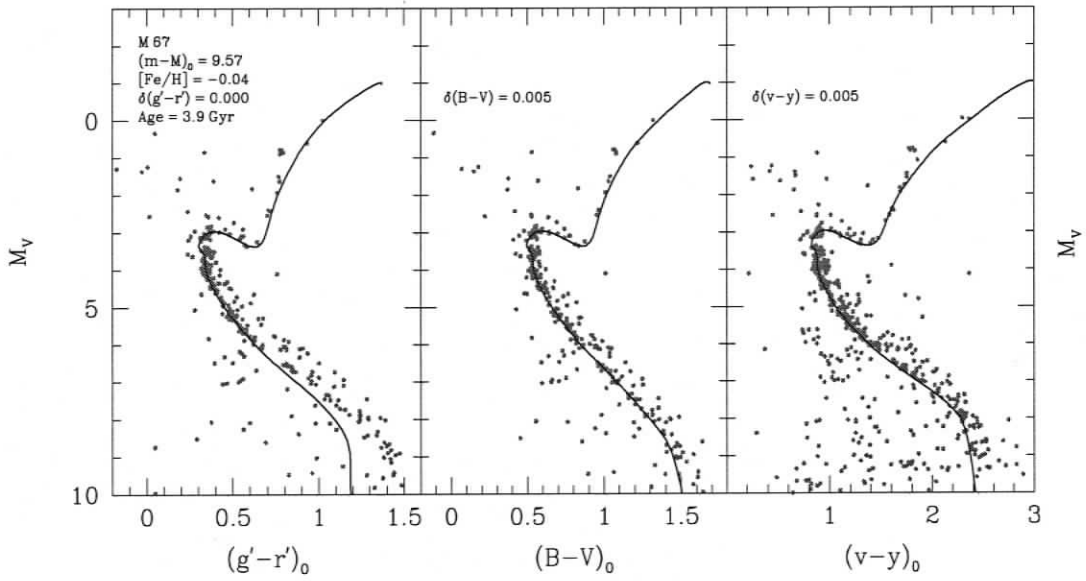

Figure 4.12: Same as Figure 4.5, but for the open cluster M 67.

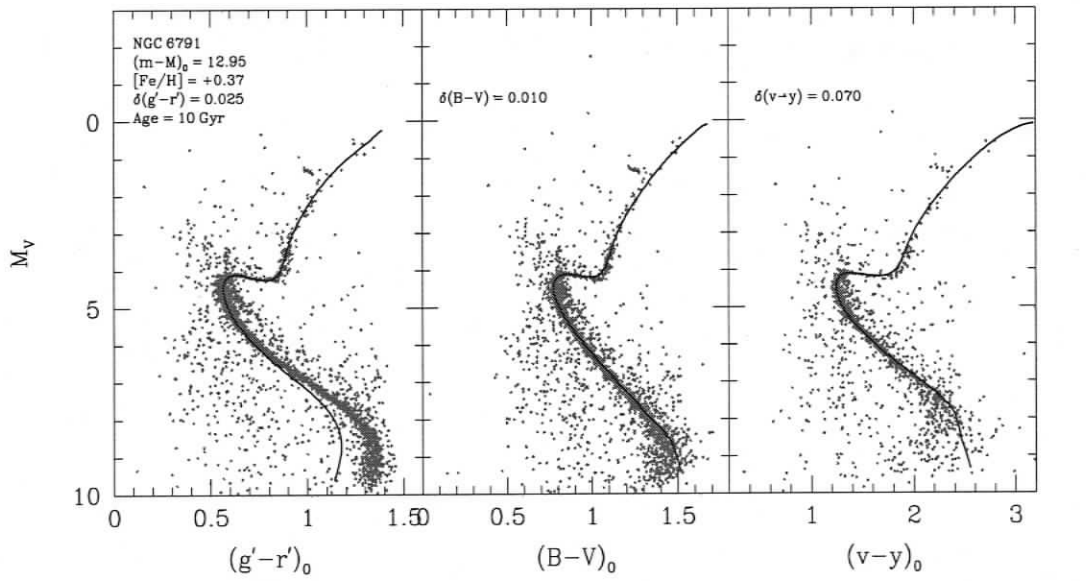

Figure 4.13: Same as Figure 4.5, but for the open cluster NGC 6791.

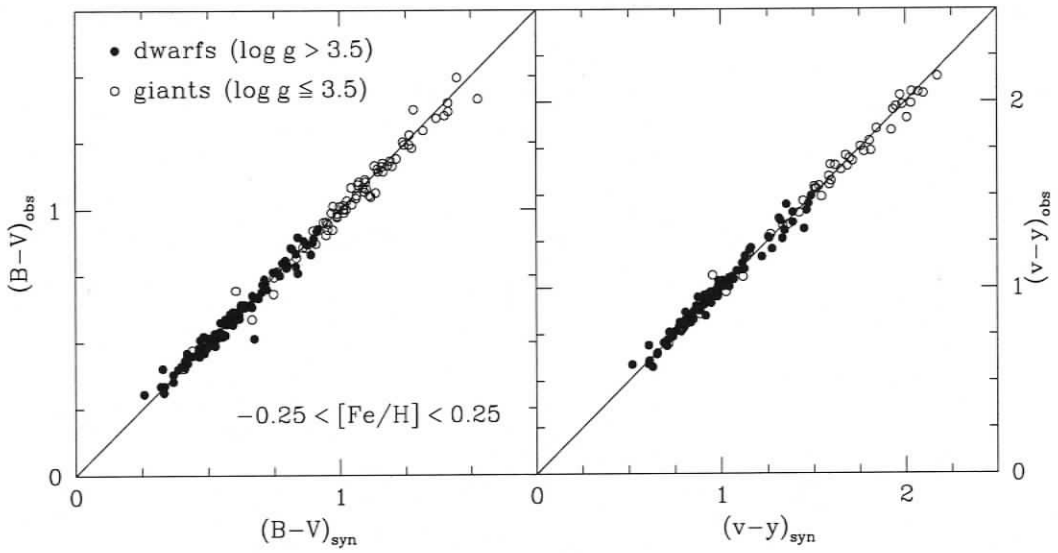

Figure 4.14: Comparisons between the observed and computed $B-V$ and $v-y$ photometry for solar-metallicity dwarf and giant stars having accurate $T_{\rm eff}$'s derived using the IRFM. The synthetic colors are derived by interpolation in the $B-V$ and $v-y$ color–$T_{\rm eff}$ relations from Paper I and Paper II using the $T_{\rm eff}$, log g, and [Fe/H] estimates provided by Alonso et al. (1996, 1999).

Population I stars, it is reasonable to assume that the synthetic spectra are not reliable in producing either colors or r' bolometric corrections that match those of cool dwarf stars with $T_{\rm eff} \lesssim 5500K$ and [Fe/H]$\gtrsim$0.0. Indeed, some of this discrepancy seen in the $u'g'r'i'z'$ CMDs for the open clusters can be attributed to problems in the computed $BC_{r'}$ values. To demonstrate this, Figure 4.15 presents the CMDs for some of the same clusters considered above, but this time the colors are expressed as $(V - r')$ versus M_V. Assuming the BC$_V$ predictions from Paper I are correct for metal-poor stars, then it would appear that the $BC_{r'}$ values derived for metal-poor dwarfs and giants are likewise valid based on the good agreement with the observed globular cluster data. However, a notable discrepancy in the $V - r'$ isochrones is apparent when comparing the isochrones to the observed data for the open clusters. This deviation can only be attributed to incorrect $BC_{r'}$ values since the BC_V values for low-mass stars have been well-constrained below $M_V \sim 5$ against the observed mass-M_V data for local M dwarfs (see Fig. 16 in Paper I). Therefore, in order for the isochrones to provide consistent matches to low-mass stars at the metal-rich end, it would appear that corrections to both the $u'g'r'i'z'$ colors and $BC_{r'}$ values are required.

4.3 Summary

The theoretical color–$T_{\rm eff}$ relations and bolometric corrections for the $u'g'r'i'z'$ system that have been derived from Kurucz synthetic spectra have been shown to be quite accurate in matching the observed photometry for metal-poor dwarf and giant stars (i.e., [Fe/H]$<$ 0). Notably, the transformations not only provide consistent fits of appropriate isochrones among the various globular cluster CMDs involving the different $u'g'r'i'z'$ color indices, but also agree with the interpretations resulting from similar fits employing $BV(RI)_c$ and *uvby* indices if one assumes a metallicity scale that is $\sim 0.1 - 0.2$ dex more metal poor than that of ZW84, such as the Kraft & Ivans

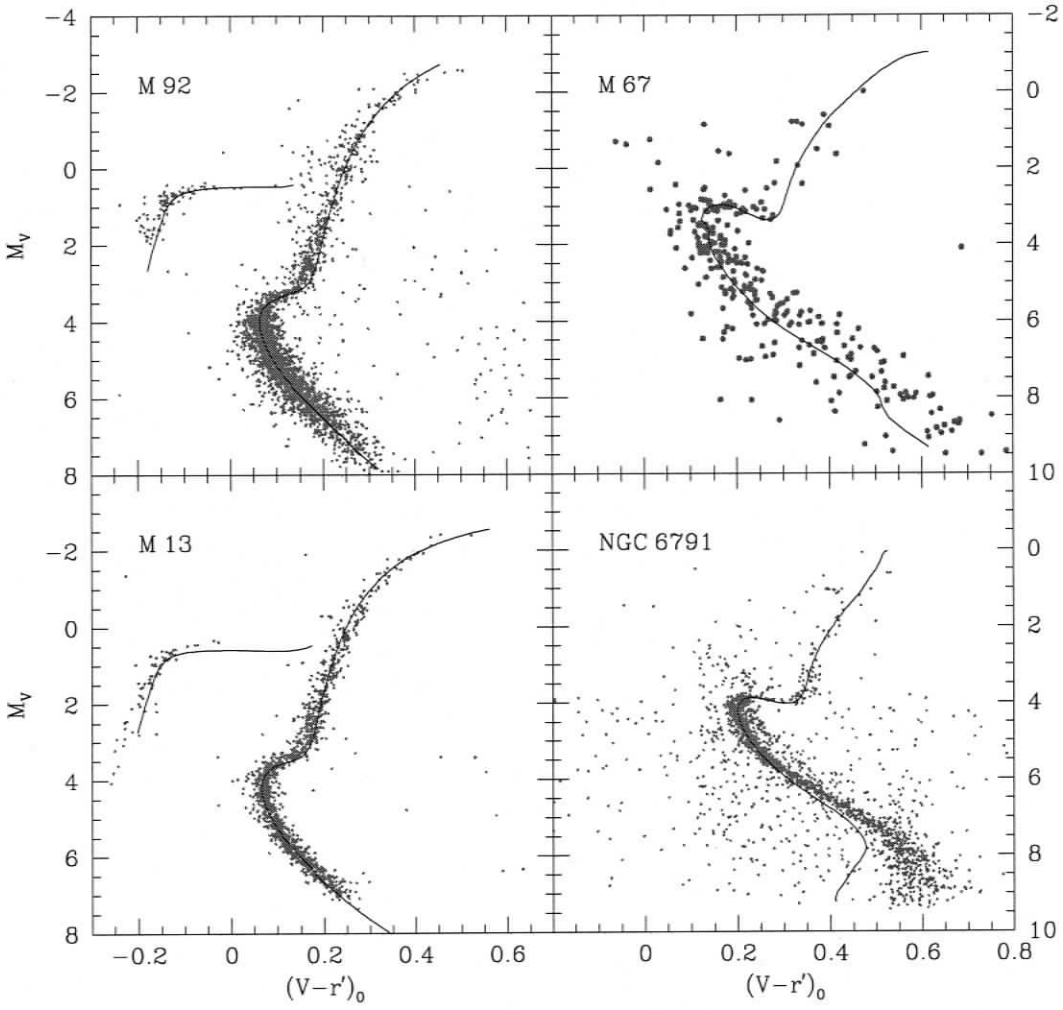

Figure 4.15: $(V - r',\ M_V)$ CMDs for the globular and open clusters overplotted with the isochrones favored in the analysis above. The plots are meant to show that when the BC_V values provided by Paper I are used in conjunction with the $BC_{r'}$ predictions from Kurucz synthetic spectra, the resulting fits to the cluster CMDs are in good agreement except at the fainter end of the MS for the open clusters M 67 and NGC 6791.

(2003) scale based on analysis of Fe II lines. At solar and super-solar metallicities, however, the colors deviate systematically to the blue compared to the observed M 67 and NGC 6791 $u'g'r'i'z'$ CMDs for stars lying on the lower-MS. These discrepancies cannot be attributed to errors in the filter transmission functions used in the synthetic color computations, the observed photometry, or miscalibrated temperature scales of the isochrones themselves. In the end, the most likely interpretation may be related to the observations that Kurucz spectra for cool, high-gravity models predict stronger molecular absorption due to TiO than what in actually observed in late-type dwarfs. Indeed, this analysis could have relied upon a different grid of stellar spectral models (e.g., MARCS/SSG, NextGen, etc.), and may have resulted in better fits at the metal-rich end, but the shortcomings of contemporary 1-D model atmospheres and spectral synthesis models for cooler stars cannot be denied (see Paper I). Therefore, the methods employed by Paper I and II to compensate for these shortcomings and provide a set of accurate, empirically-constrained color–$T_{\rm eff}$ relations for the $BV(RI)_c$ and *uvby* systems should be applicable to the $u'g'r'i'z'$ system as well.

In this respect, if small redward shifts are applied to the synthetic colors to match observed main sequence of M 67 in the various $u'g'r'i'z'$ CMDs (see Figure 4.16), as was done in Paper I to correct the $BV(RI)_c$ colors at [Fe/H] = 0, the resulting ZAMS model for solar-metallicity stars also provides improved matches to the color-color diagrams of the $u'g'r'i'z'$ standard stars in Figure 4.17, particularly in $(g' - i')$. Unfortunately, with the database of observed $u'g'r'i'z'$ photometry for stars that have well-known physical parameters (particularly IRFM-determined $T_{\rm eff}$'s) lacking, the type of analysis performed in Paper II for the *uvby* system cannot be applied here at the present time. While the observed fiducial sequences for globular and open clusters have provided a valuable set of calibrators for the transformation of stellar models to the $u'g'r'i'z'$ bandpasses, it would undoubtedly be useful to have a large database of stars with both well-determined physical parameters and observed $u'g'r'i'z'$ photometry to further constrain the accuracy of the theoretical color–$T_{\rm eff}$

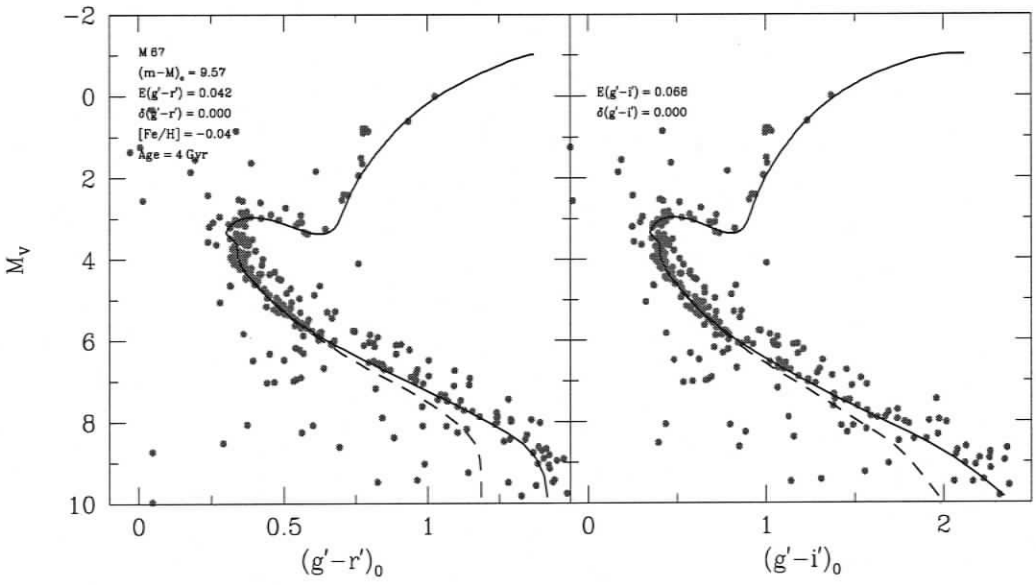

Figure 4.16: $(g' - r')$ and $(g' - i')$ versus M_V for the open cluster M 67 overplotted with the same 4 Gyr, [Fe/H] $= -0.04$ isochrone used above but this time the colors for cooler dwarf stars have been corrected to match the lower main sequence of the cluster (solid lines). Note the fits obtained using purely synthetic colors are provided as dashed lines.

relations, particularly at the metal-rich end. With the wealth of photometry resulting from the SDSS and the proliferation of the $u'g'r'i'z'$ bandpasses among different telescopes and observing projects, this database will undoubtedly begin to grow quite rapidly in the near future as investigators focus on calibrating the $u'g'r'i'z'$ system against fundamental stellar properties (see, for example, Allende Prieto et al. 2005).

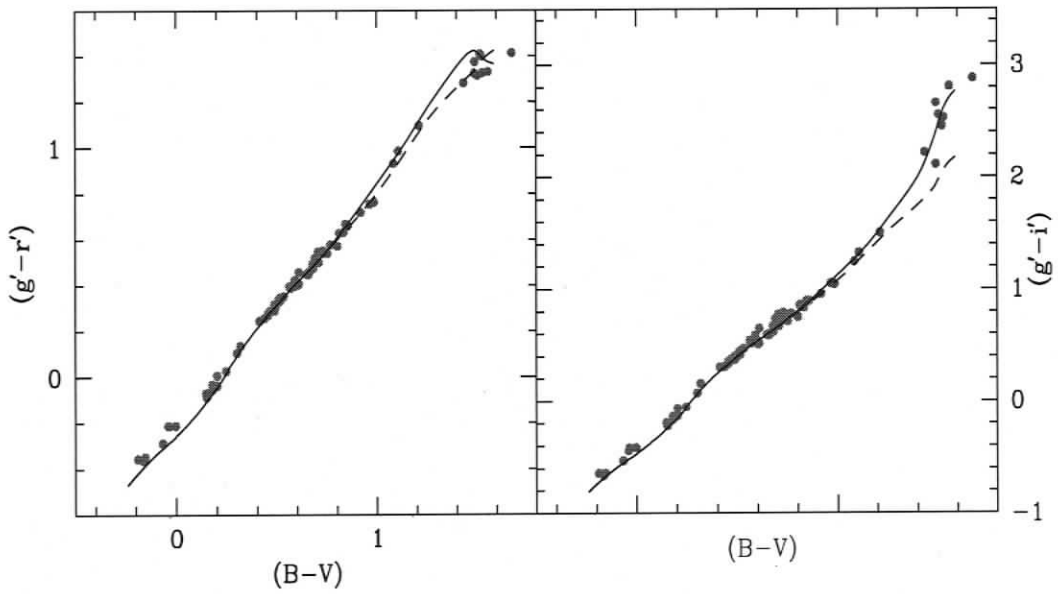

Figure 4.17: The revised fits of a solar-metallicity ZAMS model to the $u'g'r'i'z'$ standard stars from S02 using the colors that have been empirically corrected to the lower main sequence of M 67. Note the improved agreement for the reddest dwarf star, most notably on the $[B-V,\, g'-i']$ plane.

Chapter 5

Conclusions

5.1 Summary

The goal of this study has been to provide the empirical and theoretical tools that are vital to the analysis of stellar populations data resulting from observational efforts that may employ the $u'g'r'i'z'$ or other related filter sets, most notably the SDSS. In this respect, fiducial stellar population samples that extend over a broad range in magnitude and metallicity have been derived along with a set of theoretical color–$T_{\rm eff}$ relations and bolometric corrections for the $u'g'r'i'z'$ system computed from synthetic stellar spectra that span a wide range of stellar parameter space. Moreover, an extensive collection of secondary standard stars has been established in a number of different star clusters that are accessible to observatories in the northern hemisphere. While these sequences have been employed here to ensure that the fiducials are well-calibrated to the standard system, it is anticipated they can serve as useful calibrators for other observations obtained on large, high-demand telescopes by virtue of the fact they are concentrated in smaller regions of sky, and they extend to much fainter magnitudes than the primary standard star network defined by S02.

It has been claimed frequently throughout this study that the cluster fiducial

sequences and color–$T_{\rm eff}$ relations presented here are applicable to the stellar populations data resulting from the SDSS. It is important to emphasize, however, that the results of this investigation are strictly valid for photometric data sets that have been calibrated to the $u'g'r'i'z'$ system as defined by the S02 sample of standard stars and *not* to the photometry obtained by the SDSS itself in the so-called *ugriz* system. Indeed, the small differences between the USNO and SDSS filter sets that were described in Chapter 1 imply that this investigation would have had to derive fiducials from star cluster photometry collected by the 2.5 m survey telescope, and calculate synthetic colors and bolometric corrections using the *ugriz* filter transmission functions in order to claim they are applicable directly to stellar populations data obtained by the SDSS. While accomplishment of the former is relatively straightforward process, provided the *ugriz* transmission functions are accurately known, the latter is a bit more challenging since only a handful of globular cluster observations have been included in the latest SDSS data release, and because the SDSS survey will not extend to low-enough Galactic latitudes to observe some of the more metal-rich open clusters. Fortunately, the transformations between the two systems can be described using relations that involve only small, linear color terms that are valid to the regions of color and magnitude space covered by the cluster fiducial sequences (see Rider et al. 2004). As a result, the fiducials derived here can be readily translated to the SDSS *ugriz* data with a reasonable degree of accuracy.

To demonstrate this, Figure 5.1 provides CMDs for the globular cluster M 13 that are based on observations from the SDSS itself overplotted with the fiducial sequences derived in this investigation, but transformed to the *ugriz* indices using Equations 3.1-3.5). Clearly, the differences between the loci of cluster stars in *ugriz* CMDs are barely discernible when compared to the *transformed* fiducial sequences. This figure also demonstrates yet another reason why the SDSS data are insufficient to derive precise fiducial sequences since the SDSS survey camera saturates at bright magnitudes, and fails to provide high-precision photometry for MS stars lying well

below the cluster turnoffs. As a result, if ridge lines were to be derived from the SDSS cluster data set, they would only be applicable to stars lying on the lower-RGB, SGB, TO, and upper-MS regimes.

As far as the applicability of the color–$T_{\rm eff}$ relations to *ugriz* data is concerned, a parallel grid of theoretical indices has been produced from Kurucz synthetic spectra using the *ugriz* transmission functions, and, as shown in Figure 5.2, the transformation equations between the USNO and SDSS systems do a reasonable job of translating a solar metallicity ZAMS model to the *ugriz* color planes. Given the discrepancies between the synthetic and observed colors for low-temperature dwarf stars present in the CMDs comparisons for M 67 and NGC 6791 (see Chapter 4), any empirical corrections that are deemed necessary to the $u'g'r'i'z'$ colors to match observations should likewise be applicable to the *ugriz* colors.

5.2 Future Work

Although the goals of providing stellar fiducial sequences and color–$T_{\rm eff}$ relations for the $u'g'r'i'z'$ system have been accomplished in this study, the very fact that a large amount of high-quality cluster photometry has been obtained using CFHT's wide-field MegaCam imager implies that these data can serve as an excellent resource for a host of other cluster studies. In addition, a supplementary set of very-deep observations for some of the globular clusters discussed here have been obtained using the 8 m Gemini telescopes (with its analogous set of $u'g'r'i'z'$ filters). Preliminary results reveal that these data extend the cluster photometry approximately 2 mags fainter down the MS (the Gemini data are currently being processed, and, therefore, the results are not described in this study). The combination of these two very unique and highly homogeneous data sets, one covering a very large region of sky surrounding each cluster, and another probing some of the faintest cluster members, offers a terrific opportunity to gain new insight into the dynamical and evolutionary properties of

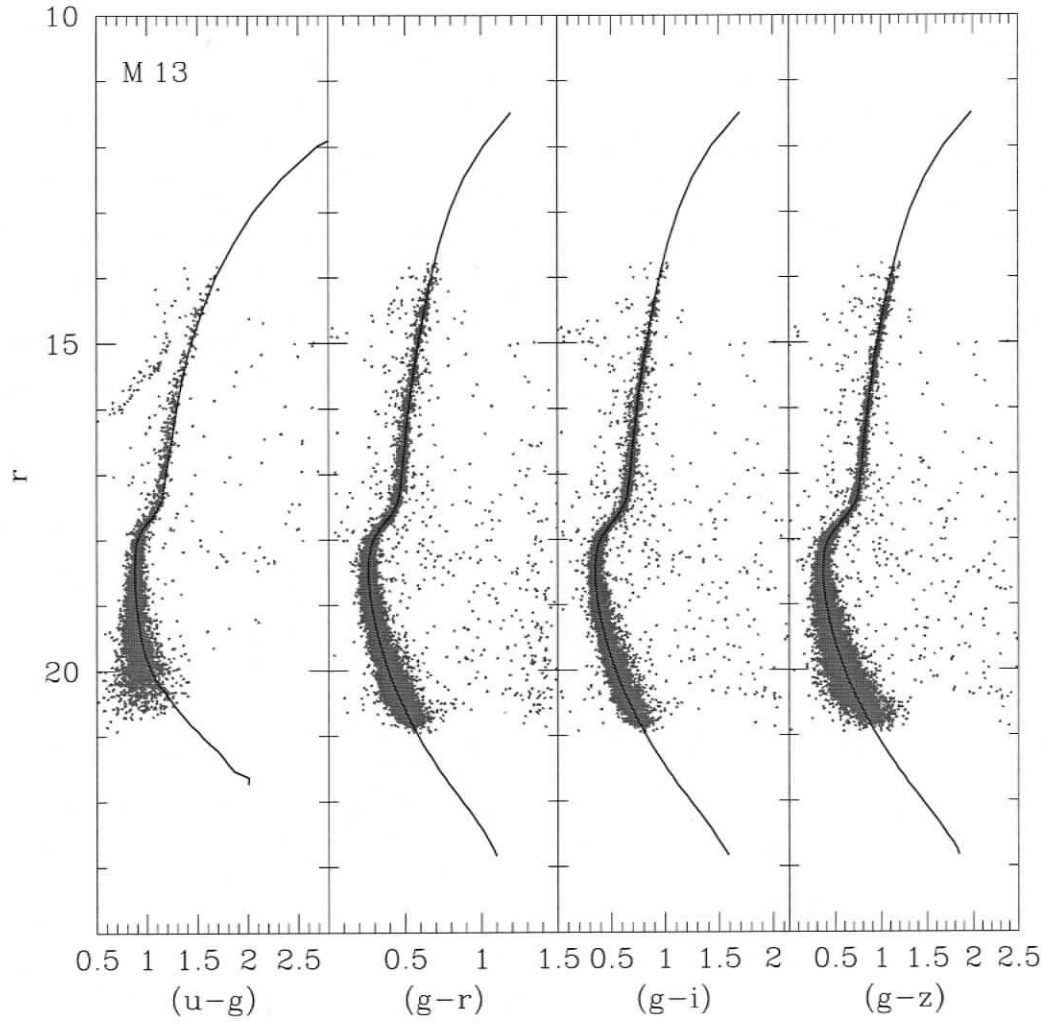

Figure 5.1: Multiple CMDs for the globular cluster M 13 derived from SDSS photometry overplotted with the fiducial sequences that have been transformed to *ugriz* indices using the relations of Rider et al. The correspondence between the two data sets provides a good indication that the fiducials derived in this study for the $u'g'r'i'z'$ system are applicable to the stellar populations data resulting from the SDSS.

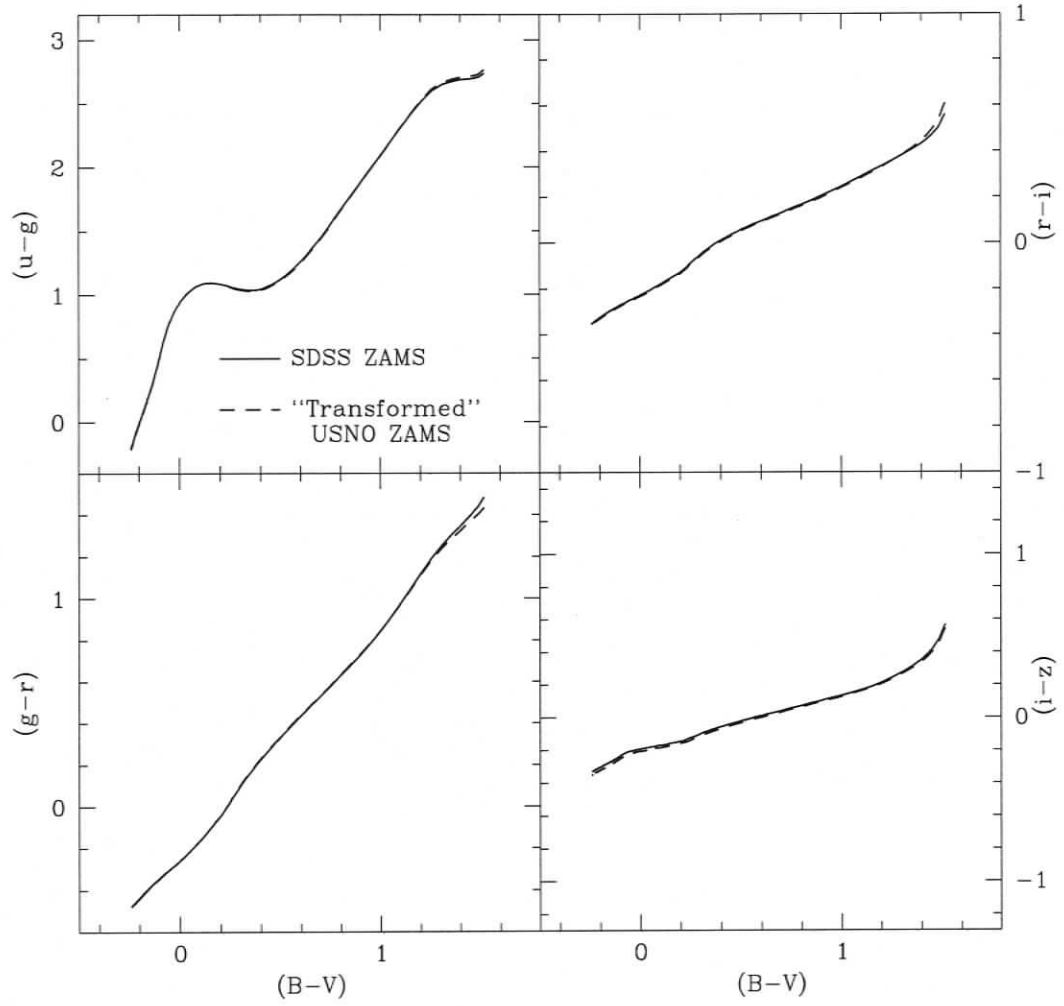

Figure 5.2: Various color-color plots employing $B - V$ as the abscissa comparing two solar-metallicity ZAMS models – one employing computed color–$T_{\rm eff}$ relations for the *ugriz* bandpasses, and another relying on the relations predicted for the $u'g'r'i'z'$ bandpasses but transformed to *ugriz* indices using the relations of Rider et al. (2004). Note the good agreement between the two over almost the entire range in *ugriz* colors

these clusters. In fact, efforts are already underway to exploit these opportunities by completing the reduction of the remaining CCD chips in the MegaCam images along with the extraction of photometry for faint main sequence stars from the deep GMOS images. A short description of the potential these two unique data sets have for redefining our understanding of globular cluster systems is provided in the remainder of this discussion.

5.2.1 Testing Stellar Models for Low-Mass Stars

The faint globular cluster fiducial sequences resulting from the combination of the CFHT and Gemini observations offers a chance to test the reliability of current stellar evolutionary and atmospheric models in describing the observed properties of low-mass, metal-poor stars. Theoretical modelling of very-low-mass stars has long been a difficult task, owing to the high densities and the low temperatures that characterize the structure of these stars (Cassisi et al. 2000; Baraffe et al. 2002). While comparisons between theory and observation in the past have largely relied upon data collected by the Hubble Space Telescope for only the nearest globular clusters (e.g., M 4; Richer et al. 2004, NGC 6752; Ferraro et al. 1997, and NGC 6397; Cool et al. 1996), the availability of deep, ground-based data for a larger sample of clusters spanning a wide range in metallicity ($-2.5 \lesssim$ [Fe/H] $\lesssim -0.5$) can provide additional tests of the validity of current stellar models down to $\lesssim 0.2\,M_{\odot}$. In this respect, numerous comparisons between theory and observed HST data in the past have shown that the evolutionary models and/or the derived color-$T_{\rm eff}$ relations for low-mass, metal-poor stars fail to match the observed lower-MS locus in some globular clusters, particularly those having [Fe/H] $\gtrsim -1.5$. Since reliable evolutionary models are a necessary ingredient in the determinations of accurate cluster mass functions, as well as providing constraints on stellar formation processes, the availability of a larger database of deep globular cluster photometry can only help to provide additional

observational constraints on current and future stellar models for very-low-mass stars.

5.2.2 Cluster Tidal Tails

Observational studies of tidal tails from globular clusters have only recently been carried out because of difficulties in obtaining high-quality wide-field photometry. The advent of large-format mosaic imagers on current large-aperture telescopes is beginning to revolutionize the search for tidal structures by providing an opportunity to search for tidal extensions and derive cluster shape parameters via direct star counts, rather than relying on surface photometry extracted from older photographic surveys. This area of research has the potential to be quite fruitful given the recent findings of Odenkirchen et al. (2003) who report the discovery of faint tidal tails extending over an arc of 10 degrees on the sky from the globular cluster Palomar 5 using SDSS photometric data. In addition, stellar density profiles and two-dimensional density maps derived from recent deep, wide-field CCD observations (see, for example, the works of Sohn et al. 2003 and Lee et al. 2003, 2004) suggest that many globular clusters have weak halos or tails of unbound stars that might result from tidal stripping. The CFHT database presented here is likely to contribute to the study of tidal extensions by greatly expanding the sample of globular clusters having deep, wide-field CCD observations.

5.2.3 Mass Segregation

The effects of mass segregation within star clusters is evident by the concentration of higher mass stars closer to the cluster core with low-mass members largely distributed in the outer cluster environments. It is well known that the radial variations in the stellar mass and luminosity functions offer the best insight into the degree of this mass segregation effect within a particular cluster (Pryor et al. 1986). Moreover, by employing mass functions to compare the stellar content of different clusters,

insight into their formation and dynamical evolution can be gained. The wide-field data obtained on CFHT has been shown to extend faint enough to allow a precise determination of a cluster's mass function down to $M_{r'} \sim 9$ over large angular radii, thereby providing a detailed probe into the variation of mass distribution between the innermost and outermost cluster environments. In addition, the resulting mass functions for these clusters can be combined with results of other investigations to test the hypotheses that the mass function of a cluster depends on its position in the Galaxy, its metallicity, and/or its dynamical history (see, for example, McClure et al. 1986; Aguilar et al. 1989; Djorgovski et al. 1993).

Bibliography

Abazajian, K. et al.: 2003, *Astron. Journal,* **126**, 2081

Abazajian, K. et al.: 2004, *Astron. Journal,* **128**, 502

Adelman-McCarthy, J. K. et al.: 2005, *astro-ph/0507711*

Allende Prieto, C. et al.: 2005, *astro-ph/0509812*

Alonso, A., Arribas, S., and Martinez-Roger, C.: 1996, *Astron. & Astrophys.,* **313**, 873

Alonso, A., Arribas, S., and Martínez-Roger, C.: 1999, *Astron. & Astrophys. Supp.,* **140**, 261

Anders, E. and Grevesse, N.: 1989, *Geochim. Cosmochim. Acta,* **53**, 197

Baraffe, I., Chabrier, G., Allard, F., and Hauschildt, P. H.: 2002, *Astron. & Astrophys.,* **382**, 563

Bergbusch, P. A. and VandenBerg, D. A.: 2001, *Astrophys. Journal,* **556**, 322

Bessell, M. S., Castelli, F., and Plez, B.: 1998, *Astron. & Astrophys.,* **333**, 231

Brown, T. M., Ferguson, H. C., Smith, E., Guhathakurta, P., Kimble, R. A., Sweigart, A. V., Renzini, A., Rich, R. M., and VandenBerg, D. A.: 2005, *Astron. Journal,* **130**, 1693

Cacciari, C., Corwin, T. M., and Carney, B. W.: 2005, *Astron. Journal,* **129**, 267

Carretta, E. and Gratton, R. G.: 1997, *Astron. & Astrophys. Supp.,* **121**, 95

Cassisi, S., Castellani, V., Ciarcelluti, P., Piotto, G., and Zoccali, M.: 2000, *Mon. Not. Royal Astron. Soc.,* **315**, 679

Castelli, F., Gratton, R. G., and Kurucz, R. L.: 1997, *Astron. & Astrophys.*, **318**, 841

Clem, J. L., VandenBerg, D. A., Grundahl, F., and Bell, R. A.: 2004, *Astron. Journal,* **127**, 1227 (Paper II)

Cool, A. M., Piotto, G., and King, I. R.: 1996, *Astrophys. Journal,* **468**, 655

de Santis, R. and Cassisi, S.: 1999, *Mon. Not. Royal Astron. Soc.,* **308**, 97

Djorgovski, S., Piotto, G., and Capaccioli, M.: 1993, *Astron. Journal,* **105**, 2148

Ferraro, F. R., Carretta, E., Bragaglia, A., Renzini, A., and Ortolani, S.: 1997, *Mon. Not. Royal Astron. Soc.,* **286**, 1012

Friel, E. D. et al.: 2002, *Astron. Journal,* **124**, 2693

Frogel, J. A., Persson, S. E., and Cohen, J. G.: 1981, *Astrophys. Journal,* **246**, 842

Fukugita, M., Ichikawa, T., Gunn, J. E., Doi, M., and Shimasaku, K. & Schneider, D. P.: 1996, *Astron. Journal,* **111**, 1748 (GS83)

Girardi, L., Bertelli, G., Bressan, A., Chiosi, C., Groenewegen, M. A. T., Marigo, P., Salasnich, B., and Weiss, A.: 2002, *Astron. & Astrophys.,* **391**, 195

Girardi, L., Grebel, E. K., Odenkirchen, M., and Chiosi, C.: 2004, *Astron. & Astrophys.,* **422**, 205

Grundahl, F., Stetson, P. B., and Andersen, M. I.: 2002, *Astron. & Astrophys.,* **395**, 481

Grundahl, F., Vandenberg, D. A., and Andersen, M. I.: 1998, *Astrophy. Journal Letters,* **500**, L179+

Grundahl, F., VandenBerg, D. A., Bell, R. A., Andersen, M. I., and Stetson, P. B.: 2000, *Astron. Journal,* **120**, 1884

Gunn, J. E. and Stryker, L. L.: 1983, *Astrophys. J. Supp.,* **52**, 121

Kraft, R. P. and Ivans, I. I.: 2003, *Pub. Astron. Soc. Pacific,* **115**, 143

Landolt, A. U.: 1973, *Astron. Journal,* **78**, 959

Landolt, A. U.: 1983, *Astron. Journal,* **88**, 439

Landolt, A. U.: 1992, *Astron. Journal,* **104**, 340

Lee, K. H., Lee, H. M., Fahlman, G. G., and Lee, M. G.: 2003, *Astron. Journal,* **126**, 815

Lee, K. H., Lee, H. M., Fahlman, G. G., and Sung, H.: 2004, *Astron. Journal,* **128**, 2838

Magnier, E. A. and Cuillandre, J.-C.: 2004, *Pub. Astron. Soc. Pacific,* **116**, 449

McClure, R. D., Vandenberg, D. A., Smith, G. H., Fahlman, G. G., Richer, H. B., Hesser, J. E., Harris, W. E., Stetson, P. B., and Bell, R. A.: 1986, *Astrophy. Journal Letters,* **307**, L49

Moffat, A. F. J.: 1969, *Astron. & Astrophys.,* **3**, 455

Monet, D. G. et al.: 2003, *Astron. Journal,* **125**, 984

Montgomery, K. A., Marschall, L. A., and Janes, K. A.: 1993, *Astron. Journal,* **106**, 181

Odenkirchen, M., Grebel, E. K., Dehnen, W., Rix, H.-W., Yanny, B., Newberg, H. J., Rockosi, C. M., Martínez-Delgado, D., Brinkmann, J., and Pier, J. R.: 2003, *Astron. Journal,* **126**, 2385

Oke, J. B. & Gunn, J. E.: 1983, *Astrophys. Journal,* **266**, 713

Pryor, C., Smith, G. H., and McClure, R. D.: 1986, *Astron. Journal,* **92**, 1358

Ramírez, I. and Meléndez, J.: 2005, *Astrophys. Journal,* **626**, 465

Richer, H. B. et al.: 2004, *Astron. Journal,* **127**, 2771

Rider, C. J., Tucker, D. L., Smith, J. A., Stoughton, C., Allam, S. S., and Neilsen, E. H.: 2004, *Astron. Journal,* **127**, 2210

Schlegel, D. J., Finkbeiner, D. P., and Davis, M.: 1998, *Astrophys. Journal,* **500**, 525

Sekiguchi, M. and Fukugita, M.: 2000, *Astron. Journal,* **120**, 1072

Smith, J. A. et al.: 2002, *Astron. Journal,* **123**, 2121 (S02)

Sohn, Y.-J., Park, J.-H., Rey, S.-C., Lee, Y.-W., Kim, H.-I., Oh, S. J., Lee, S.-G., Lee, M. G., and Han, W.: 2003, *Astron. Journal,* **126**, 803

Stetson, P. B.: 1987, *Pub. Astron. Soc. Pacific,* **99**, 191

Stetson, P. B.: 1990, *Pub. Astron. Soc. Pacific,* **102**, 932

Stetson, P. B.: 2000, *Pub. Astron. Soc. Pacific,* **112**, 925

Stetson, P. B., Bruntt, H., and Grundahl, F.: 2003, *Pub. Astron. Soc. Pacific,* **115**, 413

Stetson, P. B. and Harris, W. E.: 1988, *Astron. Journal,* **96**, 909

VandenBerg, D. A.: 2005, *astro-ph/0510789*

VandenBerg, D. A., Bergbusch, P. A., and Dowler, P. D.: 2005, *astro-ph/0510784*

VandenBerg, D. A. and Clem, J. L.: 2003, *Astron. Journal,* **126**, 778 (Paper I)

VandenBerg, D. A., Richard, O., Michaud, G., and Richer, J.: 2002, *Astrophys. Journal,* **571**, 487

VandenBerg, D. A., Swenson, F. J., Rogers, F. J., Iglesias, C. A., and Alexander, D. R.: 2000, *Astrophys. Journal,* **532**, 430

York, D. G. et al.: 2000, *Astron. Journal,* **120**, 1579

Zinn, R. and West, M. J.: 1984, *Astrophys. J. Supp.,* **55**, 45 (ZW84)